EFFECT OF LOADING RATE AND THERMOMECHANICAL COUPLING ON FRACTURE OF SHAPE MEMORY ALLOYS

by

İsmail Yiğit Özbaş

B.S., Mechanical Engineering, Boğaziçi University, 2016

Submitted to the Institute for Graduate Studies in
Science and Engineering in partial fulfillment of
the requirements for the degree of
Master of Science

Graduate Program in Mechanical Engineering
Boğaziçi University
2019

EFFECT OF LOADING RATE AND THERMOMECHANICAL COUPLING ON FRACTURE OF SHAPE MEMORY ALLOYS

APPROVED BY:

Prof. Günay Anlaş .....
(Thesis Supervisor)

Assist. Prof. Alpay Oral .....

Assist. Prof. Sertan Alkan .....

DATE OF APPROVAL: 30.05.2019

ACKNOWLEDGEMENTS

I would like to express my sincere gratitude to my thesis supervisor Prof. Günay Anlaş for his guidance, support, leadership and motivation. Thanks to him, I feel much more confident in technical subjects and I was able to develop valuable personal skills.

I acknowledge Assist. Prof. Alpay Oral and Assist. Prof. Sertan Alkan for their precious time and constructive feedbacks.

I would like to thank my colleagues Fatma Mutlu and Gülcan Özerim for their friendship, motivation and support.

I would like to thank my family for their financial support and encouragement.

I would like to thank Sıla Türkü Aşkın for her support and advises.

This work was supported by Bogazici University Scientific Research Project fund with grant number 12784P.

ABSTRACT

EFFECT OF LOADING RATE AND THERMOMECHANICAL COUPLING ON FRACTURE OF SHAPE MEMORY ALLOYS

This work is on the investigation of the effect of loading rate and thermomechanical coupling on mechanical behavior and fracture of shape memory alloys (SMA). The constitutive model of Zaki and Moumni (ZM) is studied in detail and re-derived. With the changing loading rates, the ZM model does not capture correctly the martensite start stress. Based on experimental works of Tobushi *et al.*, Mutlu and Shaw, a relation is proposed for the martensite start stress, σ_{ms} to account for a change in loading rate. Some model parameters contain σ_{ms} as variable, so, they are also proposed to be function of local strain rate. For numerical calculations ABAQUS is used and therefore the user subroutine UMAT is rewritten accordingly. Finite element simulations are conducted with modified model parameters using the specimen of Shaw. The stress-strain behavior and hysteresis area are compared to the results obtained by using the unchanged ZM model. The fracture specimen, used in Mutlu's experiments is modeled using original and modified model. Transformation regions, crack mouth opening displacements (CMOD), temperature fields and stress intensity factors are obtained using original coupled/uncoupled and modified models to investigate effect of loading rate and thermomechanical coupling; the results are compared to experimental ones.

ÖZET

TERMOMEKANİK ETKİLEŞİMİN VE YÜKLEME HIZININ, ŞEKİL HAFIZALI ALAŞIMLARDAKİ KIRILMA MEKANİĞİNE OLAN ETKİSİ

Bu çalışma, şekil hafızalı alaşımlardaki (ŞHA) termomekanik etkileşimin, mekanik davranış ve kırılma davranışları üzerine etkisinin incelenmesi hakkındadır. Zaki ve Moumni'nin geliştirdiği model (ZM) ayrıntılı bir şekilde çalışılmış ve yeniden türetilmiştir. Yüksek yükleme hızlarında, ZM modelinin, martensit başlangıç gerilmesini σ_{ms} doğru yakalayamadığı anlaşılmıştır. Tobushi *et al.*, Mutlu ve Shaw'un deneysel çalışmalarına dayanarak, ZM modelinde bir malzeme parametresi olan martensit başlangıç gerilmesinin, σ_{ms} şekil değiştirme hızının bir fonksiyonu olduğu ileri sürülmüştür. Bazı model parametreleri, değişken olarak σ_{ms} içerdiğinden, onların da yerel şekil değiştirme hızının bir fonksiyonu olması önerilmiştir. Nümerik hesaplamalar için ABAQUS kullanılmıştır ve bunun için, kullanıcı alt yordamı UMAT, tekrardan yazılmıştır. Sonlu elemanlar simülasyonu, Shaw'un deneysel çalışması temel alınarak, modifiye edilmiş model parametreleri ile yapılmıştır. Gerilme-şekil değiştirme davranışı ve histerez alanı sonuçları, orijinal ZM model ile karşılaştırılmıştır. Mutlu'nun deneylerinde kullandığı kırılma numunesi, orijinal ve modifiye edilmiş model kullanılarak modellenmiştir. Dönüşüm bölgeleri, çatlak ağzı açıklığı yer değiştirmeleri (CMOD), sıcaklık alanları ve gerilme şiddeti faktörleri, orijinal ve modifiye edilmiş model kullanılarak elde edilmiştir; termomekanik etkileşimin ve yükleme hızının etkisini araştırmak için deneysel sonuçlarla karşılaştırılmıştır.

TABLE OF CONTENTS

ACKNOWLEDGEMENTS iii
ABSTRACT iv
ÖZET v
LIST OF FIGURES ix
LIST OF TABLES xiv
LIST OF SYMBOLS xv
LIST OF ACRONYMS/ABBREVIATIONS xviii
1. INTRODUCTION 1
1.1. Shape Memory Alloys 1
1.2. Phase Transformation 1
1.2.1. Shape Memory Effect (SME) 4
1.2.2. Superelasticity 6
1.3. Application Areas 7
1.4. Constitutive Modelling of SMAs 9
1.4.1. Microscopic Models 9
1.4.2. Micro-Macro Models 10
1.4.3. Macroscopic Models 10
1.4.4. Thermomechanical Coupling of Shape Memory Alloys 11
2. GOVERNING EQUATIONS 12
2.1. The ZM Constitutive Model 12
2.2. Helmholtz Free Energy 13
2.2.1. Internal Energy, u 13
2.2.2. Helmholtz Free Energy 15
2.3. The Inelastic Case - State Variables and Internal Variables 16
2.4. Internal Constraints 19
2.5. The Lagrangian and State Equations 21
2.6. Pseudo-potential of Dissipation 23
2.6.1. Derivation of Dissipation 23
2.7. Determination and Identification of Parameters in the Constitutive Model 29

2.7.1. Orientation of Twinned Martensite and Determination of Y, α and β . . . 29
2.7.2. Pseudoelastic Experiment and the Determination of a, b, G, κ, ζ 31
2.8. Addition of Thermomechanical Coupling . . . 35
2.8.1. Heat Equation . . . 37
2.9. Effect of Thermal Strain . . . 38
2.10. Boundaries of the Thermomechanically Coupled Problem . . . 41
2.11. Plastic Strain as Dissipative Variable . . . 42
2.12. Summary . . . 45
3. MODIFICATION OF THE ZM MODEL . . . 46
3.1. Effect of Model Parameters on Mechanical Behavior . . . 46
3.1.1. Effect of Phase Change Heat Density, $C(T)$ . . . 46
3.1.2. Effect of Interaction Energy W_{it} . . . 47
3.2. On Pseudopotential of Dissipation Coefficients a, b and G . . . 48
3.3. Modification of Material Parameters a and G Based on Strain Rate . . 51
3.3.1. Determination of Parameters m and n . . . 57
3.4. Algorithmic Setup and Implementation of m and n to UMAT . . . 63
3.4.1. Boundary Value Problem . . . 63
3.4.2. Time Discretization . . . 65
3.4.3. Algorithmic Setup . . . 68
4. RESULTS . . . 69
4.1. Effect of Phase Change Heat Density, $C(T)$, on Mechanical Behavior . 69
4.2. On the Forward Transformation Function $\mathcal{F}_z^1$, Using Strain Rate Dependence . . . 71
4.3. FE Analysis Using Modified Parameters a, b and G, and Their Effect on Mechanical Behavior . . . 76
4.4. FE Analysis Using Modified Material Parameters a and G, and Their Effect on Mechanical Behavior . . . 80
5. EDGE CRACKED NITINOL . . . 85
5.1. Introduction . . . 85
5.2. Fracture Mechanics of Shape Memory Alloys . . . 85

5.3. Problem Statement 89
5.4. Evaluation of Stress Intensity Factor 89
5.4.1. Strain Energy Release Rate and J Integral 91
5.5. Computational Evaluation of Fracture Parameters 91
5.6. Results 94
5.6.1. Transformation Region 94
5.6.2. Fracture Parameters 95
5.6.3. Temperature and Transformation Around the Crack Tip 101
5.6.4. Discussion 104
6. CONCLUSION 106
REFERENCES 109
APPENDIX A: EQUIVALENT STRESS AND STRAIN 119
APPENDIX B: DERIVATION OF THE TANGENT OPERATORS 124

LIST OF FIGURES

Figure 1.1. Microstructure and Thermodynamic State of Different Phases and the Arrow Indicates the Loading Path [1]. 2

Figure 1.2. Thermally Induced Phase Transformation [2]. 3

Figure 1.3. Temperature Induced Phase-Transformation at Constant non-zero Stress [2]. 4

Figure 1.4. Twinning and Detwinning of Martensite Variants Under Applied Stress [2]. 5

Figure 1.5. Stress-Strain-Temperature Graph of NiTi SMA Exhibiting Shape Memory Effect [2]. 5

Figure 1.6. Pseudoelastic Loading Path and Stress-Temperature Relation [2]. . 6

Figure 1.7. Stress-Strain Diagram of Pseudoelastic SMA [2]. 6

Figure 1.8. SMA Coupling Used in Aerospace Tubing for Metal to Metal Sealing [3]. 7

Figure 1.9. SMA Wires Used in Orthodontic Applications [4]. 8

Figure 1.10. Self Expandable SMA Stent for Cardiovascular Applications [4]. . 8

Figure 1.11. SMA Wire Used in Automotive Industry [5]. 9

Figure 2.1. $C(T)$ vs Material Temperature (κ = 8.2138 MPa, ζ = 0.2586 MPa/K). 18

Figure 2.2. Detwinned Martensite and ϵ_0 [2]. 20

Figure 2.3. Reuss Model with Austenite and Martensite Phases. 22

Figure 2.4. Measurement of Orientation Stresses σ_{rs}, σ_{rf}, Elastic Modulus of Martensite E_M and Maximum Orientation Strain ϵ_0 from Orientation Experiment [6]. 30

Figure 2.5. Detwinning of Martensite Variants Under Applied Stress, T is Below M_f^0 [2]. 30

Figure 2.6. Stress-Strain Response of an SMA Under Pseudoelastic Uniaxial Loading. 32

Figure 2.7. Stress-Temperature State at the End of Reverse Transformation . 34

Figure 3.1. W_{it}/A vs Martensite Volume Fraction, z. 48

Figure 3.2. Experimental vs Numerical Stress-Strain Curves for Various Strain Rates [7]. 52

Figure 3.3. Evolution of the Mechanical Response to a Pseudoelastic Loading at Different Strain Rates [7]. 53

Figure 3.4. Experimental Data of Tobushi *et al.* [8] with Various Strain Rates. 54

Figure 3.5. Experimental Data of Mutlu with Various Strain Rates [9]. 54

Figure 3.6. σ_{ms} vs Strain Rate (Log Scale) [8]. 55

Figure 3.7. σ_{ms} vs Strain Rate (Log Scale). 56

Figure 3.8. Martensite Start Stress vs Logarithm of Strain Rate. 59

Figure 3.9. σ_{af} vs Strain Rate (Log Scale) [8]. 60

Figure 3.10. Austenite Finish Stress vs Logarithm of Strain Rate. 63

Figure 3.11. Algorithm for Coupled Model. 68

Figure 4.1. Stress-Strain Curves. 71

Figure 4.2. Yield Surface of $\mathcal{F}_z^1 = 0$ at $z = 0$ and $z = 1$. 72

Figure 4.3. Yield Surface of $\mathcal{F}_z^1 = 0$ at $z = 0$ and $z = 1$ From Different Angles and Orientations. 73

Figure 4.4. von Mises Yield Surface in Principal Coordinates [10]. 74

Figure 4.5. σ_{eq} vs σ_h for $z = 0$ and $z = 1$. 75

Figure 4.6. Yield Surface of $\mathcal{F}_z^1 = 0$ with Different Temperature at $z = 0$. . . . 75

Figure 4.7. Yield surface of $\mathcal{F}_z^1 = 0$ at $z = 0$ with several strain rates using modified model. 76

Figure 4.8. Dogbone Specimen Dimensions in mm. 77

Figure 4.9. Stress(MPa) - Strain(mm/mm) Diagram. 78

Figure 4.10. Temperature (K) - Strain(mm/mm) Diagram. 78

Figure 4.11. Stress- (MPa) - Strain(mm/mm) Diagram with Modified Parameters. 79

Figure 4.12. Temperature (K)-Strain(mm/mm) Diagram with Modified Parameters(Yellow) and Initial Parameters (Red). 79

Figure 4.13. Stress (MPa)-Strain(mm/mm) Enlarged Beginning of Transformation. 80

Figure 4.14. Stress (MPa)-Strain(mm/mm) Enlarged End of Transformation. . 80

Figure 4.15. Boundary Conditions and Geometry of the NiTi Specimen. 81

Figure 4.16. Comparison of Simulations and Experimental Data. 82

Figure 5.1. Dimensions of the NiTiNOL Plate. 89

Figure 5.2. FE Geometry of CT Specimen, Loading and Boundary Conditions. 92

Figure 5.3. Mesh of the CT Specimen. 93

Figure 5.4. Contour Numbers 10 and 65 and Their Corresponding Effective Regions. 96

Figure 5.5. Energy Release Rate J ($\frac{kJ}{m^2}$) vs Time for the Simulations. 97

Figure 5.6. J vs Contour #. 98

Figure 5.7. Displacement Contour Plots Obtained from FE and Eq. 5.3 Original Model. 99

Figure 5.8. Displacement Contour Plots Obtained from FE and Eq. 5.3 Modified Model. 99

Figure 5.9. Temperature (K) vs Time (s) at the Crack Tip and at the Boundary of Transformation Region. 102

Figure 5.10. Martensite Volume Ratio (z) Contours. 103

Figure 5.11. Temperature (K) Contours. 103

Figure 5.12. Martensitic Volume Fraction Contours. 104

Figure 5.13. Temperature Contours. 104

LIST OF TABLES

Table 4.1. Material Properties 69

Table 4.2. $C(T')$ and Temperature Values. 70

Table 4.3. Material Properties 77

Table 4.4. Modified Material Properties 79

Table 4.5. Material Properties 81

Table 4.6. Hysteresis Area 83

Table 5.1. Material Properties of Pseudoelastic NiTi 93

Table 5.2. Material Properties of Austenite Simulation 94

Table 5.3. Material Properties of Martensite Simulation 94

Table 5.4. r_M and r_T Values for $\dot{\epsilon} = 2$mm/min. 95

Table 5.5. Stress Intensity Factor K_I. 100

Table 5.6. Crack Mouth Opening Displacement, CMOD. 101

LIST OF SYMBOLS

a, b, G, Y, m, n, c, d	Material parameters of ZM model
A_s	Austenite start stress at zero stress
A_f	Austenite finish stress at zero stress
A_f^0	Austenite finish temperature at zero stress
$\mathcal{A}_\alpha$	Thermodynamic force associated with α
C_v	Specific heat at constant strain
C_p	Specific heat capacity at constant pressure
D_h	Heat dissipation
D_i	Intrinsic dissipation
D_t	Total dissipation
$\mathcal{D}$	Pseudopotential of dissipation
E_A	Elastic modulus of Austenite
E_M	Elastic modulus of Martensite
El_{MA}	$(1+v)/(1/E_M - 1/E_A)$
$\boldsymbol{f}$	Body forces
$\mathcal{F}_z^1$	Forward transformation yield function
$\mathcal{F}_z^2$	Reverse transformation yield function
$\mathcal{F}_{ori}^1$	Orientation yield function
h	Heat transfer coefficient
$\boldsymbol{I}$	Identity matrix
J	J integral
$\mathcal{J}$	Material Jacobian
k	Thermal conductivity
$\boldsymbol{K}$	Equivalent elastic moduli tensor
$\boldsymbol{K}_A$	Elastic moduli tensor of Austenite
$\boldsymbol{K}_M$	Elastic moduli tensor of Martensite
K_I	Mode I stress intensity factor
$\mathcal{L}$	Lagrangian

M_f	Martensite finish stress at zero stress
M_s	Martensite start stress at zero stress
$\boldsymbol{n}$	Outward unit vector normal to the boundary
P_{MA}	$v/E_A - v/E_M$
$\boldsymbol{q}$	Heat flux vector
Q	Inner heat generation
r	External heat source
s	Entropy
$\boldsymbol{s}$	Stress deviator
$\boldsymbol{S}$	Macroscopic stress deviatoric tensor
t, T	Time
T_0	Reference temperature
$\boldsymbol{T}^d$	Contact forces
u	Internal energy
$\boldsymbol{u}$	Displacement vector
$\boldsymbol{u}^d$	Displacement on volume Ω
W	Helmholtz free energy
W_A	Free energy density of Austenite
W_M	Free energy density of Martensite
W_{it}	Interaction energy density
W_1	Constraint potential
z	Martensite volume fraction
$\alpha, \beta, \kappa, \zeta$	Material parameters of ZM model
$\boldsymbol{\alpha}$	Equivalent thermal expansion coefficient tensor
$\boldsymbol{\alpha}_A$	Thermal expansion coefficient tensor of Austenite
$\boldsymbol{\alpha}_M$	Thermal expansion coefficient tensor of Martensite
$\boldsymbol{\epsilon}$	Total strain tensor
$\boldsymbol{\epsilon}_A$	Austenite strain tensor
ϵ_{eq}^{ori}	Equivalent orientation strain
$\boldsymbol{\epsilon}_M$	Martensite strain tensor

$\boldsymbol{\epsilon}_{ori}$	Orientation strain tensor
ϵ_0	Maximum orientation strain
η	Inelastic multiplier for martensite reorientation
θ	Temperature
λ, μ	Lamé constants
μ_1, μ_2	Lagrange multipliers
ν	Poisson's ratio
ρ	Density
$\boldsymbol{\sigma}$	Stress tensor
σ_{af}	Austenite finish stress
σ_{as}	Austenite start stress
σ_{eq}	Equivalent stress
σ_h	Hydrostatic stress
σ_{mf}	Martensite finish stress
σ_{ms}	Martensite start stress
σ_{rf}	Reorientation finish stress
σ_{rs}	Reorientation start stress
Ω	3D volume in Euclidian space
Ω_d	Design space

LIST OF ACRONYMS/ABBREVIATIONS

3D	Three Dimensional
ASTM	American Society for Testing and Material
CMOD	Crack Mouth Opening Displacement
CT	Compact Tension
DIC	Digital Image Corelation
FE	Finite Elements
FEA	Finite Elements Analysis
FEM	Finite Elements Method
LEFM	Linear Elastic Fracture Mechanics
SIF	Stress Intensity Factor
SMA	Shape Memory Alloy
SME	Shape Memory Effect
PE	Pseudo-Elasticity
NiTi	Nickel-Titanium
UMAT	User Defined Material Subroutine
ZM	Zaki-Moumni

1. INTRODUCTION

1.1. Shape Memory Alloys

Shape Memory Alloys (SMAs) are metallic alloys with interesting mechanical characteristics, attracting researchers over past decades. SMAs are referred to as smart materials that are capable of recovering from large amount of strains without permanent deformation upon removal of loading. This distinctive recovery behavior is a result of martensitic phase transformation. This, together with high tensile strength and high corrosion resistance, increased the popularity and usage of SMAs in a wide range of applications from biomedical industry to aerospace engineering. The unique behavior of SMAs lies in its crystal structure. Solid to solid diffusionless phase transformation takes place between two phases: parent phase austenite, stable at higher temperatures and lower stresses, and martensite, stable at lower temperatures and higher stresses. Depending on the thermomechanical state of the material, initial phase might be austenite or a martensite variant. Two different mechanisms cause phase transformation: shape memory effect (SME-by change in temperature) and pseudoelasticity (PE-by loading). The pseudo-elastic behavior Shape Memory Effect (SME) has been discovered by Arne Ölander in 1932 who observed an Au-Cd alloy [11]. The most commercial and used SMA is called NiTiNOL and its discovery dates back to 1963. It is a Nickel-Titanium alloy found by W.J. Dueler in US Naval Ordinance Laboratory hence the alloy is called NiTiNOL [12]. From that time on Nickel-Titanium based alloys (NiTi) became popular and used in wide range of industries [13].

1.2. Phase Transformation

Generally, phase transformation is used to describe transitions between solid, liquid and gas phases. However in the case of SMAs, a solid to solid diffusionless phase transformation occurs between austenite and martensite phases. A change in loading, temperature, magnetic field etc. might change the crystal structure of the SMA. Austenite is the stable phase at higher temperature and lower stresses (atoms

are packed loosely), while martensite phase is stable at lower temperature and higher stress having lower crystallographic symmetry which can be seen schematically in Fig. 1.1.

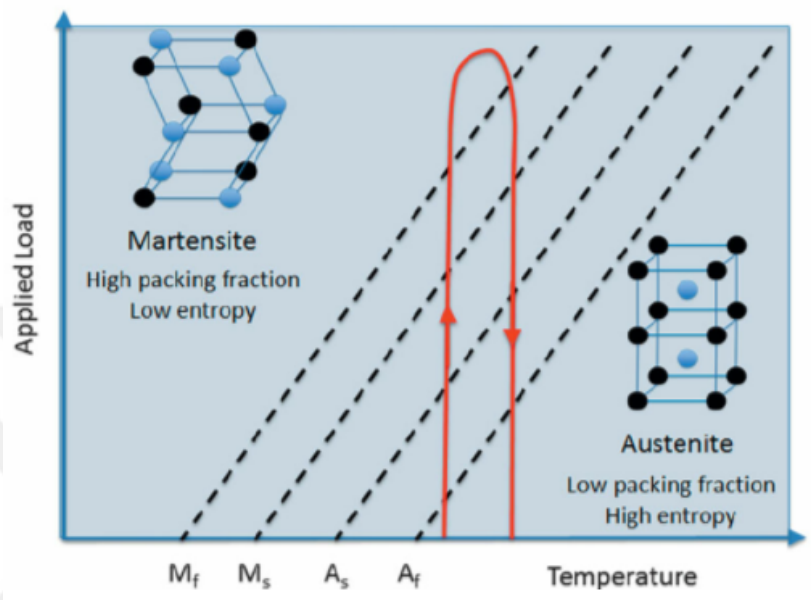

Figure 1.1. Microstructure and Thermodynamic State of Different Phases and the Arrow Indicates the Loading Path [1].

Phase transformation between austenite and martensite may be induced by changing material temperature at constant stress. Depending on material entropy and transformation temperatures, a solid to solid phase change occurs as shown in Fig. 1.2.

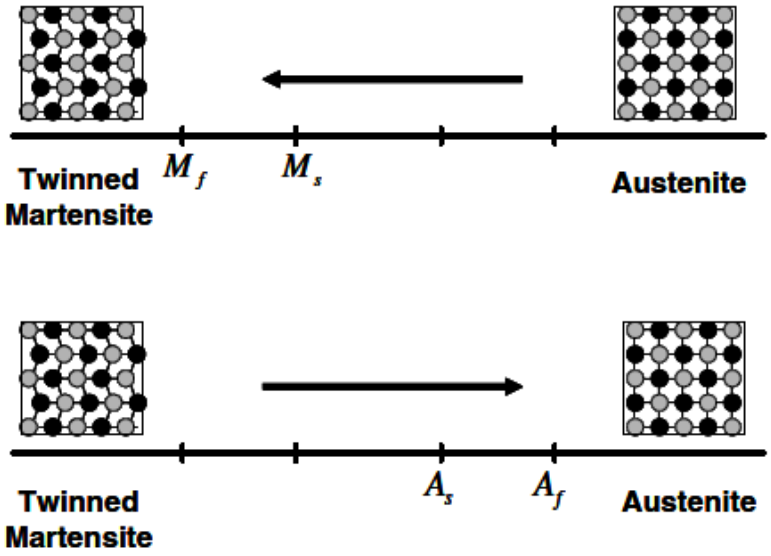

Figure 1.2. Thermally Induced Phase Transformation [2].

Here M_f, M_s, A_s, A_f are the martensite finish, martensite start, austenite start, and austenite finish temperatures, twinned martensite is the variant of the martensite at zero stress. When stress is applied to the twinned martensite it is detwinned and microstructure of the material changes (see Fig. 1.3). Transformation from austenite to martensite by cooling starts at M_s. When material is cooled down below M_f material becomes fully martensite. Reversely, transformation from martensite to austenite by heating starts at A_s and finishes when A_f is reached. Martensite is the stable phase temperatures below M_f, and austenite is stable temperatures above A_f. Note that these are the transformation start and finish temperatures at zero stress. An increase in stress changes these transformation temperatures since, phase transformation is function of both temperature and stress. In Fig. 1.3 change of transformation temperatures with respect to stress can be seen.

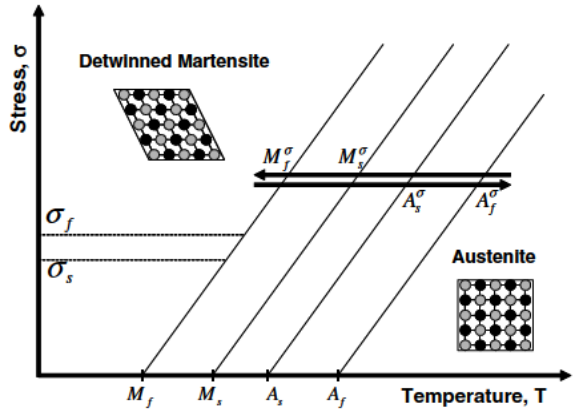

Figure 1.3. Temperature Induced Phase-Transformation at Constant non-zero Stress [2].

1.2.1. Shape Memory Effect (SME)

Shape Memory Effect (SME) feature is the ability of an SMA to recover from deformation and to regain its original shape upon heating. When austenite SMA is cooled, it turns into martensite phase. Lower symmetry of martensite phase allows existence several martensite variants [14]. The type of martensite variant is related to its thermomechanical state. Two main types of martensite variants may exist within an SMA:

- Twinned (self-accommodating) martensite, comes into existence in the absence of applied stress through twinning and no macroscopic strain is observed. It is the stable phase of SMA at temperatures lower than martensite finish temperature in the absence of stress. ($T \leq M_f$)
- Detwinned martensite, forms when stress is applied on material, forcing variants to reorient into a single variant.

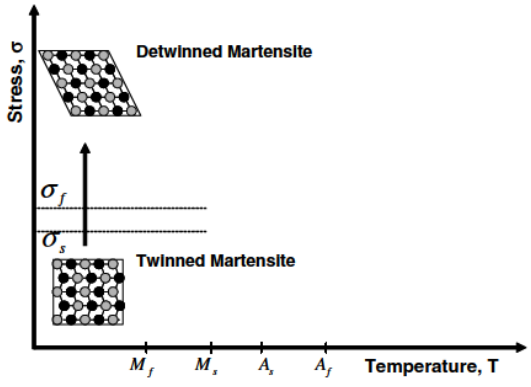

Figure 1.4. Twinning and Detwinning of Martensite Variants Under Applied Stress [2].

Deformation of twinned martensite by applying load may change the martensite variant to detwinned martensite. When detwinned variant is unloaded deformation remains. At this state if the detwinned martensite is heated above austenite finish temperature it transforms into austenite and recovers its initial shape. When material is cooled below martensite finish temperature, twinned martensite variant at the initial state with original shape is obtained. Shape memory effect can be seen in Fig. 1.5.

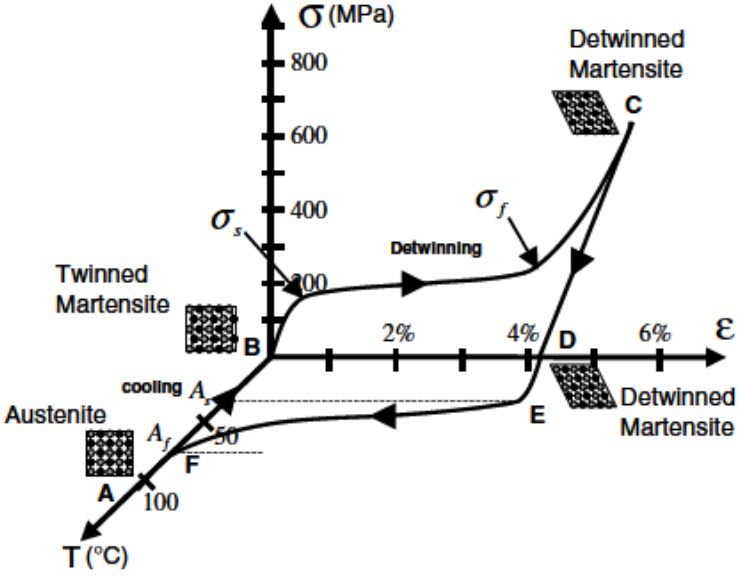

Figure 1.5. Stress-Strain-Temperature Graph of NiTi SMA Exhibiting Shape Memory Effect [2].

1.2.2. Superelasticity

Superelasticity, also known as pseudoelasticity (PE) is stress induced martensitic transformation. Above austenite finish temperature A_f, material is fully austenite. If a load, high enough to induce transformation is applied, fully detwinned (oriented) martensite forms. Upon the removal of the loading or with increase in temperature above A_f, the material recovers its original shape. Stress-strain and stress-temperature relations are represented in Figures 1.6 and 1.7. σ_{af}, σ_{as}, are the austenite finish and austenite start stresses at reverse transformation, σ_{ms}, σ_{mf} are the martensite start and martensite finish stresses at forward transformation.

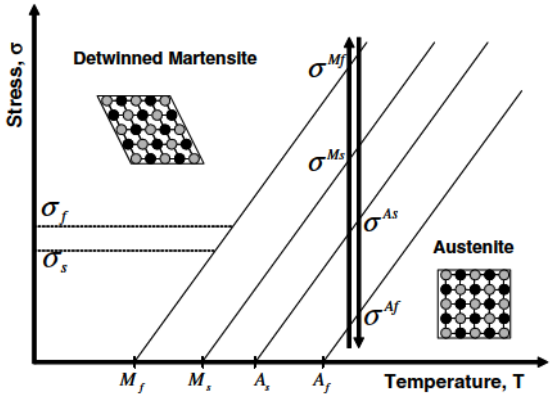

Figure 1.6. Pseudoelastic Loading Path and Stress-Temperature Relation [2].

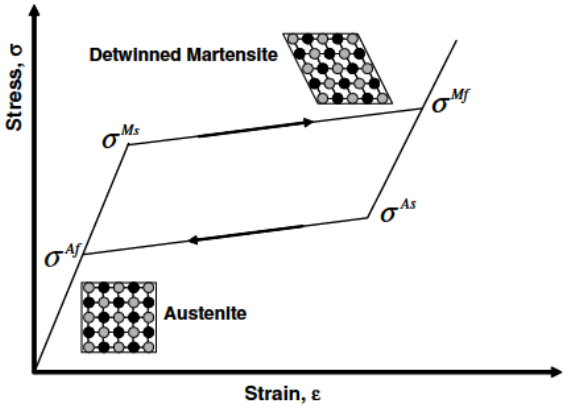

Figure 1.7. Stress-Strain Diagram of Pseudoelastic SMA [2].

1.3. Application Areas

SMAs have superior mechanical properties thanks to their pseudoelastic and shape memory effect behaviors. Distinguished mechanical properties together with their ease of adaptability and bio-compatibility widening the usage. First industrial applications of SMAs were in the military sector in 1971, connecting hydraulic tubing in F-14 aircraft [15]. By changing the temperature of the SMA, tight sealing in the tubing was achieved.

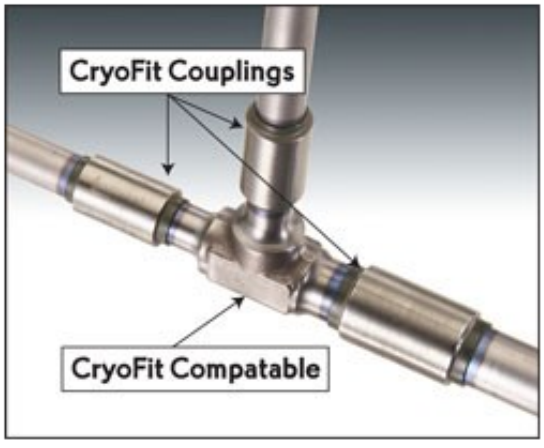

Figure 1.8. SMA Coupling Used in Aerospace Tubing for Metal to Metal Sealing [3].

Medical, military, transportation and aerospace applications were the first of SMAs. Lately, thanks to its high corrosion resistance and reliability, NiTi is mainly used in cardiovascular and orthodontic medical applications (see Figs. 1.9 - 1.10).

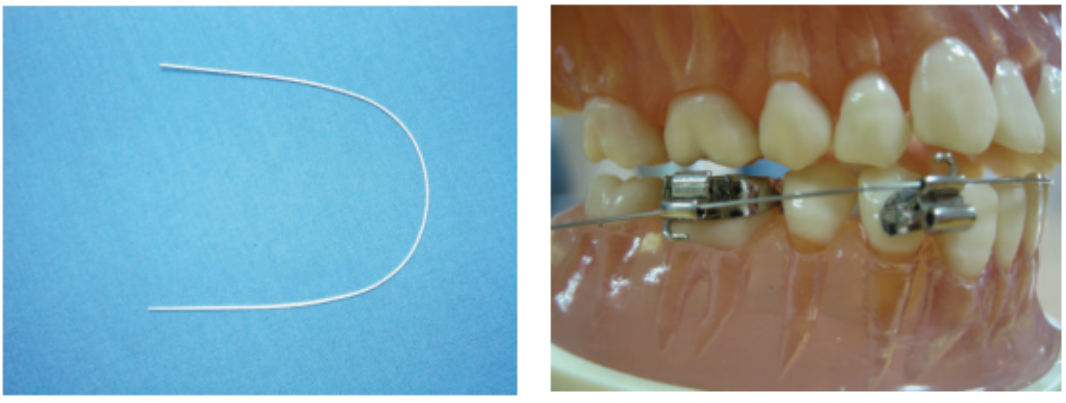

Figure 1.9. SMA Wires Used in Orthodontic Applications [4].

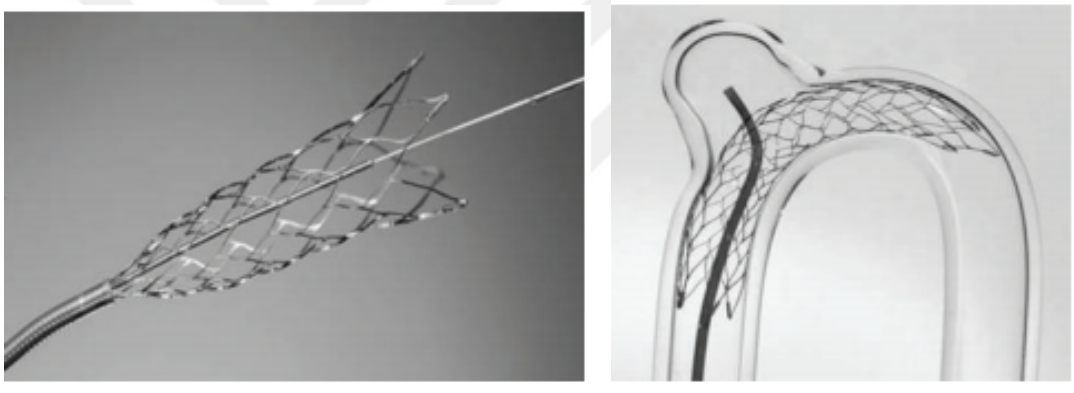

Figure 1.10. Self Expandable SMA Stent for Cardiovascular Applications [4].

NiTi is also used in temperature controls and actuators. Wire actuators used in automotive sector, use the contraction of the SMA under temperature instead of electrical components. SMA actuators both offer more economic, lighter and simpler solutions. In Fig. 1.11, fuel door cover can be seen. A SMA-wire actuator and a spring is used to open the fuel door.

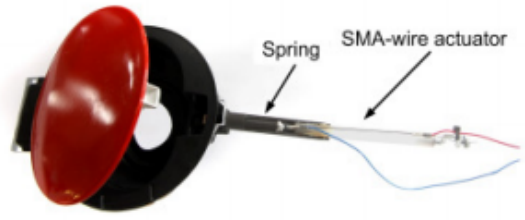

Figure 1.11. SMA Wire Used in Automotive Industry [5].

Researchers are working to understand and estimate mechanical behavior of SMAs to use them at their fully extend.

1.4. Constitutive Modelling of SMAs

To understand mechanical behavior of SMA realistically, proper constitutive models are needed. There are several different models which use different approaches. This section is dedicated to brief explanation of various constitutive models based on their scale of application.

1.4.1. Microscopic Models

Microscopic models describe phase nucleation, interface motion, martensite twin growth at the grain level [16]. These models are mainly derived from polynomial energy expression, which are written in terms of observable variables like strain and temperature. Falk [17, 18], used Ginsburg-Landrau (GL) theory within the framework of continuum thermodynamics to build up a model for martensitic transformation. Later GL theory was used to investigate fine phase mixtures by Ball and James [19]. FEM is used to model multivariant martensitic phase transformation based on strain softening model by Idesman *et al.* [20], and using phase field model by Zhong and Zhu [21]. Microscopic models are utile tools for understanding SMA behavior at microscopic level. However, since binding continuum is very small, these models have large computational

time and lack the adaptability for the usage of commercial engineering applications.

1.4.2. Micro-Macro Models

The micro-macro models are based on micromechanics to characterize material behavior at microscopic or mesoscopic level. To derive macroscopic constitutive equations, scale transition is applied [22–26]. Development of these models requires observable variables (such as temperature T, strain $\boldsymbol{\epsilon}$ and stress $\boldsymbol{\sigma}$) and internal variables (such as volume fraction of martensite z and inelastic orientation strain $\boldsymbol{\epsilon}_{ori}$). One of the first models which uses internal variables as a model parameter was developed by Frémond [27]. Despite their accuracy in physical simulations, the main restriction of micro-macro models are that, they require high number of degrees of freedom which increases the computational time. Another drawback of these models are the large number of state variables and internal variables which is not appreciated in engineering applications.

1.4.3. Macroscopic Models

Macroscopic models are based on simplified micro-macro thermodynamics or experimental data. Main objective of these models are capturing the macroscopic SMA behavior such as pseudoelasticty and shape memory effect. Tanaka in 1986 [28], established a phenomenological macroscopic model by using temperature, macroscopic strain and martensitic volume fraction as variables to explain phase transformation in SMAs. An exponential transformation hardening function is suggested. Liang and Rogers [29], used a cosine function for the evolution of the volume fraction of martensite. Detwinning of martensite is also considered in their work. Brinson [30], proposed separation of the volume fraction of martensite into the purely temperature induced martensite with multiple variants and stress induced single martensite variant. Boyd and Lagoudas [31], introduced a model that accounts for martensite reorientation by defining an inelastic strain tensor and using Gibbs free energy and dissipation potential. A polynomial transformation function is proposed. This model was validated experimentally by [32]. Raniecki *et al.* [33, 34] built RL model which predicts the formation

of hysteresis loop by using Clasius-Duhem inequality. An interaction energy between phase variants are included on the model. Lubliner and Auricchio [35] and Auricchio *et al.* [36], used general plasticity approach based on internal variable formalism. Their constitutive model accounts for superelasticity and single variant martensite orientation. Zaki-Moumni (ZM) model [6], is developed on the basis of generalized standard materials with internal constraints [37], in order to ensure thermodynamical consistency.

1.4.4. Thermomechanical Coupling of Shape Memory Alloys

Experimental works have revealed that there is strong thermomechanical coupling due to heat generation [38, 39]. The heat generation results in temperature change which then affects the mechanical behavior. Shaw and Kyrikakides [38], conducted several experiments at different strain rates, temperatures and media(water and air). The results revealed that strain rate dependence is higher in air than water since heat transfer to water is higher, temperature variation lower. Peyroux *et al.* [40], investigated temperature variations of SMAs using infrared cameras and calorimetry. Their experiments show that temperature variations are mainly caused by latent heat of phase change and deformation of work rather than intrinsic dissipated energy. Nemat-Nasser and Guo examined superelastic and cyclic response of SMAs over the range of $10^{-3}/s$ to $4200/s$ strain rates and at initial temperatures between $77 - 400K$ [41]. They concluded that SMAs have stronger sensitivity to temperature than to strain rate. Grabe and Bruhns [42], conducted several experiments at different strain rates under isothermal conditions. They found that at isothermal conditions, stress-strain behavior is the same regardless of the strain rate; so the dominant factor effecting the mechanical behavior is temperature variation that is a result of strain rate if there is not sufficient cooling. Several thermomechanically coupled models are developed based on the experimental observations. Morin *et al.* [7], improved the Zaki-Moumni model by adding heat equation. Their model suggested that, intrinsic dissipation governs the mechanical hysteresis and latent heat governs the thermal behavior.

2. GOVERNING EQUATIONS

In this chapter the constitutive model that is used in this work is derived in detail and discussed. Additions of thermomechanical coupling [7], thermal strain [43], and plastic strain [44], are also elaborated.

2.1. The ZM Constitutive Model

To study SMAs, together with equilibrium and strain displacement equations a valid constitutive model that will represent the mechanical behavior is needed. In this chapter, first, a general thermodynamic formulation with Helmholtz free energy will be given, and following, the formulation given by Zaki and Moumni [6], a constitutive model that can be used to describe mechanical behavior of NiTiNOL will be rederived. The effects of various parameters will be discussed, and to better account for the effect of temperature change, some modifications will be proposed.

Zaki-Moumni (ZM) model was developed following the thermomechanical model proposed by Halphen and Nguyen for generalized standard materials with internal constraints [37]. The dissipative phase transformation process is assumed to be governed by two internal variables: martensitic volume fraction z, and local martensite orientation strain tensor $\boldsymbol{\epsilon}_{ori}$. Because orientation of martensite causes a reversible inelastic deformation, $\boldsymbol{\epsilon}_{ori}$ is also chosen as an internal variable. Martensitic phase transformation is an exothermic process so martensite volume fraction z, is also taken as a dissipative variable.

To derive evolution of the dissipative variables, state variables and internal variables are defined and a free energy density is formed. Then the Lagrangian is established using internal constraints. Using the Lagrangian, state equations and thermodynamic forces associated with dissipative variables are obtained. Using a pseudopotential of dissipation and thermodynamic forces, transformation functions that give the evolution of the dissipative variables are derived.

2.2. Helmholtz Free Energy

In this section thermodynamic potentials, internal energy u and Helmholtz free energy W are written in terms of their state variables. Then from those potentials constitutive equation is obtained. Linear dependence of the specific heat on temperature is assumed [45].

2.2.1. Internal Energy, u

Incremental internal energy in terms of incremental strain and entropy is given as follows:

$$du = \sigma_{ij} d\epsilon_{ij} + T ds. \tag{2.1}$$

Internal energy u is a state function and du is therefore a perfect differential:

$$\left(\frac{\partial \sigma_{ij}}{\partial s}\right)_{\epsilon} = \left(\frac{\partial T}{\partial \epsilon_{ij}}\right)_{s} \tag{2.2}$$

For an isotropic material stress-strain relation can be written as follows [46]:

$$\sigma_{ij} = \lambda_T \epsilon_{KK} \delta_{ij} + 2\mu \epsilon_{ij} - \kappa_T \alpha_0 (T - T_0) \delta_{ij} \tag{2.3}$$

where λ_T and μ are the isothermal Lamé elastic constants $\kappa_T = \lambda_T + 2\mu/3$ is the isothermal bulk modulus and α_0, c_v^0 and s_0 are the coefficient of volumetric thermal expansion, the specific heat at constant strain, and the specific entropy, all in the reference state with temperature T_0 respectively. Assuming linear dependence of specific heat on temperature:

$$c_V = c_v^0 \frac{T}{T_0} \tag{2.4}$$

Partial differentiation of Eq. 2.3 gives the following:

$$\left(\frac{\partial \sigma_{ij}}{\partial s}\right)_{\epsilon} = \left(\frac{\partial \sigma_{ij}}{\partial T}\right)_{\epsilon} \left(\frac{\partial T}{\partial s}\right)_{\epsilon} = -\kappa_T \boldsymbol{\alpha}_0 \left(\frac{\partial T}{\partial s}\right)_{\epsilon} \delta_{ij} \tag{2.5}$$

Maxwell relation in Eq. 2.2 gives:

$$\left(\frac{\partial T}{\partial \epsilon_{ij}}\right)_{s} = -\kappa_T \alpha_0 \left(\frac{\partial T}{\partial s}\right)_{\epsilon} \delta_{ij} \tag{2.6}$$

Specific heat at constant strain is:

$$c_v = T \left(\frac{\partial s}{\partial T}\right)_{\epsilon} \tag{2.7}$$

using Eq. 2.4 expression above becomes:

$$\left(\frac{\partial T}{\partial s}\right)_{\epsilon} = \frac{T_0}{c_v^0} \tag{2.8}$$

substitution into Eq. 2.6 gives:

$$\left(\frac{\partial T}{\partial \epsilon_{ij}}\right)_{s} = -\frac{\kappa_T \alpha_0 T_0}{c_v^0} \delta_{ij} \tag{2.9}$$

Integration of Eqs. 2.8 and 2.9 yields:

$$T = -\frac{\kappa_T \alpha_0 T_0}{c_v^0} \epsilon_{kk} + \frac{T_0}{c_v^0}(s - s_0) + T_0 \tag{2.10}$$

Inserting this into Eq. 2.3, stress in terms of strain and entropy is obtained.

$$\sigma_{ij} = \lambda_S \epsilon_{kk} \delta_{ij} + 2\mu \epsilon_{ij} - \frac{\kappa_T \alpha_0 T_0}{c_v^0}(s - s_0)\delta_{ij} \tag{2.11}$$

where λ_s is the adiabatic Lamé constant. The joint integration of Eqs. 2.10 and 2.11 gives:

$$\sigma_{ij} = \left(\frac{\partial u}{\partial \epsilon_{ij}}\right)_s, \qquad T = \left(\frac{\partial u}{\partial s}\right)_\epsilon, \tag{2.12}$$

This yields the expression for internal energy u, in terms of the independent variables ϵ_{ij} and s:

$$u(\epsilon_{ij}, s) = \frac{1}{2}\lambda_s \epsilon_{kk}^2 + \mu \epsilon_{ij}\epsilon_{ij} - \frac{\kappa_T \alpha_0 T_0}{c_v^0}(s - s_0)\epsilon_{kk} + \frac{T_0}{2c_v^0}(s - s_0)^2 + T_0(s - s_0). \tag{2.13}$$

2.2.2. Helmholtz Free Energy

Helmholtz free energy is a function of strain and temperature and it can be written in incremental form as follows:

$$dW = \sigma_{ij} d\epsilon_{ij} - s dT \tag{2.14}$$

with Maxwell relation:

$$\left(\frac{\partial \sigma_{ij}}{\partial T}\right)_\epsilon = -\left(\frac{\partial s}{\partial \epsilon_{ij}}\right)_T \tag{2.15}$$

Calculating the temperature gradient of stress from Eq. 2.3, and using Maxwell relation in Eq. 2.15 following relation is found:

$$\left(\frac{\partial s}{\partial \epsilon_{ij}}\right)_T = \kappa_T \alpha_0 \delta_{ij} \tag{2.16}$$

Integrating the expression above, in conjunction with:

$$\left(\frac{\partial s}{\partial T}\right)_\epsilon = \frac{c_v^0}{T_0} \tag{2.17}$$

gives the following entropy:

$$s = \kappa_T \alpha_0 \epsilon_{kk} + \frac{c_v^0}{T_0}(T - T_0) + s_0 \tag{2.18}$$

Using Eqs. 2.3 and 2.18, the integration of,

$$\sigma_{ij} = \left(\frac{\partial W}{\partial \epsilon_{ij}}\right)_T, \qquad s = -\left(\frac{\partial W}{\partial T}\right)_\epsilon, \tag{2.19}$$

gives the Helmholtz free energy W, in terms of its independent variables ϵ_{ij} and T.

$$W(\epsilon_{ij}, T) = \frac{1}{2}\lambda_T \epsilon_{kk}^2 + \mu \epsilon_{ij}\epsilon_{ij} - \kappa_T \alpha_0 (T - T_0)\epsilon_{kk} - \frac{c_v^0}{2T_0}(T - T_0)^2 - s_0(T - T_0). \tag{2.20}$$

2.3. The Inelastic Case - State Variables and Internal Variables

In a nonelastic case, internal variables that account for dissipation are used together with the state variables [47]. Observable variables such as temperature and deformation are the state variables; internal variables are introduced to describe internal microscopic processes that occur in the material and reveal themselves at the macroscopic scale in the form of dissipation [48]. The dimension of the state space of deformation and temperature (state variables) is expanded by introducing dissipative internal variables [49]. To characterize the local behavior of the SMA the following state and internal variables are used [6]:

- Macroscopic strain tensor $\boldsymbol{\epsilon}$,
- Local strain tensor of austenite and martensite $\boldsymbol{\epsilon}_A$ and $\boldsymbol{\epsilon}_M$ where $\boldsymbol{\epsilon} = (1 - z)\boldsymbol{\epsilon}_A + z\boldsymbol{\epsilon}_M$,
- Volume fraction of martensite z, $0 \leq z \leq 1$
- Temperature T,
- Martensite orientation strain tensor $\boldsymbol{\epsilon}_{ori}$

$A_z \geq 0$ and $A_{ori} \geq 0$ are some thermodynamic forces associated with the dissipative internal variables z and ϵ_{ori} and they describe the evolution of z and ϵ_{ori} in time. The constitutive equations are derived from a Lagrangian with internal constraints. A thermodynamic potential, Helmholtz free energy density W, is used while forming the Lagrangian. W consists of W_A, W_M and W_{it} as follows:

$$W = (1 - z)W_A + zW_M + W_{it} \tag{2.21}$$

W_A and W_M are the free energy densities of austenite and martensite and W_{it} is the free energy stems from interaction of phases. Austenite is assumed to be elastic and its free energy density is as follows:

$$W_A = W_A(\boldsymbol{\epsilon}_A) = \frac{1}{2}\boldsymbol{\epsilon}_A : \boldsymbol{K}_A : \boldsymbol{\epsilon}_A \tag{2.22}$$

where $\boldsymbol{K}_A$ is the austenite elastic moduli tensor. Free energy density of martensite is defined as:

$$W_M = W_M(\boldsymbol{\epsilon}_M, \boldsymbol{\epsilon}_{ori}, T) = \frac{1}{2}(\boldsymbol{\epsilon}_M - \boldsymbol{\epsilon}_{ori}) : \boldsymbol{K}_M : (\boldsymbol{\epsilon}_M - \boldsymbol{\epsilon}_{ori}) + C(T) \tag{2.23}$$

Martensite orientation strain $\boldsymbol{\epsilon}_{ori}$ is assumed to be inelastic and $\boldsymbol{K}_M$ is the martensite elastic moduli tensor. $C(T)$ is heat density associated with the phase change and depends on temperature as follows [50]:

$$C(T) = \zeta(T - A_f^0) + \kappa \tag{2.24}$$

where ζ and κ are material parameters and A_f^0 is the reverse phase transformation finish temperature at zero stress. $C(T)$ is related to existence of the phases and explained in detail in section 3.1.1. Variation of $C(T)$ with respect to temperature is shown in Fig. 2.1:

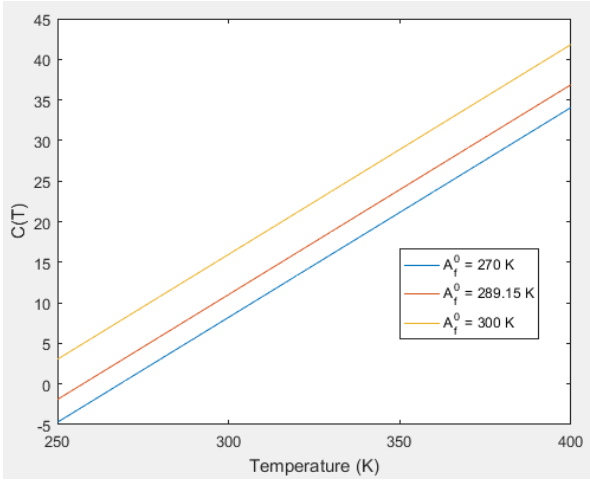

Figure 2.1. $C(T)$ vs Material Temperature ($\kappa = 8.2138$ MPa, $\zeta = 0.2586$ MPa/K).

Interaction energy, W_{it} is due to the interaction between austenite and martensite variants. According to Müller [51], the free energy of the alloy consists of 'the free energy of austenite + the free energy of martensite + interfacial energy'. Here interfacial energy stems from interaction between martensite and austenite layers. Müller proposed an interaction energy that is non-negative and proportional to product of martensitic and austenitic volume ratio ($W_{it} \sim Az(1-z) \geq 0$) where A is a positive coefficient; the phases are expected to be distributed randomly over the domain. In the ZM model, the martensite phase consists of detwinned (oriented) martensite and twinned (self accommodated martensite). Physically twinned martensite is composed of several variants. Interaction of the quantity z on each volume element dz is assumed to be proportional to some material parameter G, therefore the interaction within the twinned martensite is the integral of $Gzdz$ over the volume occupied by martensite, z. The interaction among detwinned martensite variants is proposed to be $\alpha\frac{z^2}{2}\frac{2}{3}(\boldsymbol{\epsilon}_{ori} : \boldsymbol{\epsilon}_{ori})$, inspired from classical elastoplasticity. α determines the slope of the stress-strain curve during martensite orientation. $\beta z(1-z)\frac{1}{3}(\boldsymbol{\epsilon}_{ori} : \boldsymbol{\epsilon}_{ori})$ represents the interaction between austenite with a volume fraction $(1-z)$ and martensite with the volume fraction z. In previous works of Raniecki *et al.* [33] and Müller [51] the interaction between austenite and martensite is proposed to be proportional to product of their volume fractions assuming the phases are distributed randomly over the

material. Zaki [50] proposed this interaction to be proportional to the orientation of martensite. β determines how the loading applied affects martensite orientation during transformation. Combining three interaction energies, W_{it} is written as follows:

$$W_{it} = G\frac{z^2}{2} + \frac{z}{2}[\alpha z + \beta(1-z)](\frac{2}{3}\boldsymbol{\epsilon}_{ori} : \boldsymbol{\epsilon}_{ori}). \tag{2.25}$$

The total free energy density, W, is written as the sum of individual free energy density terms:

$$\begin{aligned} W = W(T, \boldsymbol{\epsilon}_A, \boldsymbol{\epsilon}_M, \boldsymbol{\epsilon}_{ori}, z) = (1-z)[\frac{1}{2}\boldsymbol{\epsilon}_A : \boldsymbol{K}_A : \boldsymbol{\epsilon}_A] \\ + z[\frac{1}{2}(\boldsymbol{\epsilon}_M - \boldsymbol{\epsilon}_{ori}) : \boldsymbol{K}_M : (\boldsymbol{\epsilon}_M - \boldsymbol{\epsilon}_{ori}) + C(T)] \\ + G\frac{z^2}{2} + \frac{z}{2}[\alpha z + \beta(1-z)](\frac{2}{3}\boldsymbol{\epsilon}_{ori} : \boldsymbol{\epsilon}_{ori}). \end{aligned} \tag{2.26}$$

In the equation above, the effects of thermal strain and temperature change are not included. The model could be used for quasistatic loading where temperature change is negligible (isothermal).

2.4. Internal Constraints

- Total strain tensor $\boldsymbol{\epsilon}$ is determined using Reuss model by averaging local austenite and martensite strain tensors with martensite volume fraction:

$$\boldsymbol{\epsilon} = (1-z)\boldsymbol{\epsilon}_A + z\boldsymbol{\epsilon}_M \tag{2.27}$$

- The martensite volume fraction is bounded between 0 and 1:

$$z \geq 0 \quad , \quad (1-z) \geq 0 \tag{2.28}$$

- The level of inelastic deformation due to orientation of martensite may not exceed a certain limit ϵ_0, that is shown in Fig. 2.2. ϵ_0 is the recoverable inelastic strain that forms when twinned martensite is loaded and unloaded. Equivalent inelastic martensitic strain $\epsilon_{ori}^{eq} = \sqrt{\frac{2}{3}\boldsymbol{\epsilon}_{ori} : \boldsymbol{\epsilon}_{ori}}$ can not exceed the maximum orientation strain ϵ_0.

$$\epsilon_0 - \epsilon_{ori}^{eq} \geq 0 \tag{2.29}$$

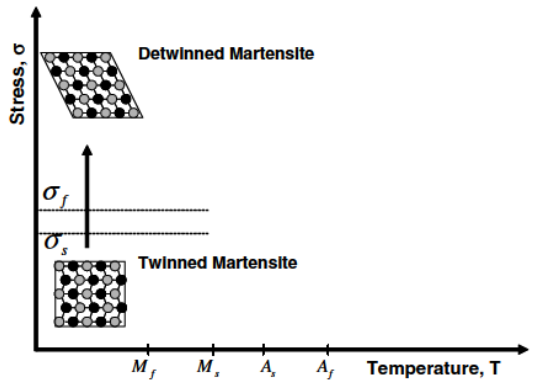

Figure 2.2. Detwinned Martensite and ϵ_0 [2].

A constraint potential W_1 to be used in the Lagrangian is therefore formed as follows:

$$W_1 = -\boldsymbol{\lambda} : [(1-z)\boldsymbol{\epsilon}_A + z\boldsymbol{\epsilon}_M - \boldsymbol{\epsilon}] - \mu(\epsilon_0 - \epsilon_{ori}^{eq}) - v_1 z - v_2(1-z) \tag{2.30}$$

where $\boldsymbol{\lambda}$, μ, v_1, v_2 are Lagrange multipliers, and Eq. 2.30 will be added to account for the constraints:

$$v_1 \geq 0, \quad v_1 z = 0, \tag{2.31}$$

$$v_2 \geq 0 \quad v_2(1-z) = 0, \tag{2.32}$$

$$\mu \geq 0, \quad \mu(\epsilon_0 - \epsilon_{ori}^{eq}) \geq 0. \tag{2.33}$$

2.5. The Lagrangian and State Equations

Summation of free energy density W and constraint potential W_1 in Eqs. 2.26 and 2.30 establish the following Lagrangian:

$$\begin{aligned}\mathcal{L} = W + W_1 =& L(\boldsymbol{\epsilon}, \boldsymbol{\epsilon}_A, \boldsymbol{\epsilon}_M, \boldsymbol{\epsilon}_{ori}, T, z) = (1-z)[\frac{1}{2}\boldsymbol{\epsilon}_A : \boldsymbol{K}_A : \boldsymbol{\epsilon}_A] \\ &+ z[\frac{1}{2}(\boldsymbol{\epsilon}_M - \boldsymbol{\epsilon}_{ori}) : \boldsymbol{K}_M : (\boldsymbol{\epsilon}_M - \boldsymbol{\epsilon}_{ori}) + C(T)] \\ &+ G\frac{z^2}{2} + \frac{z}{2}[\alpha z + \beta(1-z)](\frac{2}{3}\boldsymbol{\epsilon}_{ori} : \boldsymbol{\epsilon}_{ori}) \\ &- \boldsymbol{\lambda} : [(1-z)\boldsymbol{\epsilon}_A + z\boldsymbol{\epsilon}_M - \boldsymbol{\epsilon}] - \mu(\epsilon_0 - \epsilon_{ori}^{eq}) - v_1 z - v_2(1-z) \quad (2.34)\end{aligned}$$

with which conditions in Eqs. 2.31-2.33 are met. The following state equations may be written:

$$\frac{\partial \mathcal{L}}{\partial \boldsymbol{\epsilon}} = \boldsymbol{\sigma} = \boldsymbol{\lambda} \quad \Rightarrow \quad \boldsymbol{\lambda} - \boldsymbol{\sigma} = 0, \quad (2.35)$$

$$\frac{\partial \mathcal{L}}{\partial \boldsymbol{\epsilon}_A} = 0, \quad \Rightarrow \ (1-z)(\boldsymbol{K}_A : \boldsymbol{\epsilon}_A - \boldsymbol{\lambda}) = 0, \quad (2.36)$$

$$\frac{\partial \mathcal{L}}{\partial \boldsymbol{\epsilon}_M} = 0, \quad \Rightarrow \ z[\boldsymbol{K}_M : (\boldsymbol{\epsilon}_M - \boldsymbol{\epsilon}_{ori}) - \boldsymbol{\lambda}] = 0, \quad (2.37)$$

$$-\frac{\partial \mathcal{L}}{\partial z} = \mathcal{A}_z \quad (2.38)$$

$$-\frac{\partial \mathcal{L}}{\partial \boldsymbol{\epsilon}_{ori}} = \mathcal{A}_{ori}, \quad (2.39)$$

$$\frac{\partial \mathcal{L}}{\partial \boldsymbol{\lambda}} = 0 \quad \Rightarrow (1-z)\boldsymbol{\epsilon}_A + z\boldsymbol{\epsilon}_M - \boldsymbol{\epsilon} = 0. \quad (2.40)$$

$\mathcal{A}_z$ and $\mathcal{A}_{ori}$ are the dissipative thermodynamic forces associated with z and ϵ_{ori}:

$$\begin{aligned}\mathcal{A}_z = &\frac{1}{2}[(\boldsymbol{\epsilon}_A : \boldsymbol{K}_A : \boldsymbol{\epsilon}_A) - (\boldsymbol{\epsilon}_M - \boldsymbol{\epsilon}_{ori}) : \boldsymbol{K}_M : (\boldsymbol{\epsilon}_M - \boldsymbol{\epsilon}_{ori})] - C(T) - Gz \\ &- [(\alpha - \beta)z + \frac{\beta}{2}](\frac{2}{3}\boldsymbol{\epsilon}_{ori} : \boldsymbol{\epsilon}_{ori}) - \boldsymbol{\lambda} : (\boldsymbol{\epsilon}_A - \boldsymbol{\epsilon}_M) \quad (2.41)\end{aligned}$$

and

$$\mathcal{A}_{ori} = z[\boldsymbol{K}_M : (\boldsymbol{\epsilon}_M - \boldsymbol{\epsilon}_{ori}) - \frac{2}{3}[\alpha z + \beta(1-z)]\boldsymbol{\epsilon}_{ori}] - \frac{2\mu}{3}\frac{\boldsymbol{\epsilon}_{ori}}{\epsilon_{ori}^{eq}} \quad (2.42)$$

If the austenite and martensite layers are assumed to be in series, using Eqs. 2.35-2.37 stress-strain relations are obtained.

$$\sigma = \boldsymbol{K}_A : \boldsymbol{\epsilon}_A = \boldsymbol{K}_M : (\boldsymbol{\epsilon}_M - \boldsymbol{\epsilon}_{ori}) \tag{2.43}$$

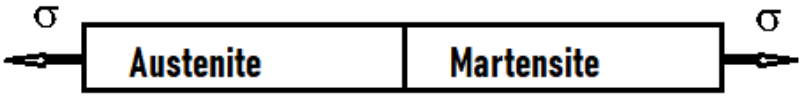

Figure 2.3. Reuss Model with Austenite and Martensite Phases.

Elastic strain ϵ_{el} can be written as:

$$\boldsymbol{\epsilon}_{el} = \boldsymbol{\epsilon} - \boldsymbol{\epsilon}_{inel} \tag{2.44}$$

$$\boldsymbol{\epsilon}_{el} = (1 - z)\boldsymbol{\epsilon}_A + z\boldsymbol{\epsilon}_M - z\boldsymbol{\epsilon}_{ori} \tag{2.45}$$

$$= \boldsymbol{\epsilon} - z\boldsymbol{\epsilon}_{ori} \tag{2.46}$$

In the case here, $\boldsymbol{\epsilon}_{inel} = z\boldsymbol{\epsilon}_{ori}$ because during martensite orientation material deforms inelastically and $\boldsymbol{\epsilon}_{el}$ is the elastic strain. Equivalent elastic moduli tensor is given as follows:

$$\boldsymbol{K}_{eq} = \boldsymbol{K} = [(1 - z)\boldsymbol{K}_A^{-1} + z\boldsymbol{K}_M^{-1}]^{-1} \tag{2.47}$$

therefore the constitutive stress-strain relation given in 2.43 takes the following form:

$$\sigma = \boldsymbol{K} : \boldsymbol{\epsilon}_{el} \tag{2.48}$$

$$= \boldsymbol{K} : (\boldsymbol{\epsilon} - z\boldsymbol{\epsilon}_{ori}) \tag{2.49}$$

2.6. Pseudo-potential of Dissipation

Phase transformation is a dissipative process and thermodynamic forces $\mathcal{A}_z$ and $\mathcal{A}_{ori}$ associated with the dissipative variables z and $\boldsymbol{\epsilon}_{ori}$, are non-zero during phase transformation. To determine the unknown thermodynamic forces $\mathcal{A}_z$ and $\mathcal{A}_{ori}$, in addition to the Lagrangian, complementary laws are needed. In the following, complementary laws will be derived.

2.6.1. Derivation of Dissipation

The Helmholtz free energy is given as:

$$W = u - Ts \tag{2.50}$$

Since in Eq. 2.30 $W_1 = 0$ and $W + W_1 = \mathcal{L}$, Lagrangian can be used instead of W :

$$\mathcal{L} = u - Ts, \tag{2.51}$$

$$\dot{\mathcal{L}} = \dot{u} - \dot{T}s - \dot{s}T \tag{2.52}$$

where u is the internal energy. First law of thermodynamics can be written as:

$$\dot{u} = \boldsymbol{\sigma} : \dot{\boldsymbol{\epsilon}} - div\mathbf{q} + r \tag{2.53}$$

using 2.52,

$$\dot{\mathcal{L}} = \boldsymbol{\sigma} : \dot{\boldsymbol{\epsilon}} - \dot{T}s - T\dot{s} - div\mathbf{q} + r \tag{2.54}$$

where q is the heat influx vector and r is external heat source density. According to second law of thermodynamics:

$$T\dot{s} + div\mathbf{q} - \frac{\mathbf{q}\nabla T}{T} - r \geq 0 \tag{2.55}$$

Combining Eqs. 2.54 and 2.55, one gets:

$$D_t = \boldsymbol{\sigma} : \dot{\boldsymbol{\epsilon}} - (\dot{\mathcal{L}} + \dot{T}s) - \frac{\mathbf{q}\nabla T}{T} \geq 0 \tag{2.56}$$

where D_t is the total dissipation. Assuming $D_t = D_i + D_h$ both intrinsic dissipation D_i and heat dissipation D_h are non-negative:

$$D_i = \boldsymbol{\sigma} : \dot{\boldsymbol{\epsilon}} - (\dot{\mathcal{L}} + \dot{T}s) \geq 0, \tag{2.57}$$

$$D_h = \frac{\mathbf{q}\nabla T}{T} \geq 0. \tag{2.58}$$

Reevaluating $\dot{\mathcal{L}}$ and rearranging D_i:

$$D_i = \boldsymbol{\sigma} : \dot{\boldsymbol{\epsilon}} - \frac{\partial \mathcal{L}}{\partial \boldsymbol{\epsilon}}\dot{\boldsymbol{\epsilon}} - \frac{\partial \mathcal{L}}{\partial z}\dot{z} - \frac{\partial \mathcal{L}}{\partial \boldsymbol{\epsilon}_{ori}}\dot{\boldsymbol{\epsilon}}_{ori} - \frac{\partial \mathcal{L}}{\partial T}\dot{T} - s\dot{T} \tag{2.59}$$

Because $\frac{\partial \mathcal{L}}{\partial \boldsymbol{\epsilon}} = \boldsymbol{\sigma}$, $\frac{\partial \mathcal{L}}{\partial T} = -s$ and $-\frac{\partial \mathcal{L}}{\partial z} = \mathcal{A}_z$, $-\frac{\partial \mathcal{L}}{\partial \epsilon_{ori}} = \mathcal{A}_{ori}$ the intrinsic dissipation D_i can be rewritten as follows:

$$D = D_i = \mathcal{A}_z\dot{z} + \mathcal{A}_{ori} : \dot{\boldsymbol{\epsilon}}_{ori} \geq 0 \tag{2.60}$$

In classical thermodynamics, dissipation D is non-negative, and in an irreversible process it can be written as follows in general form (in Eq. 2.60 it was derived):

$$D = -\frac{\partial W}{\partial \alpha_i}\dot{\alpha}_i \tag{2.61}$$

$$\mathcal{A}_{\alpha i} = -\frac{\partial W}{\partial \alpha_i} \tag{2.62}$$

where $\mathcal{A}_{\alpha i}$ is the thermodynamic force associated with the dissipative variable α_i.

A dissipative mechanism is defined assuming the existence of a function $\mathcal{D}(\alpha, \dot{\alpha})$ defined for all $\dot{\alpha}$, convex with respect to α and zero at $\dot{\alpha} = 0$ (we have to come up with a $\mathcal{D}$ to obtain the thermodynamic forces). If $\mathcal{D}$ is differentiable over all $\dot{\alpha}$.

$$\mathcal{A} = \frac{\partial \mathcal{D}(\dot{\alpha})}{\partial \dot{\alpha}} \tag{2.63}$$

The dual function $\mathcal{D}^*$ is obtained using Legendre-Fenchel transform of $\mathcal{D}$ [52].

$$\mathcal{D}^* = sup[A\dot{\alpha} - \mathcal{D}(\dot{\alpha})]. \tag{2.64}$$

where,

$$\mathcal{A} \in \partial_{\dot{\alpha}} \mathcal{D}(\dot{\alpha}), \qquad \dot{\alpha} =\in \partial_A \mathcal{D}^*(\mathcal{A}) \tag{2.65}$$

$$\mathcal{A}\dot{\alpha} = \mathcal{D}(\dot{\alpha}) + \mathcal{D}^*(\mathcal{A}) \tag{2.66}$$

which ensure the positivity of $\mathcal{A}\dot{\alpha}$.

The pseudo-potential of dissipation $\mathcal{D}$, is non-negative, lower semi-continuous and convex with respect to fluxes of dissipative variables (z and $\boldsymbol{\epsilon}_{ori}$). The pseudo-potential of dissipation $\mathcal{D}$, is written as follows [6]:

$$\mathcal{D} = P(z, \dot{z})\dot{z} + R(z)[\dot{\boldsymbol{\epsilon}}_{ori}]_{eq}. \tag{2.67}$$

$$P(z, \dot{z}) = [a(1 - z) + bz]sgn\dot{z} \tag{2.68}$$

$$R(z) = z^2 Y \tag{2.69}$$

$$\mathcal{D} = \mathcal{D}(z, \dot{z}, \dot{\boldsymbol{\epsilon}}_{ori}) = [(a(1-z) + bz) sgn\dot{z}]\dot{z} + z^2 Y \sqrt{\frac{2}{3}\dot{\boldsymbol{\epsilon}}_{ori} : \dot{\boldsymbol{\epsilon}}_{ori}} \tag{2.70}$$

where $sgn\dot{z}$ is $\dot{z}/|\dot{z}|$ and,

- $sgn\dot{z} = 1 \qquad if \quad \dot{z} > 0,$
- $sgn\dot{z} = -1 \qquad if \quad \dot{z} < 0,$
- $sgn\dot{z} = 0 \qquad if \quad \dot{z} = 0$

a, b and Y are positive material constants.

The evolution of dissipative variables z and ϵ_{ori} and their yield functions can be written as:

- For forward transformation ($\dot{z} \geq 0$), $F_z^1 = -\frac{\partial \mathcal{D}}{\partial \dot{z}} + \mathcal{A}_z \leq 0,$

$$\begin{aligned}
\mathcal{F}_z^1 &= \mathcal{A}_z - a(1-z) - bz \leq 0 \\
&= \frac{1}{2}[(\boldsymbol{\epsilon}_A : \boldsymbol{K}_A : \boldsymbol{\epsilon}_A) - (\boldsymbol{\epsilon}_M - \boldsymbol{\epsilon}_{ori}) : \boldsymbol{K}_M : (\boldsymbol{\epsilon}_M - \boldsymbol{\epsilon}_{ori})] \\
&\quad - C(T) - (G+b)z - a(1-z) \\
&\quad - [(\alpha - \beta)z + \frac{\beta}{2}](\frac{2}{3}\boldsymbol{\epsilon}_{ori} : \boldsymbol{\epsilon}_{ori}) - \boldsymbol{\lambda} : (\boldsymbol{\epsilon}_A - \boldsymbol{\epsilon}_M)
\end{aligned} \tag{2.71}$$

- For reverse transformation ($\dot{z} \leq 0$), $F_z^2 = \frac{\partial \mathcal{D}}{\partial \dot{z}} - \mathcal{A}_z \leq 0,$

$$\begin{aligned}
\mathcal{F}_z^2 &= -\mathcal{A}_z - a(1-z) - bz \leq 0 \\
&= -\frac{1}{2}[(\boldsymbol{\epsilon}_A : \boldsymbol{K}_A : \boldsymbol{\epsilon}_A) - (\boldsymbol{\epsilon}_M - \boldsymbol{\epsilon}_{ori}) : \boldsymbol{K}_M : (\boldsymbol{\epsilon}_M - \boldsymbol{\epsilon}_{ori})] \\
&\quad + C(T) + (G-b)z - a(1-z) \\
&\quad + [(\alpha - \beta)z + \frac{\beta}{2}](\frac{2}{3}\boldsymbol{\epsilon}_{ori} : \boldsymbol{\epsilon}_{ori}) - \boldsymbol{\lambda} : (\boldsymbol{\epsilon}_A - \boldsymbol{\epsilon}_M)
\end{aligned} \tag{2.72}$$

- For martensite orientation, $F_{tr} = -\frac{\partial \mathcal{D}}{\partial \dot{\boldsymbol{\epsilon}}_{ori}} + \mathcal{A}_{ori} \leq 0$,

$$\mathcal{F}_{tr} = |\mathcal{A}_{ori}|_{VM} - z^2 Y \leq 0 \tag{2.73}$$

Here VM operator is the von Mises equivalent of tensor explained in Appendix. For $0 \leq z \leq 1$, $\boldsymbol{\epsilon}_A$ and $\boldsymbol{\epsilon}_M$ can be written as:

$$\boldsymbol{\epsilon}_A = \boldsymbol{S}_A : \boldsymbol{\sigma}, \tag{2.74}$$

$$\boldsymbol{\epsilon}_M = \boldsymbol{S}_M : \boldsymbol{\sigma} + \boldsymbol{\epsilon}_{ori}, \tag{2.75}$$

where $\boldsymbol{S}_A$ and $\boldsymbol{S}_M$ are the compliance tensors of austenite and martensite. Austenite and martensite are assumed to be homogeneous and isotropic with equal Poisson's ratios ν:

$$\nu_A = \nu_M = \nu. \tag{2.76}$$

Using Eqs. 2.74 and 2.75:

$$\boldsymbol{\epsilon}_A = El_A \boldsymbol{\sigma} + P_A (tr\boldsymbol{\sigma})\mathbf{I} \tag{2.77}$$

$$\boldsymbol{\epsilon}_M = El_M \boldsymbol{\sigma} + P_M (tr\boldsymbol{\sigma})\mathbf{I} + \boldsymbol{\epsilon}_{ori} \tag{2.78}$$

where E_A and E_M are the elastic moduli of austenite and martensite and

$$El_A = \frac{1+v}{E_A}, \qquad El_M = \frac{1+v}{E_M}, \qquad El_{MA} = El_M - El_A, \tag{2.79}$$

$$P_A = \frac{-v}{E_A}, \qquad P_M = \frac{-v}{E_M}, \qquad P_{MA} = P_M - P_A, \tag{2.80}$$

$\mathbf{I}$ being identity matrix and $tr(\boldsymbol{\sigma})$ is the trace tensor of $\boldsymbol{\sigma}$. For $0 \leq z \leq 1$ transformation functions can be simplified as follows:

$$\begin{aligned}\mathcal{F}_z^1 = &[\frac{1}{3}El_{MA}\sigma_{VM}^2 + \frac{1}{2}(\frac{1}{3}El_{MA} + P_{MA})(tr\boldsymbol{\sigma})^2 - C(T)] + \boldsymbol{\sigma} : \boldsymbol{\epsilon}_{ori} \\ &- (G+b)z - a(1-z) - [(\alpha-\beta)z + \frac{\beta}{2}](\frac{2}{3}\boldsymbol{\epsilon}_{ori} : \boldsymbol{\epsilon}_{ori}),\end{aligned} \tag{2.81}$$

$$\begin{aligned}\mathcal{F}_z^2 = &-[\frac{1}{3}El_{MA}\sigma_{VM}^2 + \frac{1}{2}(\frac{1}{3}El_{MA} + P_{MA})(tr\boldsymbol{\sigma})^2 - C(T)] - \boldsymbol{\sigma} : \boldsymbol{\epsilon}_{ori} \\ &+ (G-b)z - a(1-z) + [(\alpha-\beta)z + \frac{\beta}{2}](\frac{2}{3}\boldsymbol{\epsilon}_{ori} : \boldsymbol{\epsilon}_{ori}),\end{aligned} \tag{2.82}$$

$$\mathcal{F}_{ori} = \frac{\mathcal{F}_{tr}}{z} = \sigma^{eq} - \frac{2}{3}[(\alpha z + \beta(1-z))\epsilon_{ori}^{eq}] - \frac{2\mu}{3z}\frac{\epsilon_{ori}^{eq}}{\sqrt{\frac{2}{3}\boldsymbol{\epsilon}_{ori} : \boldsymbol{\epsilon}_{ori}}} - zY \tag{2.83}$$

Martensite is assumed to be totally detwinned (oriented) upon transformation. Since $\mathcal{F}_{ori}$ resembles the von Mises function of an elastoplastic material with kinematic hardening equivalent von Mises stresses and strains are used.

$$\mathcal{F}_{ori} = X_{VM} - zY \text{ where } \boldsymbol{X} = \boldsymbol{s} - \frac{2}{3\epsilon_0^2}(\boldsymbol{s} : \boldsymbol{\epsilon}_{ori}) : \boldsymbol{\epsilon}_{ori} \tag{2.84}$$

where $\boldsymbol{s}$ is the deviatoric stress tensor. In the model the transformation occurs when transformation functions, $\mathcal{F}_z$ and $\mathcal{F}_{ori}$, are equal to zero.

- If $\mathcal{F}_z^1 < 0$ and $\mathcal{F}_z^2 < 0$ then $\dot{z} = 0$
- When forward transformation yield surface is reached $\mathcal{F}_z^1$ becomes zero. Therefore $\dot{z}$ is given by the condition $\mathcal{F}_z^1 = 0$.
- If reverse transformation yield surface is reached $\mathcal{F}_z^2$ becomes equal to zero. Therefore $\dot{z}$ is given by the condition $\mathcal{F}_z^2 = 0$.

In theory of plasticity, plastic strain increment and deviatoric stress tensor are assumed to have the same principal directions which is known as flow rule. Inspired from the flow rule and plastic potential, condition for the martensite detwinning and reorientation is the following:

$$\mathcal{F}_{ori} \leq 0, \quad \eta \geq 0, \quad \eta \mathcal{F}_{ori} = 0 \tag{2.85}$$

where η is the inelastic multiplier for martensite reorientation, and obeying the normality rule $\dot{\epsilon}_{ori}$ can be written as:

$$\dot{\boldsymbol{\epsilon}}_{ori} = \eta \frac{\partial \mathcal{F}_{ori}}{\partial \boldsymbol{X}} = \frac{3}{2} \eta \frac{\boldsymbol{X}}{X_{VM}} = \eta N \tag{2.86}$$

where $N = \frac{3}{2} \frac{\boldsymbol{X}}{X_{VM}}$ is the direction vector of $\dot{\boldsymbol{\epsilon}}_{ori}$ in strain space.

2.7. Determination and Identification of Parameters in the Constitutive Model

The parameters used in the model are the elastic moduli of austenite and martensite, E_A and E_M; Poisson's ratio v; the maximum orientation strain, ϵ_0; the material parameters $a,\ b,\ Y,\ \alpha,\ \beta,\ \kappa,\ \zeta,\ G,\ A_f^0$ which will be explained in this section.

E_A is obtained from a tensile test as shown by Mutlu [9], and v is taken from the literature [6]. The phase transition temperatures $M_s^0, M_f^0, A_s^0, A_f^0$ are found from Differential Scanning Calorimetry (DSC).

2.7.1. Orientation of Twinned Martensite and Determination of Y, α and β

The orientation experiment is conducted at a temperature below martensite finish temperature M_f^0 without initial loading so that the alloy is in twinned martensitic state ($z = 1$). The specimen is then loaded uniaxially and the stress-strain diagram shown in Fig. 2.4 is obtained.

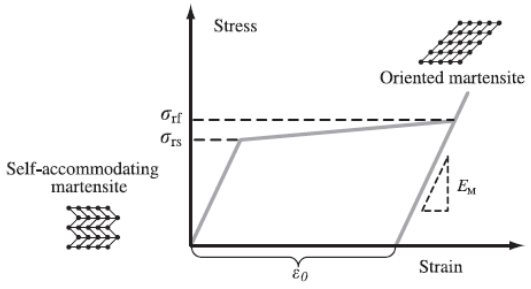

Figure 2.4. Measurement of Orientation Stresses σ_{rs}, σ_{rf}, Elastic Modulus of Martensite E_M and Maximum Orientation Strain ϵ_0 from Orientation Experiment [6].

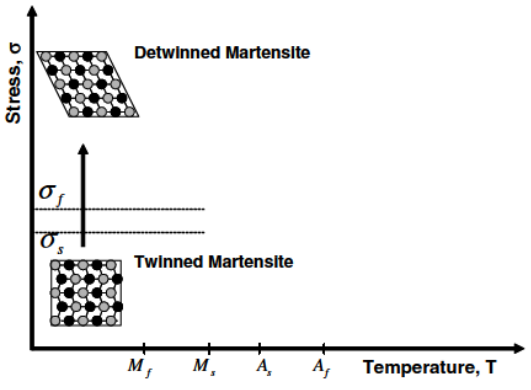

Figure 2.5. Detwinning of Martensite Variants Under Applied Stress, T is Below M_f^0 [2].

In this case, using von Mises formulation, the equivalent inelastic strain is equal to $\epsilon_{ori}^{eq} = \sqrt{\frac{2}{3}\boldsymbol{\epsilon}_{ori} : \boldsymbol{\epsilon}_{ori}}$ with maximum value of ϵ_0.

During martensite orientation, the alloy is made up of fully martensite with $z = 1$ and $\mathcal{F}_{ori} = 0$. Using Eq. 2.83:

$$|\boldsymbol{\sigma} - \frac{2}{3}\alpha\boldsymbol{\epsilon}_{ori} - \frac{2\mu}{3}\frac{\boldsymbol{\epsilon}_{ori}}{\sqrt{\boldsymbol{\epsilon}_{ori} : \boldsymbol{\epsilon}_{ori}}}|_{VM} - Y = 0 \tag{2.87}$$

At σ_{rs}, the detwinning of twinned martensite has just started and the orientation strain ϵ_{ori}^{eq} is zero. Using $z = 1$ and $\epsilon_{ori}^{eq} = 0$ and Eq. 2.83, one gets:

$$\sigma_{rs} = Y \tag{2.88}$$

Physically, Y is the orientation stress (yield stress) of twinned martensite in tension. Just at σ_{rf} where orientation transformation ends, $\epsilon_{ori}^{eq} = \epsilon_0$, μ is zero and Eq.2.83 leads to:

$$\sigma_{rf} - \alpha\epsilon_0 = \sigma_{rs}, \tag{2.89}$$

$$\alpha = \frac{\sigma_{rf} - \sigma_{rs}}{\epsilon_0}. \tag{2.90}$$

α is the slope of stress strain curve during martensite orientation. If austenite transforms directly into detwinned martensite for stresses higher then σ_{rf} and $z = 0$

$$\beta = \frac{\sigma_{rf}}{\epsilon_0}. \tag{2.91}$$

2.7.2. Pseudoelastic Experiment and the Determination of a, b, G, κ, ζ

In this experiment, the SMA is subjected to tensile loading-unloading at temperature T_0, $T_0 > A_f^0$. T_0 is assumed to be high enough so that when the transformation start stress is higher than σ_{rf} with following phase transformation, detwinned martensite forms and $\epsilon_0 = \sqrt{\frac{2}{3}\boldsymbol{\epsilon}_{ori} : \boldsymbol{\epsilon}_{ori}}$. The pseudoelastic experiment is plotted in Figure 2.6 where $\sigma_{ms}, \sigma_{mf}, \sigma_{as}, \sigma_{af}$ are phase change start and finish stress for forward and reverse transformations.

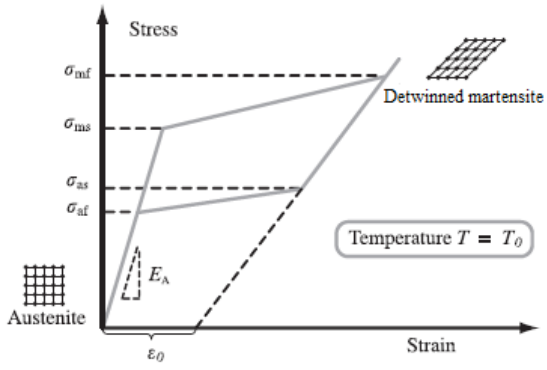

Figure 2.6. Stress-Strain Response of an SMA Under Pseudoelastic Uniaxial Loading.

σ_{ms} represents the beginning of martensitic transformation ($z = 0$); transformation function in Eq. 2.81, $\mathcal{F}_z^1 = 0$:

$$(\frac{1}{E_M} - \frac{1}{E_A})\frac{\sigma_{ms}^2}{2} - C(T_0) + \sigma_{ms}\epsilon_0 - a - \frac{\beta}{2}\epsilon_0^2 = 0 \tag{2.92}$$

At the end of transformation σ_{mf} is reached and $z = 1$. Therefore $\mathcal{F}_z^1$ is rewritten as:

$$(\frac{1}{E_M} - \frac{1}{E_A})\frac{\sigma_{mf}^2}{2} - C(T_0) + \sigma_{mf}\epsilon_0 - (G + b) - (\alpha - \frac{\beta}{2})\epsilon_0^2 = 0 \tag{2.93}$$

Upon unloading when σ_{as} is reached, $z = 1$ and the reverse transformation function in Eq. 2.82 gets the following form:

$$-(\frac{1}{E_M} - \frac{1}{E_A})\frac{\sigma_{as}^2}{2} + C(T_0) - \sigma_{as}\epsilon_0 + (G - b) + (\alpha - \frac{\beta}{2})\epsilon_0^2 = 0 \tag{2.94}$$

At the end of austenite transformation $z = 0$ and σ_{af}, Eq. 2.82 becomes:

$$-(\frac{1}{E_M} - \frac{1}{E_A})\frac{\sigma_{af}^2}{2} + C(T_0) - \sigma_{af}\epsilon_0 - a + (\frac{\beta}{2})\epsilon_0^2 = 0 \tag{2.95}$$

Note that equations above are obtained assuming that there is no change in temperature, and $T = T_0$ during transformation. Adding Eqs. 2.92 and 2.95 one gets the material parameter a:

$$a = \frac{1}{2}[(\frac{1}{E_M} - \frac{1}{E_A})\frac{\sigma_{ms}^2 - \sigma_{af}^2}{2} + (\sigma_{ms} - \sigma_{af})\epsilon_0] \tag{2.96}$$

Similarly adding Eqs. 2.93 and 2.94 one gets b:

$$b = \frac{1}{2}[(\frac{1}{E_M} - \frac{1}{E_A})\frac{\sigma_{mf}^2 - \sigma_{as}^2}{2} + (\sigma_{mf} - \sigma_{as})\epsilon_0] \tag{2.97}$$

To find G, Eqs. 2.92 and 2.94 are subtracted from sum of Eqs. 2.93 and 2.95, and:

$$G = \frac{1}{2}[(\frac{1}{E_M} - \frac{1}{E_A})\frac{\sigma_{mf}^2 - \sigma_{ms}^2 + \sigma_{as}^2 - \sigma_{af}^2}{2} + (\sigma_{mf} - \sigma_{ms} + \sigma_{as} - \sigma_{af})\epsilon_0 - 2(\alpha - \beta)\epsilon_0^2] \tag{2.98}$$

a depends on the difference between the forward transformation start stress σ_{ms} and reverse transformation finish stress σ_{af}; b depends on the forward transformation finish stress σ_{mf} and reverse transformation start stress σ_{as}. G is related to the interaction between martensite plates which affects the slope of stress-strain plateau during transformation.

Similarly to find $C(T_0)$, Eq. 2.95 is subtracted from Eq. 2.92.

$$C(T_0) = \frac{1}{2}[(\frac{1}{E_M} - \frac{1}{E_A})\frac{\sigma_{ms}^2 + \sigma_{af}^2}{2} + (\sigma_{ms} + \sigma_{af})\epsilon_0 - \beta\epsilon_0^2] \tag{2.99}$$

To find remaining material properties κ and ζ in $C(T) = \zeta(T - A_f^0) + \kappa$ the specimen is unloaded to zero stress at $T = A_f^0$ shown in the Fig. 2.7:

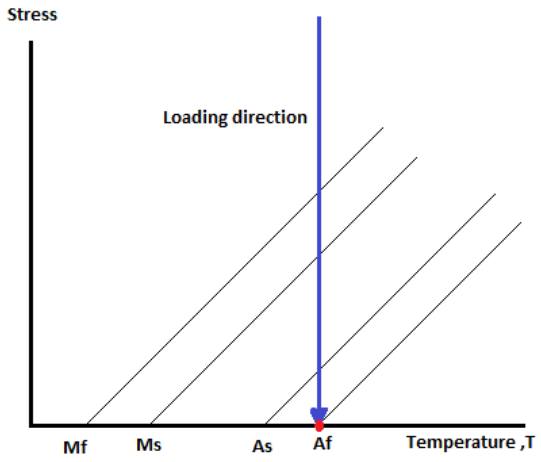

Figure 2.7. Stress-Temperature State at the End of Reverse Transformation

A_f^0 is the austenite finish temperature at reverse transformation under zero stress that is obtained from DSC. Using Eq. 2.95 for fully orientated martensite at temperature A_f^0, with $\sigma = 0$: $\mathcal{F}_z^2 = 0$, $z = 0$, and $\sqrt{\frac{2}{3}\boldsymbol{\epsilon}_{ori} : \boldsymbol{\epsilon}_{ori}} = \epsilon_0$:

$$C(A_f^0) = a - \beta\frac{\epsilon_0^2}{2} \tag{2.100}$$

is obtained. Using Eq. 2.24, κ is found as follows:

$$\kappa = a - \beta\frac{\epsilon_0^2}{2} \tag{2.101}$$

Knowing the value of $C(T_0)$ from Eq. 2.99, and κ from Eq. 2.101, ζ can be found as follows:

$$C(T_0) = \zeta(T_0 - A_f^0) + \kappa \tag{2.102}$$

$$\zeta = \frac{C(T_0) - \kappa}{T_0 - A_f^0} \tag{2.103}$$

2.8. Addition of Thermomechanical Coupling

The model explained above [6], successfully reflects the superelasticity, self accommodation of martensite (twinning), orientation of self-accommodation of martensite (detwinning) and one-way shape memory phenomena of SMAs in 3D at constant temperature. However thermomechanical coupling and temperature change due to transformation is not included in this model. During forward transformation, heat is generated which may increase the temperature of the SMA depending on heat transfer rate. At higher temperatures, austenite becomes more stable, and higher stress is required to carry forward transformation. During reverse transformation, due to latent heat, the temperature of the SMA may decrease depending on heat transfer rate making martensite more stable. In this case, the transformation stress must decrease in order to drive the formation of austenite. To account for the effect of temperature, Morin et. al [7], improved the 3D model of ZM by adding temperature related term to Helmholtz free energy and solving the heat transfer equation. Entropy of the material at constant T, equals to:

$$s = -\frac{\partial \mathcal{L}}{\partial T} = -\zeta z \tag{2.104}$$

ζz comes from the $C(T)$ term. It can be seen that entropy s is directly related to $\frac{\partial C(T)}{\partial T}$ and martensite volume fraction z at constant temperature. When $z = 0$, entropy $s = 0$, meaning the entropy of the austenite is assumed to be reference entropy and is taken as zero. That is the main reason why $C(T)$ is included in the free energy of the martensite. Lagrangian in Eq. 2.34, only includes the phase change at constant temperature. To model the temperature change, free energy density term related to that must be added. Second law of the thermodynamics asserts that:

$$ds = \frac{\delta Q}{T} \tag{2.105}$$

Assuming ρ and C_p do not change with temperature Eq. 2.105 can be written as in integral form:

$$\int_{s_0}^{s} ds = \int_{T_0}^{T} \frac{\rho C_p}{T} dT \tag{2.106}$$

$$s - s_0 = \rho C_p ln(\frac{T}{T_0}) \tag{2.107}$$

s_0 is the reference entropy at T_0 temperature. Eq. 2.107 is the entropy difference caused by the temperature change and entropy can be written as follows:

$$s = -\frac{\partial \mathcal{L}}{\partial T} = \rho C_p ln(\frac{T}{T_0}) + s_0 \tag{2.108}$$

Taking the integral with respect to T:

$$\mathcal{L} = \rho C_p[-Tln(\frac{T}{T_0}) + T + c] + Ts_0 + \mathcal{L}(\boldsymbol{\epsilon}, \boldsymbol{\epsilon}_A, \boldsymbol{\epsilon}_M, \boldsymbol{\epsilon}_{ori}, z) \tag{2.109}$$

$\rho C_p[-Tln(\frac{T}{T_0}) + T + c]$ is the free energy density which stems from the temperature change and equals to zero when $T = T_0$. Using $T = T_0$, c is found to be $c = -T_0$. Free energy term related to temperature change W_T is can be written as:

$$W_T = \rho C_p[T - T_0 - Tln(\frac{T}{T_0})] \tag{2.110}$$

Therefore, the total free energy becomes $W = (1-z)W_A + zW_M + W_{it} + W_T$:

$$\begin{aligned} W &= W(T, \boldsymbol{\epsilon}_A, \boldsymbol{\epsilon}_M, \boldsymbol{\epsilon}_{ori}, z) \\ &= (1-z)[\frac{1}{2}\boldsymbol{\epsilon}_A : \boldsymbol{K}_A : \boldsymbol{\epsilon}_A] + z[\frac{1}{2}(\boldsymbol{\epsilon}_M - \boldsymbol{\epsilon}_{ori}) : \boldsymbol{K}_M : (\boldsymbol{\epsilon}_M - \boldsymbol{\epsilon}_{ori}) \\ &\quad + C(T)] + G\frac{z^2}{2} + \frac{z}{2}[\alpha z + \beta(1-z)](\frac{2}{3}\boldsymbol{\epsilon}_{ori} : \boldsymbol{\epsilon}_{ori}) \\ &\quad + \rho C_p[T - T_0 - Tln(\frac{T}{T_0})] \end{aligned} \tag{2.111}$$

which also modifies the Lagrangian as follows:

$$\begin{aligned}
\mathcal{L} &= W + W_1 = L(\epsilon, \boldsymbol{\epsilon}_A, \boldsymbol{\epsilon}_M, \boldsymbol{\epsilon}_{ori}, T, z) \\
&= (1-z)[\frac{1}{2}\boldsymbol{\epsilon}_A : \boldsymbol{K}_A : \boldsymbol{\epsilon}_A] \\
&\quad + z[\frac{1}{2}(\boldsymbol{\epsilon}_M - \boldsymbol{\epsilon}_{ori}) : \boldsymbol{K}_M : (\boldsymbol{\epsilon}_M - \boldsymbol{\epsilon}_{ori}) + C(T)] \\
&\quad + G\frac{z^2}{2} + \frac{z}{2}[\alpha z + \beta(1-z)](\frac{2}{3}\boldsymbol{\epsilon}_{ori} : \boldsymbol{\epsilon}_{ori}) \\
&\quad + \rho C_p[T - T_0 - Tln(\frac{T}{T_0})] - \boldsymbol{\lambda} : [(1-z)\boldsymbol{\epsilon}_A + z\boldsymbol{\epsilon}_M - \epsilon] \\
&\quad - \mu(\epsilon_0 - \sqrt{\frac{2}{3}\boldsymbol{\epsilon}_{ori} : \boldsymbol{\epsilon}_{ori}}) - v_1 z - v_2(1-z)
\end{aligned} \tag{2.112}$$

which differs from Eq. 2.34 by the addition of the free energy term related to temperature in Eq. 2.110.

2.8.1. Heat Equation

Addition of heat capacity modifies the entropy as follows:

$$s = \frac{\partial \mathcal{L}}{\partial T} = \rho C_p ln(\frac{T}{T_0}) - \zeta z \tag{2.113}$$

From Eqs. 2.55 and 2.57, D_i can also be written as:

$$D_i = T\dot{s} + div\mathbf{q} - r \tag{2.114}$$

using,

$$s = -\frac{\partial \mathcal{L}}{\partial T}\ ,\ \dot{s} = -\frac{\partial^2 \mathcal{L}}{\partial T \partial \boldsymbol{\epsilon}} : \dot{\boldsymbol{\epsilon}} - \frac{\partial^2 \mathcal{L}}{\partial T \partial \boldsymbol{\epsilon}_{ori}} : \dot{\boldsymbol{\epsilon}}_{ori} - \frac{\partial^2 \mathcal{L}}{\partial T \partial z}\dot{z} - \frac{\partial^2 \mathcal{L}}{\partial T^2}\dot{T} \tag{2.115}$$

Eq. 2.114 becomes:

$$D_i = T\dot{s} + div\mathbf{q} - r = -T\frac{\partial^2 \mathcal{L}}{\partial T \partial \boldsymbol{\epsilon}} : \dot{\boldsymbol{\epsilon}} - T\frac{\partial^2 \mathcal{L}}{\partial T \partial \boldsymbol{\epsilon}_{ori}} : \dot{\boldsymbol{\epsilon}}_{ori} - T\frac{\partial^2 \mathcal{L}}{\partial T \partial z}\dot{z} - T\frac{\partial^2 \mathcal{L}}{\partial T^2}\dot{T} + div\mathbf{q} - r \tag{2.116}$$

The $\dot{\boldsymbol{\epsilon}}$ term represents thermoelastic effects and can be neglected. Using Fourier's law of heat conduction, heat equation is obtained:

$$\rho C_p \dot{T} - div(k\nabla T) = -T\frac{\partial A_{ori}}{\partial T} : \dot{\boldsymbol{\epsilon}}_{ori} - T\frac{\partial A_z}{\partial T}\dot{z} + r + D_i \tag{2.117}$$

If only the heat generation due to phase change is taken into account, the term associated with $\boldsymbol{\epsilon}_{ori}$ can be neglected. Because $\mathcal{A}_z$ is a subgradient of pseudopotential of dissipation associated with z using Eq. 2.41, Eq. 2.117 becomes:

$$\rho C_p \dot{T} - div(k\nabla T) = T\frac{\partial C(T)}{\partial T}\dot{z} + [a(1-z) + bz]|\dot{z}| \tag{2.118}$$

2.9. Effect of Thermal Strain

With the addition of thermomechanical coupling, temperature of the material might change resulting in a thermal strain $\boldsymbol{\epsilon}_T$ which can be written as sum of thermal strains of austenite and martensite $\boldsymbol{\epsilon}_{TA}$ and $\boldsymbol{\epsilon}_{TM}$ given as follows:

$$\boldsymbol{\epsilon}_{TA} = \boldsymbol{\alpha}_A(T - T_0) \tag{2.119}$$

$$\boldsymbol{\epsilon}_{TM} = \boldsymbol{\alpha}_M(T - T_0) \tag{2.120}$$

where T is the material temperature T_0 is the reference temperature, $\boldsymbol{\alpha}_A$ and $\boldsymbol{\alpha}_M$ are the thermal expansion coefficients of austenite and martensite respectively. Including thermal strains, free energy density of austenite and martensite are modified as follows:

$$W_A = W_A(\boldsymbol{\epsilon}_A) = \frac{1}{2}(\boldsymbol{\epsilon}_A - \boldsymbol{\alpha}_A(T - T_0)) : \boldsymbol{K}_A : (\boldsymbol{\epsilon}_A - \boldsymbol{\alpha}_A(T - T_0)) \tag{2.121}$$

$$
\begin{aligned}
W_M &= W_M(\boldsymbol{\epsilon}_M, \boldsymbol{\epsilon}_{ori}, T) \\
&= \frac{1}{2}(\boldsymbol{\epsilon}_M - \boldsymbol{\epsilon}_{ori} - \boldsymbol{\alpha}_M(T - T_0)) : \boldsymbol{K}_M : (\boldsymbol{\epsilon}_M - \boldsymbol{\epsilon}_{ori} - \boldsymbol{\alpha}_M(T - T_0)) + C(T)
\end{aligned} \tag{2.122}
$$

Helmholtz Free energy, W, becomes:

$$
\begin{aligned}
W = \ & W(z, \boldsymbol{\epsilon}_A, \boldsymbol{\epsilon}_M, \boldsymbol{\epsilon}_{ori}, T) \\
= \ & (1 - z)[\frac{1}{2}(\boldsymbol{\epsilon}_A - \boldsymbol{\alpha}_A(T - T_0)) : \boldsymbol{K}_A : (\boldsymbol{\epsilon}_A - \boldsymbol{\alpha}_A(T - T_0))] \\
& + z[\frac{1}{2}(\boldsymbol{\epsilon}_M - \boldsymbol{\epsilon}_{ori} - \boldsymbol{\alpha}_M(T - T_0)) : \boldsymbol{K}_M : (\boldsymbol{\epsilon}_M - \boldsymbol{\epsilon}_{ori} - \boldsymbol{\alpha}_M(T - T_0)) + C(T)] \\
& + G\frac{z^2}{2} + \frac{z}{2}[\alpha z + \beta(1 - z)](\frac{2}{3}\boldsymbol{\epsilon}_{ori} : \boldsymbol{\epsilon}_{ori}) \\
& + \rho C_p[T - T_0 - Tln(\frac{T}{T_0})]
\end{aligned} \tag{2.123}
$$

Lagrangian $\mathcal{L} = W + W_1$ takes the following form:

$$
\begin{aligned}
\mathcal{L} = \ & \mathcal{L}(z, \boldsymbol{\epsilon}_A, \boldsymbol{\epsilon}_M, \boldsymbol{\epsilon}_{ori}, T) \\
= \ & (1 - z)[\frac{1}{2}(\boldsymbol{\epsilon}_A - \boldsymbol{\alpha}_A(T - T_0)) : \boldsymbol{K}_A : (\boldsymbol{\epsilon}_A - \boldsymbol{\alpha}_A(T - T_0))] \\
& + z[\frac{1}{2}(\boldsymbol{\epsilon}_M - \boldsymbol{\epsilon}_{ori} - \boldsymbol{\alpha}_M(T - T_0)) : \boldsymbol{K}_M : (\boldsymbol{\epsilon}_M - \boldsymbol{\epsilon}_{ori} - \boldsymbol{\alpha}_M(T - T_0)) + C(T)] \\
& + G\frac{z^2}{2} + \frac{z}{2}[\alpha z + \beta(1 - z)](\frac{2}{3}\boldsymbol{\epsilon}_{ori} : \boldsymbol{\epsilon}_{ori}) + \rho C_p[T - T_0 - Tln(\frac{T}{T_0})] \\
& - \boldsymbol{\lambda} : [(1 - z)\boldsymbol{\epsilon}_A + z\boldsymbol{\epsilon}_M - \boldsymbol{\epsilon}] - \mu(\epsilon_0 - \sqrt{\frac{2}{3}\boldsymbol{\epsilon}_{ori} : \boldsymbol{\epsilon}_{ori}}) - v_1 z - v_2(1 - z)
\end{aligned} \tag{2.124}
$$

Thermodynamic forces A_z and A_{ori} becomes:

$$
\begin{aligned}
-\frac{\partial \mathcal{L}}{\partial z} = A_z = \frac{1}{2}[&(\boldsymbol{\epsilon}_A - \boldsymbol{\alpha}_A(T-T_0)) : \boldsymbol{K}_A : (\boldsymbol{\epsilon}_A - \boldsymbol{\alpha}_A(T-T_0)) \\
&- (\boldsymbol{\epsilon}_M - \boldsymbol{\epsilon}_{ori} - \boldsymbol{\alpha}_M(T-T_0)) : \boldsymbol{K}_M : (\boldsymbol{\epsilon}_M - \boldsymbol{\epsilon}_{ori} - \boldsymbol{\alpha}_M(T-T_0))] - C(T) \\
&- Gz - [(\alpha-\beta)z + \frac{\beta}{2}](\frac{2}{3}\boldsymbol{\epsilon}_{ori} : \boldsymbol{\epsilon}_{ori}) - \boldsymbol{\lambda} : (\boldsymbol{\epsilon}_A - \boldsymbol{\epsilon}_M) \qquad (2.125) \\
-\frac{\partial \mathcal{L}}{\partial \boldsymbol{\epsilon}_{ori}} = A_{ori} = z[&\boldsymbol{K}_M : (\boldsymbol{\epsilon}_M - \boldsymbol{\epsilon}_{ori} - \boldsymbol{\alpha}_M(T-T_0)) - \frac{2}{3}[\alpha z + \beta(1-z)]\boldsymbol{\epsilon}_{ori}] \\
&- \frac{2\mu}{3}\frac{\boldsymbol{\epsilon}_{ori}}{\sqrt{\frac{2}{3}\boldsymbol{\epsilon}_{ori} : \boldsymbol{\epsilon}_{ori}}} \qquad (2.126)
\end{aligned}
$$

Stress-strain relation becomes:

$$
\boldsymbol{\sigma} = \boldsymbol{K} : [\boldsymbol{\epsilon} - z\boldsymbol{\epsilon}_{ori} - \boldsymbol{\alpha}_{eq}(T-T_0)] \qquad (2.127)
$$

where,

$$
\boldsymbol{\alpha}_{eq} = (1-z)\boldsymbol{\alpha}_A + z\boldsymbol{\alpha}_M \qquad (2.128)
$$

Forward, reverse and orientation transformation functions slightly change after the addition of thermal strain effects and thermomechanical coupling:

- For forward transformation ($\dot{z} \geq 0$),

$$
\begin{aligned}
\mathcal{F}_z^1 = \frac{1}{2}[&(\boldsymbol{\epsilon}_A - \boldsymbol{\alpha}_A(T-T_0)) : \boldsymbol{K}_A : (\boldsymbol{\epsilon}_A - \boldsymbol{\alpha}_A(T-T_0))] \\
&- (\boldsymbol{\epsilon}_M - \boldsymbol{\epsilon}_{ori} - \boldsymbol{\alpha}_M(T-T_0)) : \boldsymbol{K}_M : (\boldsymbol{\epsilon}_M - \boldsymbol{\epsilon}_{ori} - \boldsymbol{\alpha}_M(T-T_0))] \\
&- C(T) - (G+b)z - a(1-z) \\
&- [(\alpha-\beta)z + \frac{\beta}{2}](\frac{2}{3}\boldsymbol{\epsilon}_{ori} : \boldsymbol{\epsilon}_{ori}) - \boldsymbol{\lambda} : (\boldsymbol{\epsilon}_A - \boldsymbol{\epsilon}_M) \qquad (2.129)
\end{aligned}
$$

- For reverse transformation ($\dot{z} \leq 0$),

$$\begin{aligned}\mathcal{F}_z^2 = &-\frac{1}{2}[(\boldsymbol{\epsilon}_A - \boldsymbol{\alpha}_A(T-T_0)) : \boldsymbol{K}_A : (\boldsymbol{\epsilon}_A - \boldsymbol{\alpha}_A(T-T_0))] \\ &- (\boldsymbol{\epsilon}_M - \boldsymbol{\epsilon}_{ori} - \boldsymbol{\alpha}_M(T-T_0)) : \boldsymbol{K}_M : (\boldsymbol{\epsilon}_M - \boldsymbol{\epsilon}_{ori} - \boldsymbol{\alpha}_M(T-T_0))] \\ &+ C(T) + (G-b)z - a(1-z) \\ &+ [(\alpha-\beta)z + \frac{\beta}{2}](\frac{2}{3}\boldsymbol{\epsilon}_{ori} : \boldsymbol{\epsilon}_{ori}) - \boldsymbol{\lambda} : (\boldsymbol{\epsilon}_A - \boldsymbol{\epsilon}_M)\end{aligned} \tag{2.130}$$

- For martensite orientation,

$$\mathcal{F}_{ori} = \mathcal{A}_{ori} - z^2 Y \tag{2.131}$$

2.10. Boundaries of the Thermomechanically Coupled Problem

The problem is determining the thermomechanical response of a shape memory alloy body occupying a volume of Ω, subjected to a loading. The body is subjected to body forces $\boldsymbol{f}$ over Ω, and contact forces $\boldsymbol{T}_d$ on $\partial\Omega_T$ and displacement boundary conditions are defined on $\partial\Omega_u$. Convection is considered between the body and the surroundings. The material behavior could be determined solving the following set of equations:

- Static and kinetic admissibility
  $div\boldsymbol{\sigma} - \boldsymbol{f} = 0$ over Ω
  $\boldsymbol{\sigma}.\boldsymbol{n} - \boldsymbol{T}_d = 0$ on $\partial\Omega_T$
  $\boldsymbol{u} - \boldsymbol{u}_d = 0$ on $\partial\Omega_u$
- Strain displacement
  $\boldsymbol{\epsilon} = \frac{1}{2}(\boldsymbol{\nabla u} +^t \boldsymbol{\nabla u})$ over Ω
- Constitutive stress-strain relation $\boldsymbol{\sigma} = \boldsymbol{K} : [\boldsymbol{\epsilon} - z\boldsymbol{\epsilon}_{ori} - \boldsymbol{\alpha}(T-T_0)]$ over Ω where z and $\boldsymbol{\epsilon}_{ori}$ are governed by transformation functions.
- Heat equation $\boldsymbol{q}.\boldsymbol{n} = h(T - T_{ext})$ on $\partial\Omega$
  $T(t=0) = T_{ext}$
  $\rho C_p \dot{T} - div(k\nabla T) = T\frac{\partial^2\mathcal{L}}{\partial T\partial\boldsymbol{\epsilon}_{ori}} : \dot{\boldsymbol{\epsilon}}_{ori} + T\frac{\partial^2\mathcal{L}}{\partial T\partial z}\dot{z} + r + D_i$ over Ω.

where h is the convective heat transfer coefficient same for austenite and martensite phases.

2.11. Plastic Strain as Dissipative Variable

So far behavior of fully transformed martensite is assumed to be elastic. However beyond a certain stress σ_{my}, martensite yields and undergoes an irreversible plastic deformation which causes a heat dissipation. In order to capture the behavior beyond plastic deformation Zaki *et al.* [44] extended the ZM model by adding plastic dissipation term into free energy, however in their publication, thermomechanical coupling is not considered. In this work, the model for the plastic deformation [44] is extended by the addition of thermomechanical coupling and thermal strain.

Helmholtz free energy density of plastic strain W_p is the energy stems from kinematic hardening and can be written as:

$$W_p = \frac{H}{2}(\frac{2}{3}\boldsymbol{\epsilon}_p : \boldsymbol{\epsilon}_p) \tag{2.132}$$

Helmholtz free energy,$W(T, \boldsymbol{\epsilon}_A, \boldsymbol{\epsilon}_M, \boldsymbol{\epsilon}_{ori}, \boldsymbol{\epsilon}_p, z)$ becomes :

$$\begin{aligned} W = (1-z)[\frac{1}{2}(\boldsymbol{\epsilon}_A - \boldsymbol{\epsilon}_p - \boldsymbol{\alpha}_A(T-T_0)) : \boldsymbol{K}_A : (\boldsymbol{\epsilon}_A - \boldsymbol{\epsilon}_p - \boldsymbol{\alpha}_A(T-T_0))] \\ + z[\frac{1}{2}(\boldsymbol{\epsilon}_M - \boldsymbol{\epsilon}_{ori} - \boldsymbol{\epsilon}_p - \boldsymbol{\alpha}_M(T-T_0)) : \boldsymbol{K}_M : (\boldsymbol{\epsilon}_M - \boldsymbol{\epsilon}_{ori} - \boldsymbol{\epsilon}_p - \boldsymbol{\alpha}_M(T-T_0)) \\ + C(T)] + G\frac{z^2}{2} + \frac{z}{2}[\alpha z + \beta(1-z)](\frac{2}{3}\boldsymbol{\epsilon}_{ori} : \boldsymbol{\epsilon}_{ori}) \\ + \rho C_p[T - T_0 - Tln(\frac{T}{T_0})] + \frac{H}{2}(\frac{2}{3}\boldsymbol{\epsilon}_p : \boldsymbol{\epsilon}_p) \end{aligned} \tag{2.133}$$

The modified Lagrangian, $\mathcal{L}(\boldsymbol{\epsilon}, \boldsymbol{\epsilon}_A, \boldsymbol{\epsilon}_M, \boldsymbol{\epsilon}_{ori}, \boldsymbol{\epsilon}_p, T, z)$ is then:

$$\begin{aligned}\mathcal{L} = &(1-z)[\frac{1}{2}(\boldsymbol{\epsilon}_A - \boldsymbol{\epsilon}_p - \boldsymbol{\alpha}_A(T-T_0)) : \boldsymbol{K}_A : (\boldsymbol{\epsilon}_A - \boldsymbol{\epsilon}_p - \boldsymbol{\alpha}_A(T-T_0))] \\ &+ z[\frac{1}{2}(\boldsymbol{\epsilon}_M - \boldsymbol{\epsilon}_{ori} - \boldsymbol{\epsilon}_p - \boldsymbol{\alpha}_M(T-T_0)) : \boldsymbol{K}_M : (\boldsymbol{\epsilon}_M - \boldsymbol{\epsilon}_{ori} - \boldsymbol{\epsilon}_p - \boldsymbol{\alpha}_M(T-T_0)) \\ &+ C(T)] + G\frac{z^2}{2} + \frac{z}{2}[\alpha z + \beta(1-z)](\frac{2}{3}\boldsymbol{\epsilon}_{ori} : \boldsymbol{\epsilon}_{ori}) + \\ &\rho C_p[T - T_0 - Tln(\frac{T}{T_0})] - \boldsymbol{\lambda} : [(1-z)\boldsymbol{\epsilon}_A + z\boldsymbol{\epsilon}_M - \boldsymbol{\epsilon}] \\ &- \mu(\epsilon_0 - \sqrt{\frac{2}{3}\boldsymbol{\epsilon}_{ori}\boldsymbol{\epsilon}_{ori}}) - v_1 z - v_2(1-z) + \frac{H}{2}(\frac{2}{3}\boldsymbol{\epsilon}_p : \boldsymbol{\epsilon}_p)\end{aligned} \tag{2.134}$$

Thermodynamic force associated with plastic strain A_p is obtained as follows:

$$A_p = -\frac{\partial \mathcal{L}}{\partial \boldsymbol{\epsilon}_p} = (1-z)\boldsymbol{K}_A : (\boldsymbol{\epsilon}_A - \boldsymbol{\epsilon}_p) - z\boldsymbol{K}_M : (\boldsymbol{\epsilon}_M - \boldsymbol{\epsilon}_{ori} - \boldsymbol{\epsilon}_p) - \frac{2}{3}H\boldsymbol{\epsilon}_p \tag{2.135}$$

Addition of a new dissipative variable $\boldsymbol{\epsilon}_p$, changes pseudo-potential of dissipation function:

$$\mathcal{D} = D(z, \dot{z}, \dot{\boldsymbol{\epsilon}}_{ori}, \dot{\boldsymbol{\epsilon}}_p) = [(a(1-z)+bz)sgn\dot{z}]\dot{z} + z^2 Y\sqrt{\frac{2}{3}\dot{\boldsymbol{\epsilon}}_{ori} : \dot{\boldsymbol{\epsilon}}_{ori}} + zY_p\sqrt{\frac{2}{3}\dot{\boldsymbol{\epsilon}}_p : \dot{\boldsymbol{\epsilon}}_p} \tag{2.136}$$

Yield function governing plastic deformation is found using thermodynamic force A_p and pseudopotential of dissipation:

$$F_p = |\boldsymbol{\sigma} - \frac{2}{3}H\boldsymbol{\epsilon}_p|_{VM} - zY_p \tag{2.137}$$

Let σ_{ym} and k be the yield stress of martensite and tangent modulus of stress-strain curve beyond yield point. When stress reaches σ_{ym} plastic strain is zero and material is fully martensite and $F_p = 0$. Eq. 2.137 becomes:

$$\sigma_{ym} = Y_p \tag{2.138}$$

During evolution of plastic strain, $F_p = 0$ and $\dot{F}_p = 0$ leads to:

$$\dot{F}_p = \dot{\boldsymbol{\sigma}} - H\dot{\boldsymbol{\epsilon}}_p = 0 \tag{2.139}$$

$$\dot{\boldsymbol{\sigma}} = H\dot{\boldsymbol{\epsilon}}_p \tag{2.140}$$

Recall,

$$\boldsymbol{\sigma} = E_{eq} : (\boldsymbol{\epsilon} - z\boldsymbol{\epsilon}_{ori} - z\boldsymbol{\epsilon}_p) \tag{2.141}$$

change with respect to time during plastic strain evolution and $z = 1$:

$$\dot{\boldsymbol{\sigma}} = E_M(\dot{\boldsymbol{\epsilon}} - \dot{\boldsymbol{\epsilon}}_p) \tag{2.142}$$

Combining Eqs. 2.140 and 2.142:

$$E_M\dot{\boldsymbol{\epsilon}} = \dot{\boldsymbol{\epsilon}}_p(H + E_M) \tag{2.143}$$

$$\dot{\boldsymbol{\epsilon}}_p = \frac{E_M\dot{\boldsymbol{\epsilon}}}{H + E_M} \tag{2.144}$$

Eq. 2.140 in terms of $\dot{\boldsymbol{\epsilon}}$:

$$\dot{\boldsymbol{\sigma}} = \frac{HE_M}{H + E_M}\dot{\boldsymbol{\epsilon}} \tag{2.145}$$

During plastic deformation tangent modulus is equal to:

$$k = \frac{\dot{\boldsymbol{\sigma}}}{\dot{\boldsymbol{\epsilon}}} \tag{2.146}$$

From this relation using Eq. 2.145:

$$k = \frac{HE_M}{H + E_M} \tag{2.147}$$

Material parameter H is obtained:

$$H = \frac{E_M k}{E_M - k} \tag{2.148}$$

2.12. Summary

In this section the ZM constitutive model in which the local behavior of the SMA is rederived in detail (the state equations are derived using Helmholtz free energy potential). The Lagrangian is established using the free energy and the constraints and together with state equations the constitutive relation that is needed is obtained. Following the Lagrangian, a pseudopotential of dissipation $\mathcal{D}$ is derived based on the work of Halphen and Nguyen [37], and the thermodynamic forces governing the evolution of dissipative variables are obtained. Determination and identification of the material parameters and the addition of thermomechanical coupling [7], and thermal strain [43], are explained. Plastic strain [44], is extended to include thermomechanical coupling and thermal strains which is not used further in this thesis. Boundaries of the thermomechanically coupled problem are stated.

3. MODIFICATION OF THE ZM MODEL

In this section the effect of model parameters on the mechanical behavior is discussed in detail. During the derivation of the parameters in Chapter 2, it has been realized that some of the assumptions are simplified for ease of solution and some points have been disregarded. This chapter is dedicated to the influence of model parameters on the mechanical behavior and on their modifications and improvements.

3.1. Effect of Model Parameters on Mechanical Behavior

To improve the model, the effect of parameters used is studied. Inconsistencies in assumptions or weak co-relation between simulation and experimental results are stated and some of them are modified and improved based on experimental findings.

3.1.1. Effect of Phase Change Heat Density, $C(T)$

$C(T)$ represents phase change heat density. It governs the effect of material temperature T, on transformation stresses and strains. Assuming a fully austenitic phase, $z = 0$, Eq. 2.26 takes the following simple form:

$$W = \frac{1}{2}\boldsymbol{\epsilon}_A : \boldsymbol{K}_A : \boldsymbol{\epsilon}_A \tag{3.1}$$

remember that the Helmholtz free energy W is equal to $U - Ts$, combining with 3.1 one gets:

$$U - Ts = \frac{1}{2}\boldsymbol{\epsilon}_A : \boldsymbol{K}_A : \boldsymbol{\epsilon}_A \tag{3.2}$$

Eq. 3.2 is also valid for elastic materials and the change of temperature does not change the righthand side; and lefthand side also does not change since U and s also change with temperature. However when the martensite phase is present, $z \neq 0$, change in U and s does not satisfy the equality with the righthand side. To provide equality

righthand side is altered, $C(T)$ term is added to Eq. 2.23 to account for the phase change heat density. It is a linear function [53], that depends on material temperature T, and other material constants are explained in the previous sections. $C(T)$ is the free energy density of existence of martensite at a specific temperature T, regardless of its deformation and orientation. κ is found by using reverse transformation function Eq. 2.95 at $z = 0$, austenite finish temperature and zero stress.

$C(T)$ is an element in forward and reverse transformation functions, Eqs. 2.81, 2.82 and directly affects the transformation yield surface. Demonstrated by experiments, it is a well known fact that transformation stresses increase when material temperature increases and vice versa. In Eq. 2.81, $C(T)$ takes higher values at higher temperatures, lowering the righthand side of the function. During transformation, F_z^1 is zero, and to balance the decrease due to $C(T)$, stress and strain increase simultaneously in accordance with evolution laws. As result, forward transformation starts at higher strain and stress levels on higher temperatures. Results of numerical simulation can be seen in Section 4.1.

3.1.2. Effect of Interaction Energy W_{it}

Interaction energy, W_{it} has the following form proposed by Muller [51]:

$$W_{it} = Az(1 - z) \geq 0 \tag{3.3}$$

Figure 3.1 shows the relation between martensite volume fraction and interaction energy.

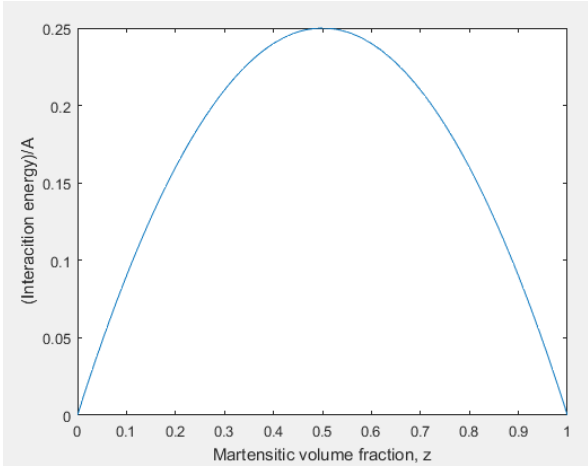

Figure 3.1. W_{it}/A vs Martensite Volume Fraction, z.

At $z = 0.5$, maximum number of interactions occur between martensite and austenite layers. According to this approach, interaction energy W_{it} gets its maximum value when austenitic volume ratio equals to martensitic volume ratio.

In ZM model interaction between martensite variants are also considered since it also contains orientation of martensite. Interaction energy W_{it} is defined as Eq. 2.25. G governs the interaction between martensite variants independent of orientation and affects the slope of stress-strain curve during transformation.

3.2. On Pseudopotential of Dissipation Coefficients a, b and G

a, b and G are the pseudo-potential of dissipation coefficients related to hysteresis loop. They are calculated using transformation functions and experimental data obtained at constant temperature T_0 and given in Eqs. 2.96 - 2.98. First versions of the ZM model are developed without considering thermomechanical coupling at which temperature stays at T_0 during stress induced transformation. Therefore experimental data obtained at T_0 were sufficient to determine a, b and G. With the addition of thermomechanical coupling by Morin *et al.* [7], temperature of the material may change during stress induced transformation depending on heat generation and heat

transfer rate of the SMA. Assume a condition where T_1, T_2, T_3, T_4 are the material temperatures at martensite start, martensite finish, austenite start and austenite finish respectively. Since transformation stresses and temperatures are different than isothermal case, Eqs. 2.92-2.95 change. At the beginning of martensitic transformation, material temperature is T_1 and stress is σ_{ms1} forward transformation function Eq. 2.81 becomes:

$$(\frac{1}{E_M} - \frac{1}{E_A})\frac{\sigma_{ms1}^2}{2} - C(T_1) + \sigma_{ms1}\epsilon_0 - a - \frac{\beta}{2}\epsilon_0^2 = 0 \tag{3.4}$$

At the end of transformation with the modified temperature T_2, σ_{mf2} is reached and $z = 1$. Eq. 2.81 becomes:

$$(\frac{1}{E_M} - \frac{1}{E_A})\frac{\sigma_{mf2}^2}{2} - C(T_2) + \sigma_{mf2}\epsilon_0 - (G + b) - (\alpha - \frac{\beta}{2})\epsilon_0^2 = 0 \tag{3.5}$$

Upon unloading at T_3 when σ_{as3} is reached, $z = 1$ and reverse transformation function in Eq. 2.82 gets the following form:

$$-(\frac{1}{E_M} - \frac{1}{E_A})\frac{\sigma_{as3}^2}{2} + C(T_3) - \sigma_{as3}\epsilon_0 + (G - b) + (\alpha - \frac{\beta}{2})\epsilon_0^2 = 0 \tag{3.6}$$

and for $z = 0$ and T_4 at end of austenite transformation σ_{af4}, Eq. 2.82 becomes:

$$-(\frac{1}{E_M} - \frac{1}{E_A})\frac{\sigma_{af4}^2}{2} + C(T_4) - \sigma_{af4}\epsilon_0 - a + (\frac{\beta}{2})\epsilon_0^2 = 0 \tag{3.7}$$

Adding Eqs. 3.4 and 3.7 gives material parameter a:

$$a = \frac{1}{2}[(\frac{1}{E_M} - \frac{1}{E_A})\frac{\sigma_{ms1}^2 - \sigma_{af4}^2}{2} + (\sigma_{ms1} - \sigma_{af4})\epsilon_0 - C(T_1) + C(T_4)] \tag{3.8}$$

$C(T_1)$ and $C(T_4)$ are values of $C(T)$ at the temperatures of T_1 and T_4. In general form for given T_i (i = 0, 1, 2, 3, 4), $C(T_i)$ can be written as

$$C(T_i) = \frac{1}{2}[(\frac{1}{E_M} - \frac{1}{E_A})\frac{\sigma^2_{ms(i)} + \sigma^2_{af(i)}}{2} + (\sigma_{ms(i)} + \sigma_{af(i)})\epsilon_0 - \beta\epsilon_0^2] \tag{3.9}$$

To calculate a, $C(T)$ values at martensite start and austenite finish temperatures are needed. Using 3.9, $C(T_1)$ and $C(T_4)$ are found as:

$$C(T_1) = \frac{1}{2}[(\frac{1}{E_M} - \frac{1}{E_A})\frac{\sigma^2_{ms1} + \sigma^2_{af1}}{2} + (\sigma_{ms1} + \sigma_{af1})\epsilon_0 - \beta\epsilon_0^2] \tag{3.10}$$

$$C(T_4) = \frac{1}{2}[(\frac{1}{E_M} - \frac{1}{E_A})\frac{\sigma^2_{ms4} + \sigma^2_{af4}}{2} + (\sigma_{ms4} + \sigma_{af4})\epsilon_0 - \beta\epsilon_0^2] \tag{3.11}$$

Using values of Eqs. 3.10 and 3.11, a in Eq. 3.8 becomes:

$$a = \frac{1}{2}[(\frac{1}{E_M} - \frac{1}{E_A})\frac{\sigma^2_{ms1} - \sigma^2_{af1} + \sigma^2_{ms4} - \sigma^2_{af4}}{4} + \frac{(\sigma_{ms1} + \sigma_{ms4} - \sigma_{af1} - \sigma_{af4})}{2}\epsilon_0] \tag{3.12}$$

With the addition of thermomechanical coupling, temperature of the material and may change and transformation stresses also change. Therefore material parameter a, can not be calculated assuming isothermal conditions and a recalculation is needed as shown.

Similarly adding Eqs. 3.5 and 3.6 one gets b:

$$b = \frac{1}{2}[(\frac{1}{E_M} - \frac{1}{E_A})\frac{\sigma^2_{mf2} - \sigma^2_{as3}}{2} + (\sigma_{mf2} - \sigma_{as3})\epsilon_0 - C(T_2) + C(T_3)] \tag{3.13}$$

Again using 3.9, $C(T_2)$ and $C(T_3)$ can be written as:

$$C(T_2) = \frac{1}{2}[(\frac{1}{E_M} - \frac{1}{E_A})\frac{\sigma_{ms2}^2 + \sigma_{af2}^2}{2} + (\sigma_{ms2} + \sigma_{af2})\epsilon_0 - \beta\epsilon_0^2] \tag{3.14}$$

$$C(T_3) = \frac{1}{2}[(\frac{1}{E_M} - \frac{1}{E_A})\frac{\sigma_{ms3}^2 + \sigma_{af3}^2}{2} + (\sigma_{ms3} + \sigma_{af3})\epsilon_0 - \beta\epsilon_0^2] \tag{3.15}$$

Using Eqs. 3.14 and 3.15, b in Eq. 3.13 becomes:

$$\begin{aligned} b = \frac{1}{2}[(\frac{1}{E_M} - \frac{1}{E_A})\frac{2\sigma_{mf2}^2 - 2\sigma_{as3}^2 - \sigma_{ms2}^2 - \sigma_{af2}^2 + \sigma_{ms3}^2 + \sigma_{af3}^2}{4} \\ + \frac{(2\sigma_{mf2} - 2\sigma_{as3} - \sigma_{ms2} - \sigma_{af2} + \sigma_{ms3} + \sigma_{af3})}{2}\epsilon_0] \end{aligned} \tag{3.16}$$

Similarly using same equations G is found:

$$\begin{aligned} G = (\frac{1}{E_M} - \frac{1}{E_A})\frac{2\sigma_{mf2}^2 - \sigma_{af4}^2 - \sigma_{ms1}^2 + 2\sigma_{as3}^2 + \sigma_{af1}^2 + \sigma_{ms4}^2 - \sigma_{ms2}^2 - \sigma_{ms3}^2 - \sigma_{af2}^2 - \sigma_{af3}^2}{8} \\ + \frac{(2\sigma_{mf2} - \sigma_{af4} - \sigma_{ms1} + 2\sigma_{as3} + \sigma_{af1} + \sigma_{ms4} - \sigma_{ms2} - \sigma_{ms3} - \sigma_{af2} - \sigma_{af3})\epsilon_0}{4} \\ - (\alpha - \beta)\epsilon_0^2 \end{aligned} \tag{3.17}$$

3.3. Modification of Material Parameters a and G Based on Strain Rate

Although thermomechanical coupling is included in ZM model, its performance at higher strain rates, where strong thermomechanical coupling is dominant, is not accurate. To investigate mechanical behavior under high strain rates, experimental work of Shaw and Kyriakides [38], is used. In their work they tested stress-strain behavior of cylinder NiTi bar at different strain rates. In Fig. 3.3, comparison of experimental [38], and simulation results with original coupled ZM-model, at high and low strain rates can be seen.

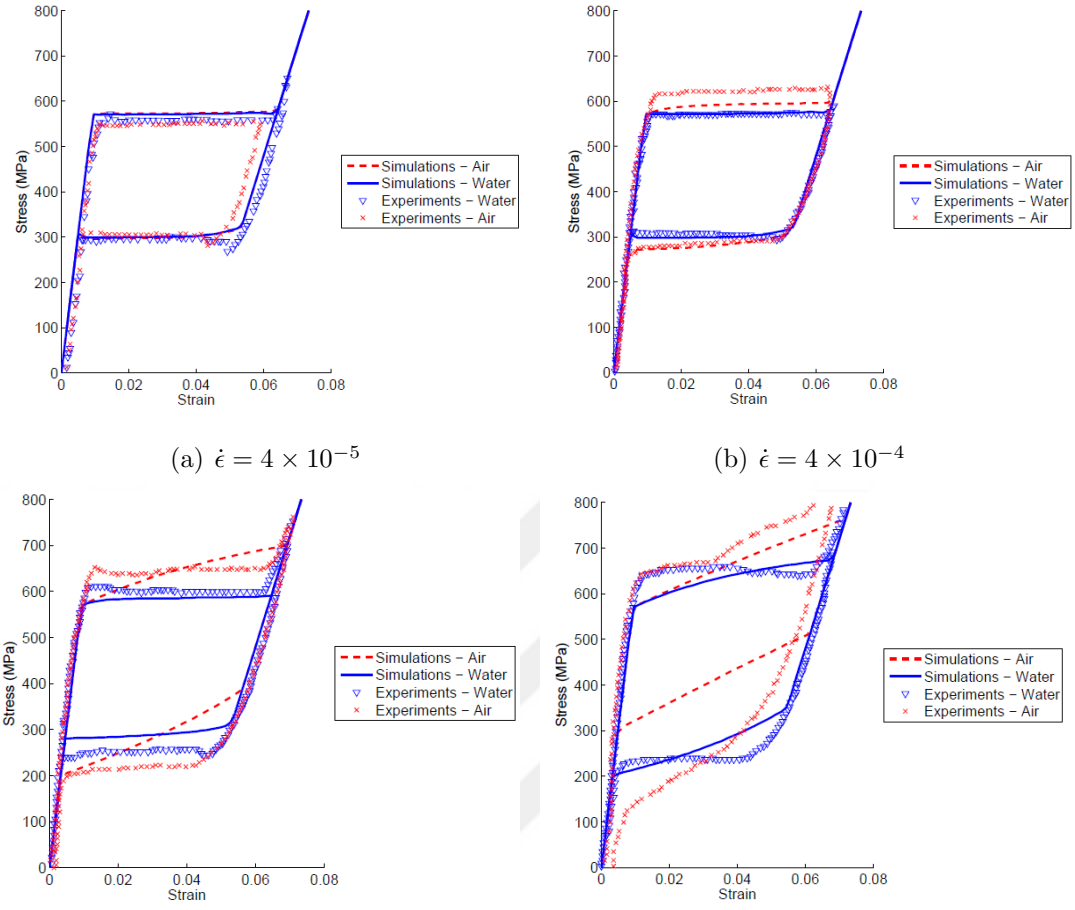

(a) $\dot{\epsilon} = 4 \times 10^{-5}$ (b) $\dot{\epsilon} = 4 \times 10^{-4}$

(c) $\dot{\epsilon} = 4 \times 10^{-3}$ (d) $\dot{\epsilon} = 4 \times 10^{-2}$

Figure 3.2. Experimental vs Numerical Stress-Strain Curves for Various Strain Rates [7].

At lower strain rates, where loading occurs isothermally ZM model gives reasonably accurate results as it can be seen on Fig. 3.2a. At high strain rate as in Fig. 3.2d, stress-strain behavior is captured coarsely, transformation start,finish stresses and transformation plateau could not be determined correctly. Also, the hysteresis area is different from that of the experimental one. The simulation results of original coupled ZM model with various strain rates can be seen in Fig. 3.3:

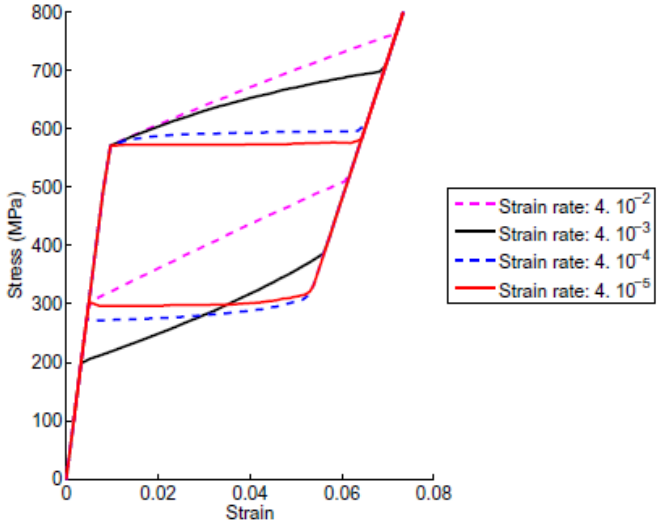

Figure 3.3. Evolution of the Mechanical Response to a Pseudoelastic Loading at Different Strain Rates [7].

Looking at Fig. 3.3 one can notice that, slope of the transformation plateau and martensite finish stress increases with increasing strain rate. Since material temperature increases gradually during forward transformation, stress required to induce martensitic transformation increases. Higher strain rate means higher material temperature and more stable austenite, which means higher stress is needed to maintain transformation.

Apart from increasing slopes at transformation plateau, it is eye-catching that martensite start stress, σ_{ms}, does not change in any condition. Fixity of σ_{ms} does not cause any troubles at lower strain rates where material temperature does not change as it can be seen in Fig. 3.2a, nonetheless, σ_{ms} changes significantly at higher strain rates which can be seen in experimental works of Tobushi *et al.* [8] and Mutlu [9].

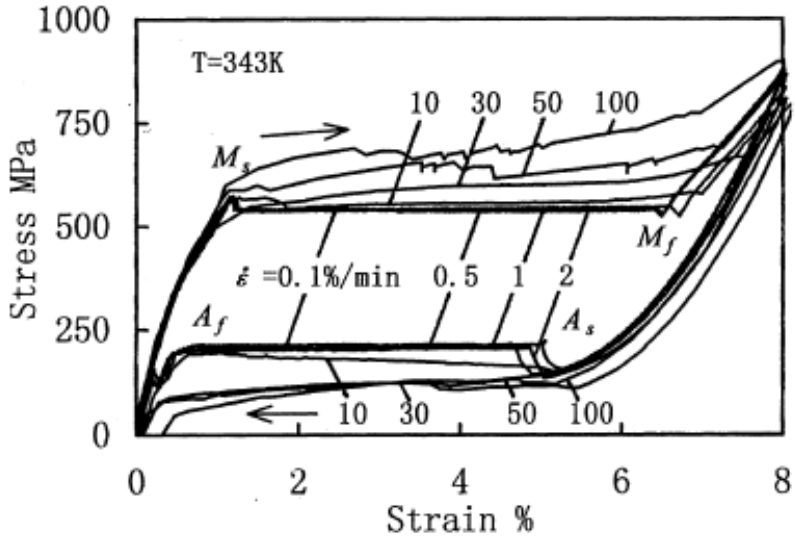

Figure 3.4. Experimental Data of Tobushi *et al.* [8] with Various Strain Rates.

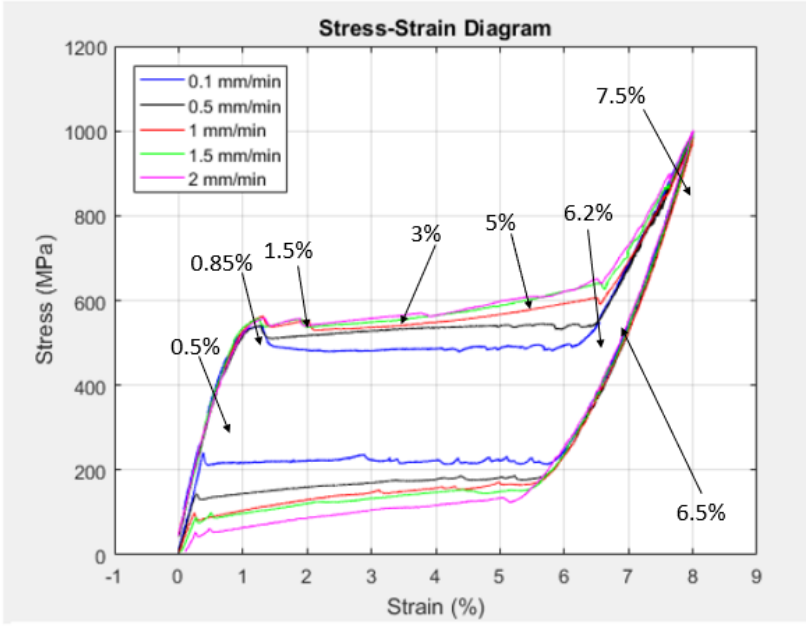

Figure 3.5. Experimental Data of Mutlu with Various Strain Rates [9].

Therefore, simulation results in Fig. 3.3 is not accurate since martensite start stress is always constant. In simulation, prior to transformation, temperature of the material does not change so transformation starts always at the same stress level regardless of the strain rate. However, according to experimental results [8, 9, 38], σ_{ms} increases with increasing strain rate. Martensite start stress, σ_{ms}, takes place in Eqs. 2.96 and 2.98, by changing σ_{ms} in these functions, model will be able to capture martensite start stress. Note that thermomechanical coupling in the model handles the changes of martensite finish, austenite start and austenite finish stresses to some extend not martensite start stress. Since σ_{ms} is related to strain rate, following form of modification is proposed:

$$\sigma'_{ms} = \sigma_{ms}(1 + f(\dot{\epsilon})) \tag{3.18}$$

σ'_{ms} is the modified σ_{ms} parameter which is a function of strain rate and will be used in Eqs. 2.96 and 2.98 to determine a and G values. Experimental work of Tobushi *et al.* [8] showed that logarithm of strain rate $log(\dot{\epsilon})$, has linear relationship with σ_{ms} after a point that is when strain rate is high enough to change the temperature of the material.

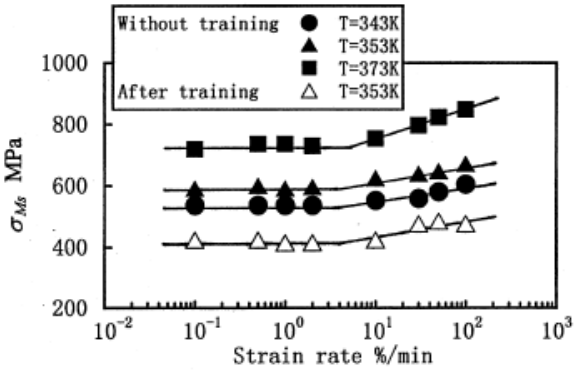

Figure 3.6. σ_{ms} vs Strain Rate (Log Scale) [8].

Similar chart is prepared using experimental data of Mutlu [9]. Martensite start stresses are determined using the procedure proposed by Maletta and Furgiele [54]. According to their method, martensite start stresses are determined by extending and intersecting the linear portion of transformation plateau with the linearly elastic portion at the beginning of loading. In Fig. 3.7, the relationship between martensite start stress and strain rate can be seen based on experimental results of Mutlu [9].

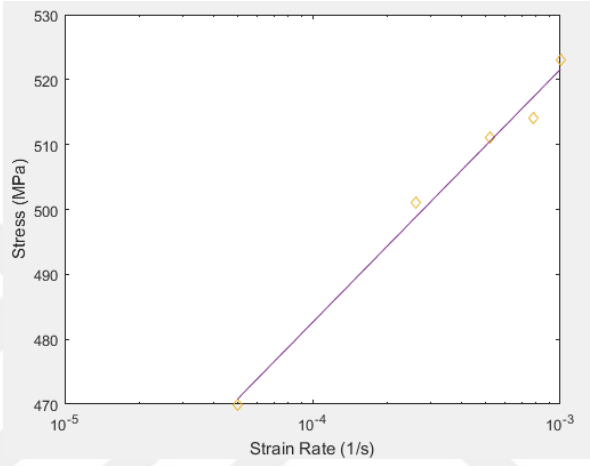

Figure 3.7. σ_{ms} vs Strain Rate (Log Scale).

Linear portion with positive slope, which is observed in Tobushi's work at higher strain rates, is observed in Mutlu's work as well. The horizontal line is not observed, which is the case where strain rate is so slow that transformation occurs quasi-statically. In Mutlu's experiment, only the lowest rate is quasi-static, that is why a horizontal line is not present in Fig. 3.7.

It is observed that, if the loading is not quasi-static, σ_{ms} has a linear relation with $log(\dot{\epsilon})$. So $f(\dot{\epsilon})$ in Eq. 3.18 is assumed to have the following form and σ'_{ms} is written as:

$$f(\dot{\epsilon}) = n \times log(\dot{\epsilon} \times m) \tag{3.19}$$

$$\sigma'_{ms} = \sigma_{ms}(1 + n \times log(\dot{\epsilon} \times m)) \tag{3.20}$$

m and n are the coefficients depend on geometry and heat transfer rate of the material.

3.3.1. Determination of Parameters m and n

Determination of m and n requires one quasi-static and two non-quasi-static tensile tests conducted at different strain rates. To determine m, minimum strain rate which causes a temperature change is needed. Minimum strain rate can be obtained either experimentally with a number of trials conducted at different strain rates, or can be estimated using σ_{ms} vs $\dot{\epsilon}$ graph. Intersection of horizontal line and positively sloped line gives the minimum strain rate which causes a temperature change(See Fig. 3.6).

If the strain rate is low enough to keep material temperature unchanged (horizontal region)then, martensite start stress does not change, thus:

$$\sigma'_{ms} = \sigma_{ms}(1 + n \times log(\dot{\epsilon} \times m)), \tag{3.21}$$

$$log(\dot{\epsilon} \times m) = 0, \tag{3.22}$$

$$\dot{\epsilon} \times m = 1 \tag{3.23}$$

According to experimental data of Shaw and Kyriakides [38], 8×10^{-5} Hz strain rate is the minimum strain rate where loading is non quasi-static. So m is found to be:

$$m = 1/(8 \times 10^{-5}) = 12500 \tag{3.24}$$

To determine n, another σ^*_{ms} in an non-isothermal experiment, conducted at higher strain rate is used. For the strain rate $\dot{\epsilon} = 4 \times 10^{-3}$, martensite start stress is $\sigma^*_{ms} = 630$. Using Eq. 3.20 n is found.

$$\sigma^*_{ms} = \sigma_{ms}(1 + \log(\dot{\epsilon} \times 12500) \times n) \tag{3.25}$$

$$630 = 570(1 + \log(4 \times 10^{-3} \times 12500) \times n) \tag{3.26}$$

$$\frac{630}{570} = (1 + 1.7n) \tag{3.27}$$

$$n = 0.062 \tag{3.28}$$

Due to scarcity of non quasi-static strain rates (only 3 of them are available) precise calculation of n is not possible. If there were more experimental data n could have been determined as a function of strain rate or another parameter. However, in this work it is taken constant for this particular geometry as 0.062. Also note that experimental data used, dates back to 1995, where accuracy of the experimental data are questionable.

Determining m and n, now a can be recalculated as a function of strain rate using modified σ_{ms}. For $\dot{\epsilon} = 4 \times 10^{-2}$, using Eq. 3.20:

$$\sigma'_{ms} = 570(1 + n \times log(\dot{\epsilon} \times m)) \tag{3.29}$$

$$\sigma'_{ms} = 570(1 + 0.062 \times log(4 \times 10^{-2} \times 12500)) \tag{3.30}$$

$$\sigma'_{ms} = 665.3 \tag{3.31}$$

Now, using modified martensite start stress σ'_{ms}, a and G in Eqs. 2.96 and 2.98 are recalculated:

$$a = \frac{1}{2}[(\frac{1}{E_M} - \frac{1}{E_A})\frac{\sigma'^2_{ms} - \sigma^2_{af}}{2} + (\sigma'_{ms} - \sigma_{af})\epsilon_0] \tag{3.32}$$

$$G = \frac{1}{2}[(\frac{1}{E_M} - \frac{1}{E_A})\frac{\sigma^2_{mf} - \sigma'^2_{ms} + \sigma^2_{as} - \sigma^2_{af}}{2} + (\sigma_{mf} - \sigma'_{ms} + \sigma_{as} - \sigma_{af})\epsilon_0 - 2(\alpha - \beta)\epsilon_0^2] \tag{3.33}$$

In Fig. 3.8, estimation of martensite start stress with respect to strain rate with the proposed method can be seen.

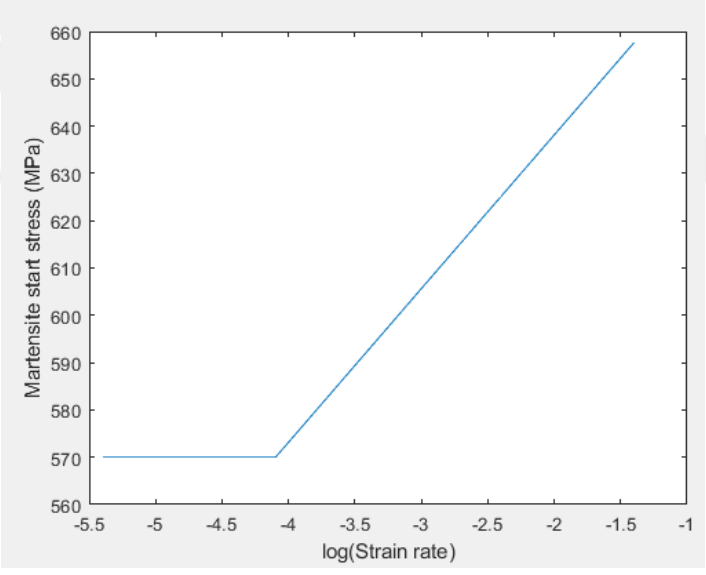

Figure 3.8. Martensite Start Stress vs Logarithm of Strain Rate.

Newly introduced parameter m is associated with the constant horizontal stress line at lefthand side, while n is the slope of the curve at the righthand side.

Same method can be used to estimate modified austenite finish stress, σ_{af} as Tobushi *et al.* [8], demonstrates similar relationship with the logarithmic strain rate and stress:

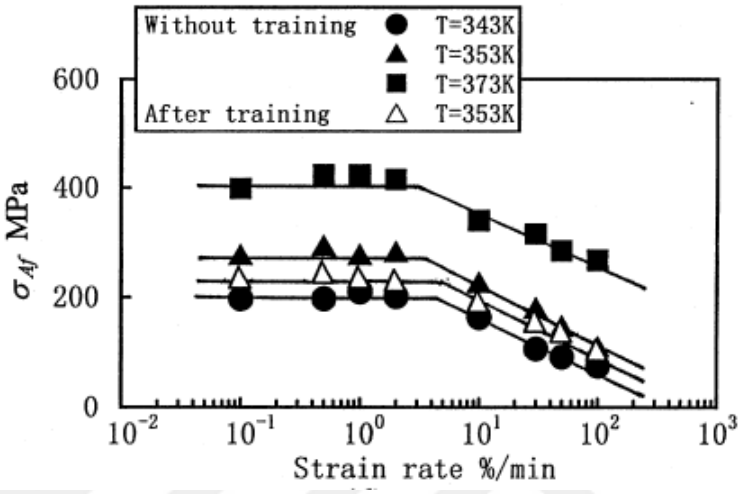

Figure 3.9. σ_{af} vs Strain Rate (Log Scale) [8].

Based on relationship between σ_{af} and strain rate, following form is proposed to estimate modified austenite finish stress σ'_{af}.

$$\sigma'_{af} = \sigma_{af}(1 - f(\dot{\epsilon})) \tag{3.34}$$

It is observed that, if the loading is not quasi-static, σ_{af} has a linear relation with $log(\dot{\epsilon})$. So $f(\dot{\epsilon})$ in Eq. 3.18 is assumed to have the following form and σ'_{af} is written as:

$$f(\dot{\epsilon}) = c \times log(\dot{\epsilon} \times d) \tag{3.35}$$

$$\sigma'_{af} = \sigma_{af}(1 - c \times log(\dot{\epsilon} \times d)) \tag{3.36}$$

If the strain rate is low enough to keep material temperature unchanged (horizontal region in the backward transformation) then, austenite finish stress does not change, thus:

$$\sigma'_{af} = \sigma_{af}(1 - c \times log(\dot{\epsilon} \times d)), \tag{3.37}$$

$$log(\dot{\epsilon} \times d) = 0, \tag{3.38}$$

$$\dot{\epsilon} \times d = 1 \tag{3.39}$$

According to experimental data of Shaw and Kyriakides [38], 2×10^{-4} Hz strain rate is the minimum strain rate where σ_{af} is unchanged. So d is found to be:

$$d = 1/(2 \times 10^{-4}) = 5000 \tag{3.40}$$

To determine c, another σ^*_{af} in an non-isothermal experiment, conducted at higher strain rate is used. For the strain rate $\dot{\epsilon} = 4 \times 10^{-3}$, austenite finish stress is $\sigma^*_{af} = 200$. Using Eq. 3.36 c is found.

$$\sigma^*_{af} = \sigma_{af}(1 - c \times \log(\dot{\epsilon} \times 5000)) \tag{3.41}$$

$$200 = 300(1 - c \times \log(4 \times 10^{-3} \times 5000)) \tag{3.42}$$

$$\frac{200}{300} = (1 - 1.3c) \tag{3.43}$$

$$c = 0.26 \tag{3.44}$$

Due to scarcity of non quasi-static strain rates (only 3 of them are available) precise calculation of c is not possible. If there were more experimental data c could have been determined as a function of strain rate or another parameter. However, in this work it is taken constant for this particular geometry as 0.26. Determining c and d, now a can be recalculated together with previously obtained material parameters m and n as a function of strain rate using modified σ_{ms} and σ_{af}. For $\dot{\epsilon} = 4 \times 10^{-2}$: Using

Eq. 3.20:

$$\sigma'_{ms} = 570(1 + n \times log(\dot{\epsilon} \times m)) \tag{3.45}$$

$$\sigma'_{ms} = 570(1 + 0.062 \times log(4 \times 10^{-2} \times 12500)) \tag{3.46}$$

$$\sigma'_{ms} = 665.3 \tag{3.47}$$

$$\sigma'_{af} = 300(1 - c \times log(\dot{\epsilon} \times d)) \tag{3.48}$$

$$\sigma'_{af} = 300(1 - 0.26 \times log(4 \times 10^{-2} \times 5000)) \tag{3.49}$$

$$\sigma'_{af} = 120.5 \tag{3.50}$$

Now, using modified martensite start stress σ'_{ms}, and modified austenite finish stress σ'_{af}, a and G in Eqs. 2.96 and 2.98 are recalculated:

$$a = \frac{1}{2}[(\frac{1}{E_M} - \frac{1}{E_A})\frac{\sigma'^2_{ms} - \sigma'^2_{af}}{2} + (\sigma'_{ms} - \sigma'_{af})\epsilon_0] \tag{3.51}$$

$$G = \frac{1}{2}[(\frac{1}{E_M} - \frac{1}{E_A})\frac{\sigma^2_{mf} - \sigma'^2_{ms} + \sigma^2_{as} - \sigma'^2_{af}}{2} + (\sigma_{mf} - \sigma'_{ms} + \sigma_{as} - \sigma'_{af})\epsilon_0 - 2(\alpha - \beta)\epsilon_0^2] \tag{3.52}$$

In Fig. 3.10, estimation of austenite finish stress with respect to strain rate with the proposed method can be seen.

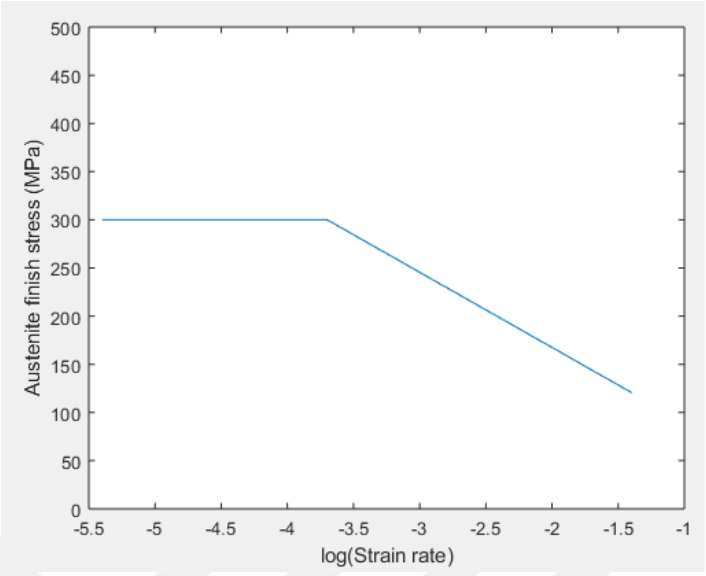

Figure 3.10. Austenite Finish Stress vs Logarithm of Strain Rate.

Newly introduced parameter d is associated with the constant horizontal stress line at lefthand side, while c is the negative slope of the curve at the righthand side.

3.4. Algorithmic Setup and Implementation of m and n to UMAT

This section addresses the algorithmic setup of thermo-mechanically coupled problem and implementation of proposed solution to the user subroutine.

3.4.1. Boundary Value Problem

The problem to be solved is the thermomechanical response of shape memory alloy structure, occupying volume Ω subjected to a loading in the time interval $[0, T]$. SMA structure is subjected to body forces f over Ω and contact forces T_d on $\partial\Omega_T$ and displacement is appointed over the remaining boundary $\partial\Omega_u$. Thermal boundary conditions are determined using Fourier's law of conduction Heat generation Q is acting over Ω and heat convection between structure and surroundings is over $\partial\Omega$. The

problem can be solved using following sets of equations: Static and kinetic admissibility,

$$div\boldsymbol{\sigma} = f \text{ over } \Omega \tag{3.53}$$

$$u = u_d \text{ on } \partial\Omega_u \tag{3.54}$$

$$\boldsymbol{\sigma}.\boldsymbol{n} = T_d \text{ on } \partial\Omega_T \tag{3.55}$$

Assuming infinitesimal strain,

$$\boldsymbol{\epsilon} = \frac{1}{2}(\nabla u +^t \nabla u) \text{ over } \Omega \tag{3.56}$$

Constitutive stress-strain relation,

$$\boldsymbol{\sigma} = \boldsymbol{K} : (\boldsymbol{\epsilon} - z\boldsymbol{\epsilon}_{ori} - \boldsymbol{\alpha}(T - T_0)) \tag{3.57}$$

Heat equation:

$$\rho C_p \dot{T} - div(k\nabla T) = T\frac{\partial C(T)}{\partial T}\dot{z} + [a(1-z) + bz]|\dot{z}| \text{ over } \Omega \tag{3.58}$$

$$\boldsymbol{q}.\boldsymbol{n} = h(T - T_{ext}) \text{ on } \partial\Omega \tag{3.59}$$

$$T(t = 0) = T_{ext} \tag{3.60}$$

where h is the convective heat transfer coefficient same for austenite and martensite phases.

3.4.2. Time Discretization

To solve boundary value problem prescribed above, finite element analysis is used. Time discretization of the constitutive equations is performed using the implicit algorithm of Zaki [55], and Gu [43] which solves mechanical (σ, u) and thermal (Q, T) problem simultaneously. Phase transformation and martensite reorientation is computed simultaneously by the mechanical part. $_n$ and $_{n+1}$ are the load increment numbers and $^{(k)}$ is the solution iteration number.

The predictor step, computes the stress state and strain increment elastically without any evolution in internal variables.

$$z_{n+1}^{(0)} = z_n, \quad \boldsymbol{\epsilon}_{ori,n+1}^{(0)} = \boldsymbol{\epsilon}_{ori,n} \tag{3.61}$$

The trial thermoelastic stress is given by:

$$\boldsymbol{\sigma}_{n+1}^{(0)} = \boldsymbol{K}_{n+1}^{(0)} : [\boldsymbol{\epsilon}_{n+1} - z_{n+1}^{(0)}\boldsymbol{\epsilon}_{ori,n+1}^{(0)} - \boldsymbol{\alpha}_{n+1}^{(0)}(T_{n+1} - T_0)] \tag{3.62}$$

if,

$$F_z^1(\boldsymbol{\sigma}_{n+1}^{(k)}, z_{n+1}^{(k)}, \boldsymbol{\epsilon}_{ori,n+1}^{(k)}) \leq 0 \tag{3.63}$$

$$F_{ori}(\boldsymbol{\sigma}_{n+1}^{(k)}, z_{n+1}^{(k)}, \boldsymbol{\epsilon}_{ori,n+1}^{(k)}) \leq 0 \tag{3.64}$$

are both verified, then the trial state is accepted and increment is elastic. If either of the inequalities is not satisfied, evolution of internal variables z and $\boldsymbol{\epsilon}_{ori}$ must be computed. To achieve this, first order Taylor series expansions are used to estimate the transformation functions:

$$F^{1,(k)}_{z,n+1} = F^{1,(k-1)}_{z,n+1} + \partial_{\boldsymbol{\sigma}} F^{1,(k-1)}_{z,n+1} : \Delta\boldsymbol{\sigma}^{(k)}_{n+1} + \partial_z F^{1,(k-1)}_{z,n+1} \Delta z^{(k)}_{n+1} + \partial_{\boldsymbol{\epsilon}_{ori}} F^{1,(k-1)}_{z,n+1} \Delta\boldsymbol{\epsilon}^{(k)}_{ori,n+1} + \partial_T F^{(k-1)}_{z,(n+1)} \Delta T_{n+1} = 0 \tag{3.65}$$

$$F^{1,(k)}_{ori,n+1} = F^{1,(k-1)}_{ori,n+1} + \partial_{\boldsymbol{\sigma}} F^{1,(k-1)}_{ori,n+1} : \Delta\boldsymbol{\sigma}^{(k)}_{n+1} + \partial_z F^{1,(k-1)}_{ori,n+1} \Delta z^{(k)}_{n+1} + \partial_{\boldsymbol{\epsilon}_{ori}} F^{1,(k-1)}_{ori,n+1} \Delta\boldsymbol{\epsilon}^{(k)}_{ori,n+1} = 0 \tag{3.66}$$

Time discrete stress-strain relation:

$$\Delta\boldsymbol{\sigma}^{(k)}_{n+1} = \boldsymbol{K}^{(k-1)}_{n+1} : [\Delta\boldsymbol{\epsilon}^{(k)}_{n+1} - (\Delta\boldsymbol{K}^{(k),-1}_{n+1} : \boldsymbol{\sigma}^{(k-1)}_{n+1} + \Delta z^{k}_{n+1}\boldsymbol{\epsilon}^{(k-1)}_{ori,n+1} + z^{k-1}_{n+1}\boldsymbol{\epsilon}^{(k)}_{ori,n+1} + \Delta\boldsymbol{\alpha}^{(k)}_{n+1}(T^{(k-1)}_{n+1} - T_0) + \Delta T^{(k)}_{n+1}\boldsymbol{\alpha}^{(k-1)}_{n+1})] \tag{3.67}$$

where,

$$\Delta\boldsymbol{K}^{(k),-1}_{n+1} = (\boldsymbol{K}^{-1}_{M} - \boldsymbol{K}^{-1}_{A})\Delta z^{(k)}_{n+1}, \tag{3.68}$$

$$\Delta\boldsymbol{\alpha}^{(k)}_{n+1} = (\boldsymbol{\alpha}_M - \boldsymbol{\alpha}_A)\Delta z^{(k)}_{n+1}. \tag{3.69}$$

Time discrete consistency condition is given as:

$$\Delta\boldsymbol{\epsilon}^{(k)}_{ori,n+1} = \Delta\eta^{(k)}_{n+1}\boldsymbol{N}^{(k-1)}_{n+1}, \tag{3.70}$$

where $\Delta\eta^{(k)}_{n+1}$ is the discrete inelastic multiplier, and $\boldsymbol{N}^{(k-1)}_{n+1} = \frac{3}{2}\frac{\boldsymbol{X}^{(k-1)}_{n+1}}{X^{(k-1)}_{VM,n+1}}$. Combining Eqs. 3.67 to 3.70 gives the following incremental stress:

$$\Delta\boldsymbol{\sigma}^{(k)}_{n+1} = -\boldsymbol{K}^{(k-1)}_{n+1} : [\boldsymbol{R}^{(k-1)}_{n+1}\Delta z^{(k)}_{n+1} + z^{(k-1)}_{n+1}\boldsymbol{N}^{(k-1)}_{n+1}\Delta\eta^{(k)}_{n+1}] \tag{3.71}$$

where,

$$\boldsymbol{R}_{n+1}^{(k-1)} = (\boldsymbol{K}_M^- 1 - \boldsymbol{K}_A^- 1) : \boldsymbol{\sigma}_{n+1}^{(k-1)} + \boldsymbol{\epsilon}_{ori,n+1}^{(k-1)} + (\boldsymbol{\alpha}_M - \boldsymbol{\alpha}_A)(T_{n+1}^{(k-1)} - T_0) \tag{3.72}$$

Computation of incremental martensite volume fraction $\Delta z_{n+1}^{(k)}$ and incremental inelastic multiplier $\Delta\eta_{n+1}^{(k)}$ allows determination of internal variable in a given state which are given by:

$$\Delta z_{n+1}^{(k)} = -\frac{F_{z,n+1}^{1,(k-1)}}{A_z} - \frac{A_{ori}}{A_z}\left(\frac{B_z F_{z,n+1}^{1,(k-1)} - A_z F_{ori,n+1}^{(k-1)}}{A_z B_{ori} - B_z A_{ori}}\right) \tag{3.73}$$

$$\Delta\eta_{n+1}^{(k)} = \frac{B_z F_{z,n+1}^{1,(k-1)} - A_z F_{ori,n+1}^{(k-1)}}{A_z B_{ori} - B_z A_{ori}} \tag{3.74}$$

with,

$$A_z = \partial_z F_{z,n+1}^{(k-1)} - \partial_{\boldsymbol{\sigma}} F_{z,n+1}^{(k-1)} : \boldsymbol{K}_{n+1}^{(k-1)} : \boldsymbol{R}_{n+1}^{(k-1}, \tag{3.75}$$

$$A_{ori} = \partial_{\boldsymbol{\epsilon}_{ori}} F_{z,n+1}^{(k-1)} : \boldsymbol{N}_{n+1}^{(k-1)} - z_{n+1}^{(k-1)} \partial_{\boldsymbol{\sigma}} F_{z,n+1}^{(k-1)} : \boldsymbol{K}_{n+1}^{(k-1)} : \boldsymbol{N}_{n+1}^{(k)}, \tag{3.76}$$

$$B_z = \partial_z F_{ori,n+1}^{k-1} - \partial_{\boldsymbol{\sigma}} F_{ori,n+1}^{(k-1)} : \boldsymbol{K}_{n+1}^{(k-1)} : \boldsymbol{R}_{n+1}^{(k-1)}, \tag{3.77}$$

$$B_{ori} = \partial_{\boldsymbol{\epsilon}_{ori}} F_{ori,n+1}^{(k-1)} : \boldsymbol{N}_{n+1}^{(k-1)} - z_{n+1}^{(k-1)} \partial_{\boldsymbol{\sigma}} F_{ori,n+1}^{(k-1)} : \boldsymbol{K}_{n+1}^{(k-1)} : \boldsymbol{N}_{n+1}^{(k)} \tag{3.78}$$

If phase transformation occurs without martensite reorientation, Δz at iteration (k) simplifies to:

$$\Delta z^{(k)} = -\frac{F_z^{(k-1)}}{A_z^{(k-1)}}. \tag{3.79}$$

In the case where martensite reorientation is present without phase transformation, inelastic multiplier at iteration (k) can be written as:

$$\Delta\eta^{(k)} = -\frac{F_{ori}^{(k-1)}}{B_{ori}^{(k-1)}}. \tag{3.80}$$

3.4.3. Algorithmic Setup

To solve thermomechanically coupled problem user material subroutine is coded in Fortran to be used in finite elements software ABAQUS. Explanation of the tangent operators used in algorithm can be seen in Appendix. As a modification, parameter σ_{ms} is updated at each increment using local strain rate $\dot{\epsilon}$, and using Eq. 3.20 a and G are also updated at initialization section. Newly added material parameters m and n are defined at material properties section of ABAQUS. Local strain rate is obtained with DSTRAN/DTIME in each node; a' and G' are recalculated for each specific node using strain rate obtained from algorithm. Algorithm can be seen for thermomechanically coupled SMA model in Fig. 3.11:

Input: Material parameters, $\boldsymbol{\epsilon}_n, T_n, z_n, \boldsymbol{\epsilon}_{ori,n}$.
Output: $\boldsymbol{\sigma}_{n+1}, z_{n+1}, \boldsymbol{\epsilon}_{ori,n+1}, T_{n+1}$ tangent operators $J_{\boldsymbol{\sigma\epsilon}}, J_{\boldsymbol{\sigma}T}, J_{Q\boldsymbol{\epsilon}}, J_{QT}$.
Initialization Set $k = 0, z_{n+1}^{(0)} = z_n, \boldsymbol{\epsilon}_{ori,n}^{(0)}, \boldsymbol{\epsilon}_{n+1} = \boldsymbol{\epsilon}_n + \Delta\boldsymbol{\epsilon}_n, T_{n+1} = T_n + \Delta T_n$.
Calculate the trial thermoelastic stress using Eq. 3.62
if No active reorientation or transformation **then**
  return
else if Only martensite reorientation is active **then**
  Calculate evolution of inelastic multiplier through $\Delta\eta_{n+1}$ using Eq. 3.80
  Calculate the tangent operators using B.18 to B.21.
else if Only phase transformation is active **then**
  Calculate evolution of martensite volume fraction through Δz_{n+1} using Eq. 3.79
  Calculate the tangent modulus tensors using B.18 to B.21.
else if Both phase transformation and reorientation are active **then**
  Calculate $\Delta\eta_{n+1}$ and Δz_{n+1} using Eqs. 3.74 and 3.73.
  Calculate the tangent operators using B.18 to B.21.
end if
return: stress, state variables, tangent operators

Figure 3.11. Algorithm for Coupled Model.

4. RESULTS

In this chapter, effect of material parameters discussed in Ch. 3 are visually demonstrated using FE analysis results obtained from ABAQUS. Effect of phase change heat density explained in Sec. 3.1.1 with different material parameters at different temperatures using dog-bone specimen with uncoupled model are shown in Sec. 4.1. Using a MATLAB algorithm, yield surfaces of the forward transformation function are drawn at various conditions to better understand and visualize nature of transformation for a material point in Sec. 4.2. Explained in Sec. 3.2, material parameters a, b and G are re-evaluated and FE analysis are conducted using dog-bone specimen which can be seen in Sec. 4.3. Lastly, FE analysis is conducted using ABAQUS with the modified UMAT according to the new method described in Sec. 3.3. The mechanical response comparison between experiments,existing models and the new model is demonstrated in Sec. 4.4.

4.1. Effect of Phase Change Heat Density, $C(T)$, on Mechanical Behavior

The influence of $C(T)$ on stress and strain is simulated using the uncoupled ZM-model. Following material parameters are used for the dog-bone specimen:

Table 4.1. Material Properties.

E_A	62000 MPa	b	16.5156 MPa
E_M	45000 MPa	ϵ_0	0.06
v	0.33	G	15.1503 MPa
Y	110 MPa	β	3666.7 MPa
α	1833.3 MPa	κ	8.2138 MPa
ζ	0.2586 MPa/K	T	300 K
A_f^0	289.15 K	t_a	$1.1e^{-5}$ 1/K
a	14.8138 MPa	t_m	$6.6e^{-6}$ 1/K

At 300 K temperature, using Eq. 2.24 $C(T)$ is found to be 11.02. In FE analysis following values are used for $C(T') = C(T)$ and temperature, T.

Table 4.2. $C(T')$ and Temperature Values.

Simulation #	# 1	# 2	# 3	# 4	# 5
$C(T')$	0	11.02	22.04	44.08	44.08
Temperature (K)	300	300	300	300	427.8

$C(T')$ values are obtained by multiplying $C(T)$ by $0, 1, 2, 4$ and 1 respectively for the cases $\#1, \#2, \#3, \#4, \#5$. 427.8 K is chosen in case '#5' in order to equate $C(T')$ values in #4 and #5. When (T) increases at constant temperature $T = 300K$, transformation stresses and strain increase. Shifting of stress-strain curve can be seen on Fig. 4.1 It is important to note that stress-strain graphs conducted at different temperatures (300 K-427.8 K) becomes exactly the same by equating $C(T')$ values manually. $C(T)$ in general governs the free energy of martensite related to its temperature. Since at higher temperatures martensite is less stable, it wants to transform into austenite. This phenomenon causes an increase in free energy of martensite, denoted in general form in this model by $zC(T)$.

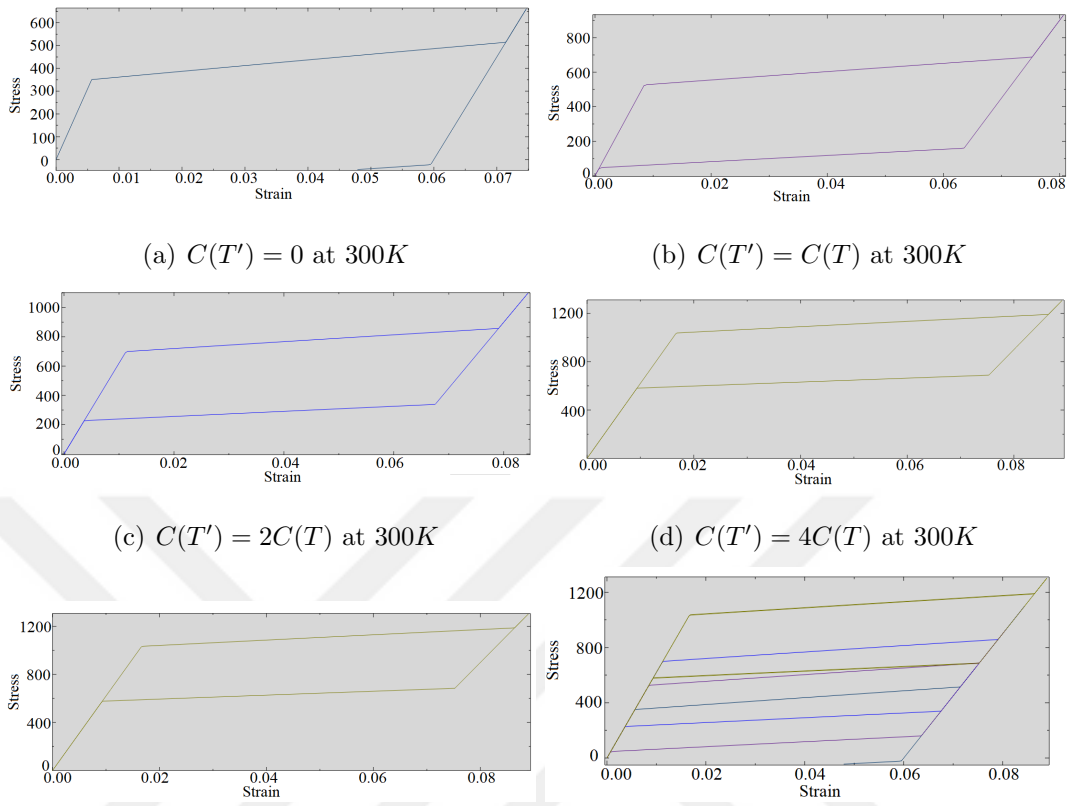

(a) $C(T') = 0$ at $300K$

(b) $C(T') = C(T)$ at $300K$

(c) $C(T') = 2C(T)$ at $300K$

(d) $C(T') = 4C(T)$ at $300K$

(e) $C(T') = C(T)$ at $427.8K$

(f) All Curves Together

Figure 4.1. Stress-Strain Curves.

4.2. On the Forward Transformation Function $\mathcal{F}_z^1$, Using Strain Rate Dependence

Assuming loading is quasistatic, forward transformation function $\mathcal{F}_z^1$ in Eq. 2.81 reduces to:

$$\mathcal{F}_z^1 = [\frac{1}{3}El_{MA}\sigma_{VM}^2 + \frac{1}{2}(\frac{1}{3}El_{MA} + P_{MA})(tr\boldsymbol{\sigma})^2 - C(T)] + \boldsymbol{\sigma} : \boldsymbol{\epsilon}_{ori}$$
$$- (G+b)z - a(1-z) - [(\alpha-\beta)z + \frac{\beta}{2}](\frac{2}{3}\boldsymbol{\epsilon}_{ori} : \boldsymbol{\epsilon}_{ori}), \tag{4.1}$$

where,

$$\epsilon_{ori} = \frac{3}{2}\epsilon_0 \frac{\boldsymbol{s}}{\sigma_{VM}} \tag{4.2}$$

$\boldsymbol{s}$ being deviatoric stress tensor [6]. Using Eq. 4.2, forward transformation function in Eq. 4.1 can be written as function of stress tensor $\boldsymbol{\sigma}$ and martensite volume fraction z only:

$$\begin{aligned}\mathcal{F}_z^1 = [\frac{1}{3}El_{MA}\sigma_{VM}^2 + \frac{1}{2}(\frac{1}{3}El_{MA} + P_{MA})(tr\boldsymbol{\sigma})^2 - C(T)] + \boldsymbol{\sigma} : \frac{3}{2}\epsilon_0 \frac{\boldsymbol{s}}{\sigma_{VM}} \\ - (G+b)z - a(1-z) - [(\alpha-\beta)z + \frac{\beta}{2}](\epsilon_0 \frac{\boldsymbol{s}}{\sigma_{VM}} : \frac{3}{2}\epsilon_0 \frac{\boldsymbol{s}}{\sigma_{VM}})\end{aligned} \tag{4.3}$$

which takes the value of 0 during forward transformation. In other words, $\mathcal{F}_z^1 = 0$ gives the solution for z or $\boldsymbol{\sigma}$ if the either one is known. Based on this judgment, using a matlab algorithm, martensite start stresses can be found. Setting $z = 0$ and $\mathcal{F}_z^1 = 0$ will give the solution of principal stresses using Eq. 4.3 which could be interpreted as martensite start stresses. Similarly, when the transformation ends, $z = 1$ and martensite finish stress σ_{mf} can be found. In Fig. 4.2 yield surfaces can be seen at transformation start $z = 0$ and transformation finish $z = 1$ in 3D with the given coordinates.

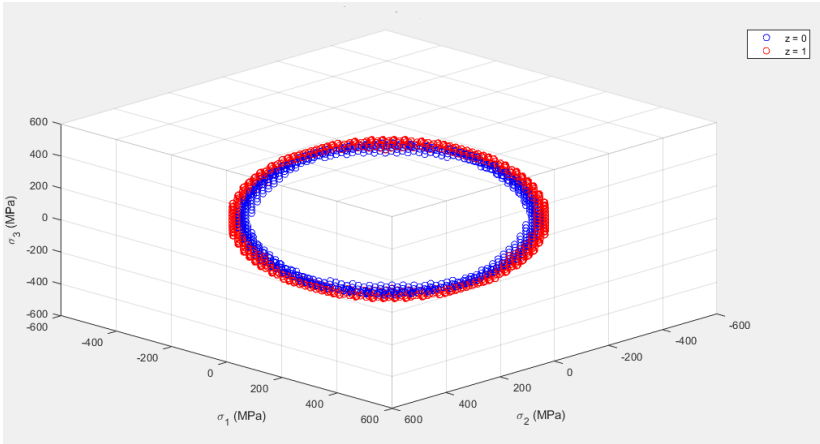

Figure 4.2. Yield Surface of $\mathcal{F}_z^1 = 0$ at $z = 0$ and $z = 1$.

An expansion in the yield surface therefore an increase in the stress at the end of the transformation is observed. Another view of the Fig. 4.2 from three different angles in 3D with the given coordinates can be seen in Fig. 4.3:

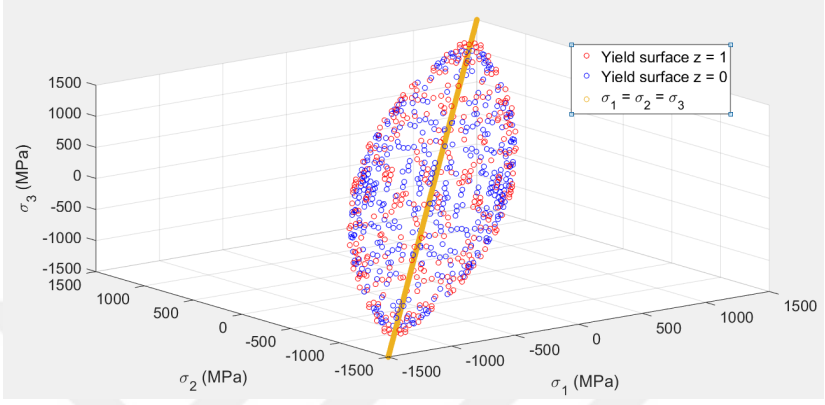

(a) View # 1

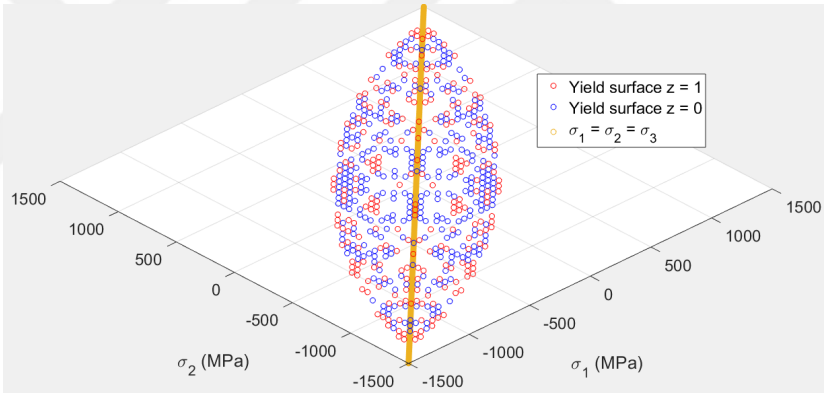

(b) View # 2

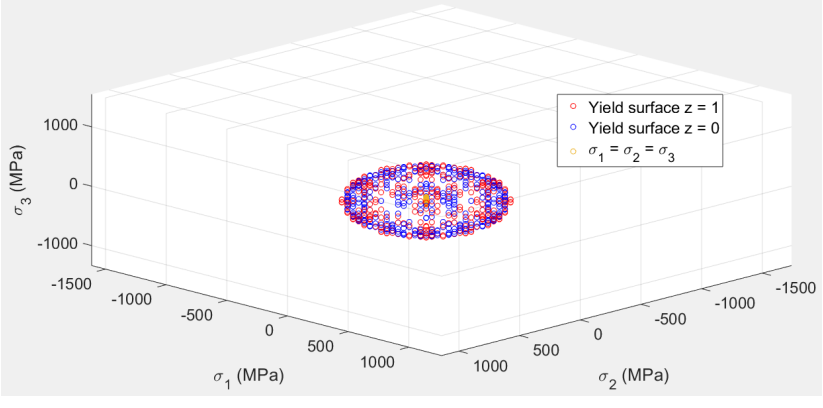

(c) View # 3

Figure 4.3. Yield Surface of $\mathcal{F}_z^1 = 0$ at $z = 0$ and $z = 1$ From Different Angles and Orientations.

One can realize the similarity of the transformation yield surface in Fig. 4.3 to that of 3D von Mises yield surface shown in Fig. 4.4.

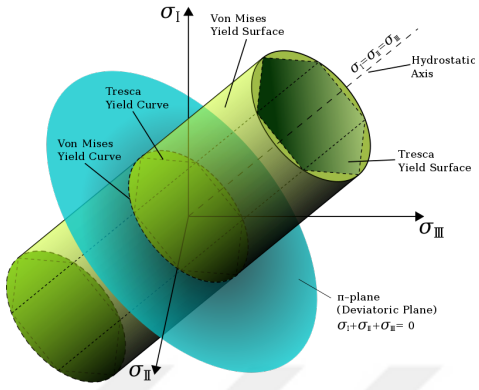

Figure 4.4. von Mises Yield Surface in Principal Coordinates [10].

Although both transformation function yield surfaces and von Mises 3D surface have a centerline at $\sigma_1 = \sigma_2 = \sigma_3$, they have major shape differences. von Mises yield surface in Fig. 4.4 is a infinitely long cylinder whereas Fig. 4.2 shows that transformation function yield surfaces have a finite limit and unlike von Mises yield surface there is a solution at $\sigma_1 = \sigma_2 = \sigma_3$ at some point. In other words, unlike von Mises yield surface, transformation yield surfaces are reached for a certain $\sigma_1 = \sigma_2 = \sigma_3$ according to the proposed transformation function. This also means that, according to transformation function Eq. 4.3, no shear force is needed to yield the material. Calculation and illustration of transformation yield surfaces initiates a method for verification of transformation functions, therefore experimental studies in this particular subject is encouraged. According to ZM model and 4.3, SMAs exhibit hydrostatic pressure effect, that is when hydrostatic stress increases, equivalent stress decreases. In Fig. 4.5 hydrostatic stress versus equivalent stress at $z = 0$ and $z = 1$ yield conditions can be seen.

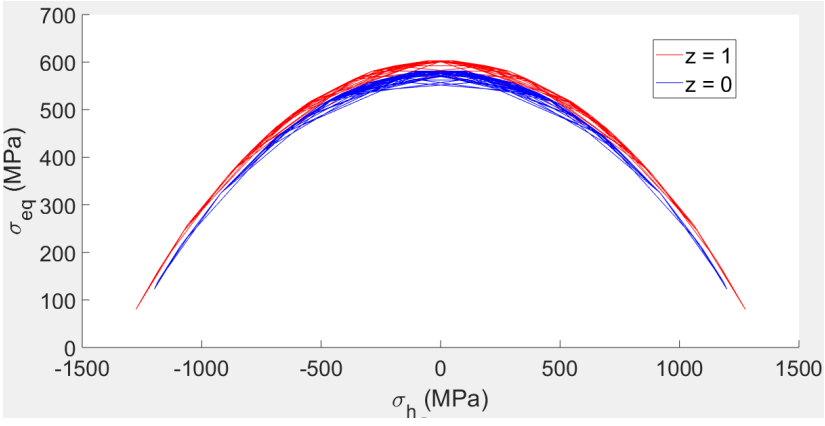

Figure 4.5. σ_{eq} vs σ_h for $z = 0$ and $z = 1$.

According to Fig. 4.5 when absolute value of hydrostatic stress increases material transforms at lower equivalent stresses. For different material temperatures, the yield surface for $\mathcal{F}_z^1 = 0$ can be seen at $z = 0$.

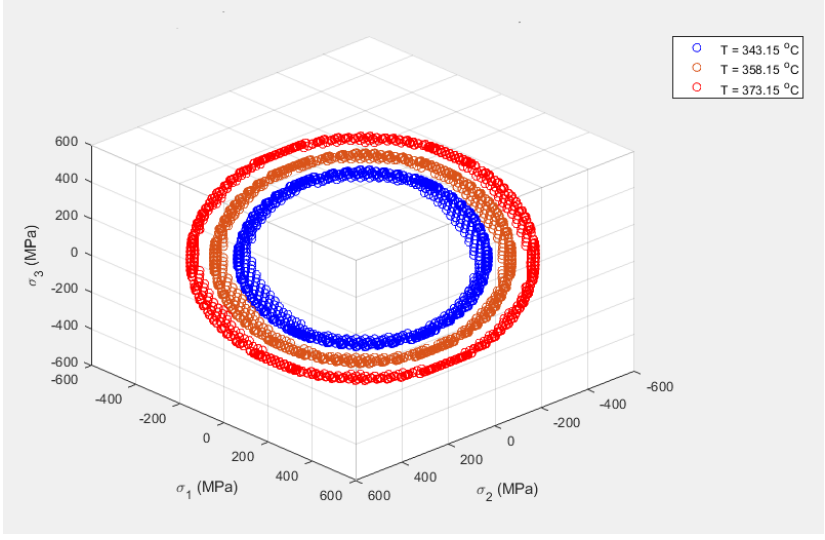

Figure 4.6. Yield Surface of $\mathcal{F}_z^1 = 0$ with Different Temperature at $z = 0$.

Fig. 4.6 figure represents, when the temperature of the material increases, a higher stress is required to initiate transformation. It also reflects austenite becomes more stable at higher temperatures.

In the following figure yield surfaces are drawn using the modified parameter a in Eq. 3.32 at the beginning of transformation. With the addition of new material parameters m and n, martensite start stress is defined as a function of strain rate. As in the experimental works of Tobushi *et al.* [8], Shaw and Kyrikiades [38], and Mutlu [9], it is observed that with increasing strain rate, martensite start stress(thus the forward transformation yield surface) increases.

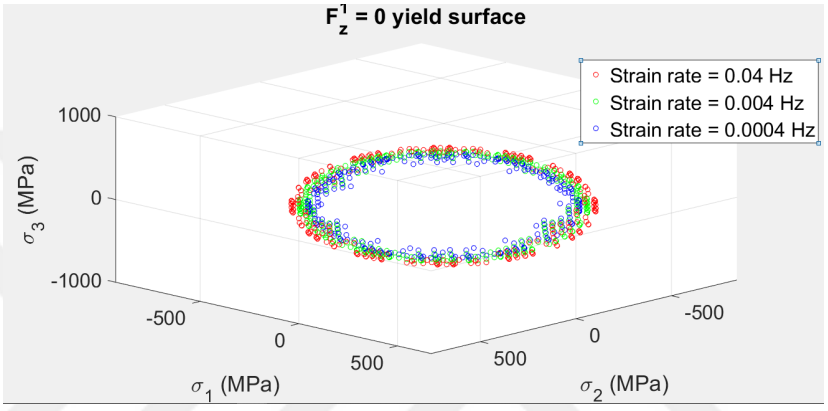

Figure 4.7. Yield surface of $\mathcal{F}_z^1 = 0$ at $z = 0$ with several strain rates using modified model.

Fig. 4.7 indicates that modification of material parameter a successfully expands the yield surfaces of transformation function which returns the stress tensor at forward transformation for a given value of z. Note that following figures are generated with Matlab using uncoupled model for the visualization of transformation function-stress-temperature relations. For more accurate results FEM simulations are conducted using coupled model and modified parameters.

4.3. FE Analysis Using Modified Parameters a, b and G, and Their Effect on Mechanical Behavior

Dogbone specimen in Fig. 4.8 is modeled using ABAQUS and a tensile test (loading-unloading) simulation is conducted using thermomechanically coupled ZM model. Material parameters are identified using experimental data of Mutlu [9] and

can be found in Table 4.3.

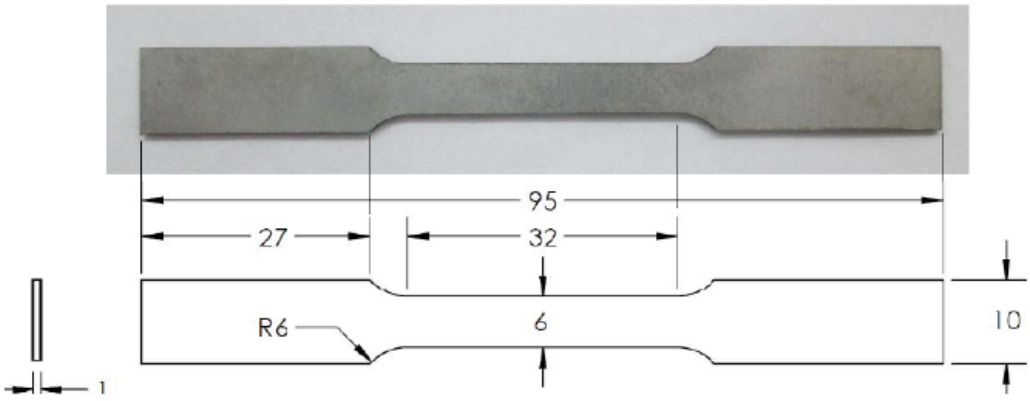

Figure 4.8. Dogbone Specimen Dimensions in mm.

Table 4.3. Material Properties.

E_A	62000 MPa	b	9.5581 MPa
E_M	45000 MPa	ϵ_0	0.05
v	0.33	G	7.9757 MPa
Y	110 MPa	β	4400 MPa
α	2200 MPa	κ	3.9272 MPa
ζ	0.4934 MPa/K	T	303.15 K
A_f^0	289.15 K	t_a	$1.1e^{-5}$ 1/K
a	9.4272 MPa	t_m	$6.6e^{-6}$ 1/K

Using these material properties, after loading and unloading at constant displacement rate, following stress-strain and temperature-strain graphs are obtained.

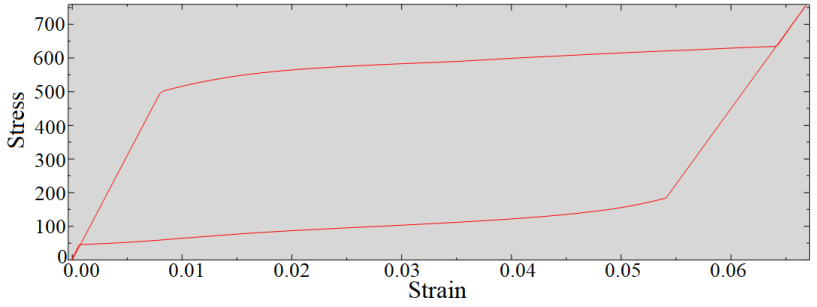

Figure 4.9. Stress(MPa) - Strain(mm/mm) Diagram.

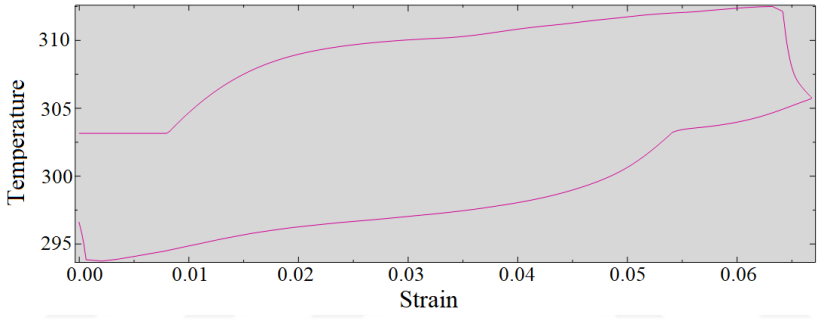

Figure 4.10. Temperature (K) - Strain(mm/mm) Diagram.

From the simulation T_1, T_2, T_3 and T_4 temperatures are obtained as 303.15, 312.5, 303.15 and 293.74 Kelvin. To determine modified versions of a, b and G indicated in Eqs. 3.12, 3.16, 3.17 isothermal stress-strain behavior at T_1, T_2, T_3 and T_4 are needed. Necessary simulations are conducted at these temperatures and corresponding martensite start, martensite finish, austenite start and austenite finish temperatures are determined. Using modified stress values a, b and G are recalculated.

Using recalculated material parameters same simulation is run and stress-strain and temperature-strain graphs with modified material properties are obtained. Their comparison with inital case can be seen in Figures 4.11 and 4.12.

Table 4.4. Material Properties.

Material Parameter	Initial	Modified
a	9.4272	9.3014
b	9.5581	9.7018
G	7.9757	8.1211

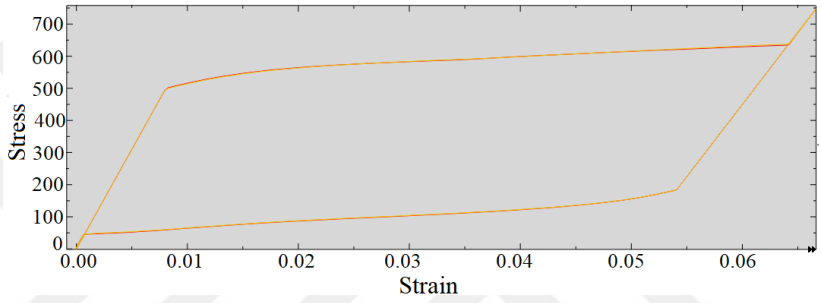

Figure 4.11. Stress- (MPa) - Strain(mm/mm) Diagram with Modified Parameters.

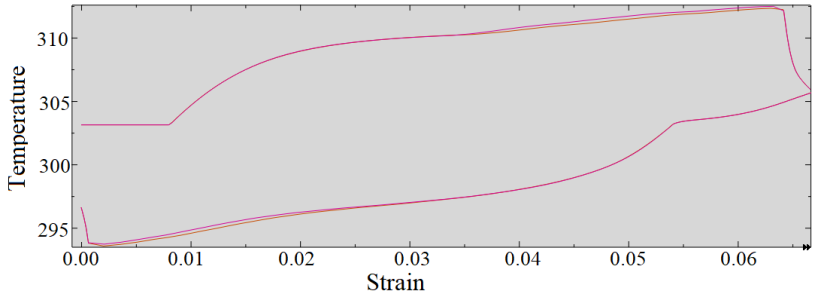

Figure 4.12. Temperature (K)-Strain(mm/mm) Diagram with Modified Parameters(Yellow) and Initial Parameters (Red).

In Fig. 4.11 yellow (modified) and red(initial) curves are almost following the same path. When curves are enlarged, in the beginning of transformation pletau yellow curve is below; while at the end it is above.

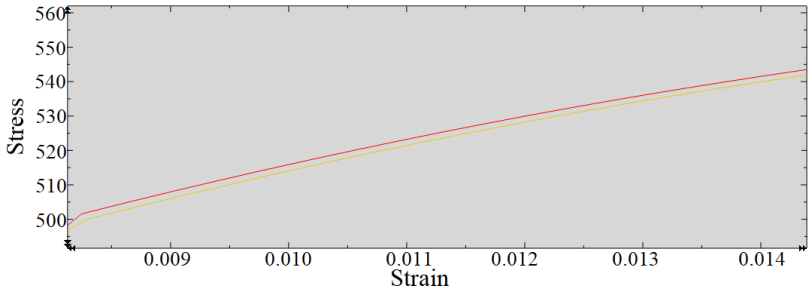

Figure 4.13. Stress (MPa)-Strain(mm/mm) Enlarged Beginning of Transformation.

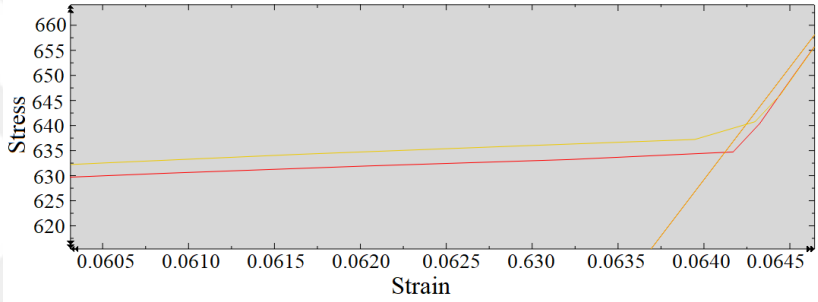

Figure 4.14. Stress (MPa)-Strain(mm/mm) Enlarged End of Transformation.

There is less then 1% change in stress when modified parameters are used. Nevertheless changes of a,b and G are limited, they directly effect transformation functions and dissipation potential. When there are larger temperature changes at transformation start and transformation finish compare to initial temperature, impact of modification might be higher. Model improvement by modification of parameters with method explained above is abandoned, since comparison with original results asserts the change in stress-strain curve, temperature and hysteresis area are not significant.

4.4. FE Analysis Using Modified Material Parameters a and G, and Their Effect on Mechanical Behavior

NiTi wire with 1 mm diameter and 100 mm length is clamped in one end and subjected to tensile displacement on the other end (see Fig. 4.15).

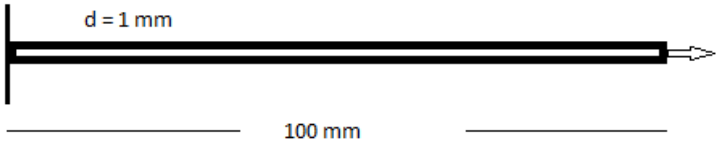

Figure 4.15. Boundary Conditions and Geometry of the NiTi Specimen.

Simulation is conducted using ABAQUS with modified user subroutine. This subroutine computes σ_{ms} and σ_{af} using Eqs. 3.20,3.36 and re-calculates a and G. Strain rate is obtained from the ABAQUS locally at each increment and a and G are updated according to the local strain rate. Following material parameters are used for the simulation:

Table 4.5. Material Properties.

E_A	61500 MPa	b	6.9091 MPa
E_M	24000 MPa	ϵ_0	0.04
v	0.30	G	4.6556 MPa
Y	110 MPa	β	5500 MPa
α	2750 MPa	κ	6.8920 MPa
ζ	0.2914 MPa/K	T	343.15 K
A_f^0	313.15 K	t_a	$1.1e^{-5}$ 1/K
a	6.8920 MPa	t_m	$6.6e^{-6}$ 1/K
h_{air}	50 W $m^{-2}K^{-1}$	k	18 W $m^{-1}K^{-1}$
m	12500 s	n	0.062
d	5000 s	c	0.26

Using original coupled ZM model, modified ZM model, and experimental results, a stress-strain curve comparison graph for the strain rate 4×10^{-2} can be seen in Fig. 4.16.

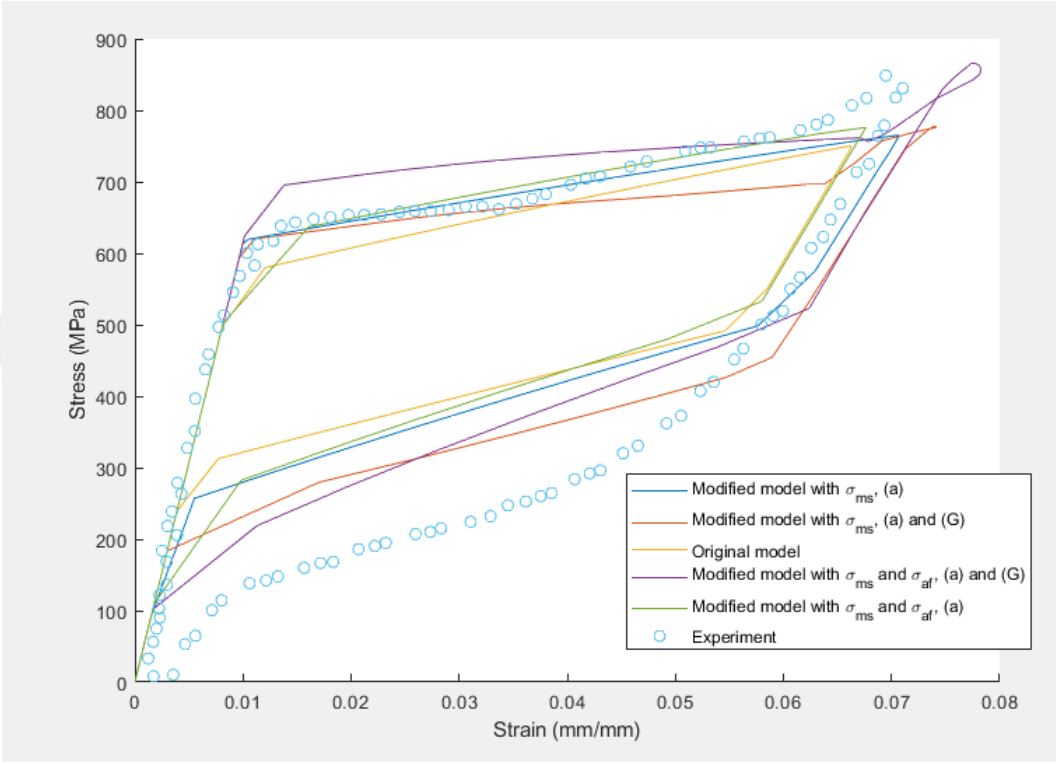

Figure 4.16. Comparison of Simulations and Experimental Data.

Dotted one is experimental data and yellow is the simulation of the original coupled model. Blue is the model with modified a parameter. Orange is the model with modified a and G parameters and yellow is the original model. Purple and green ones are the simulations with modified σ_{ms}, σ_{af}. At higher strain rates original coupled model can not capture the martensite start stress and hysteresis area accurately. Results with modified parameters perform considerably better than original coupled model in terms of capturing stress-strain behavior.

Looking at Fig. 4.16, with modified a parameter, model successfully captures martensite start stress, as well as improvement other transformation stress and strains. However, in model with modified a and G slope of transformation pletau and martensite

finish stress is not as accurate as the original model. Since increased martensite start stress causes a decrease in G parameter, thus a decrease in the slope of transformation plateau, we do not recommend usage of the model with modified G parameter. Models with σ_{af}, σ_{ms} modification cause overshoots to estimation of the stress-strain curve since, since temperature change after the transformation is already taken into account. Since modification of σ_{ms} is related to pre-transformation, we proposed to use the model with σ_{ms} and a modification. Specifically, modified model with σ_{ms} and a modification captures σ_{ms} more accurately and unloading-plateau is closer to the experimental curve and it would be convenient to use this model in fracture analysis. In general, compared to original model, modified models perform better in any case. Based on this work, ZM model can be improved further. The desired mechanical properties whether it is martensite start stress, hysteresis area or martensite finish stress or another one, can be estimated more correctly with the necessary adjustments on related material parameter.

Hysteresis area, which is used to determine dissipation is now estimated more precisely using the model with modified σ_{ms}. So the effect of thermomechanical coupling works in a more correct way. Since the martensite start stress increases with the increasing strain rate, transformation occurs later in a higher stress, causing an expansion of stress-strain curve thus increasing the hysteresis area. In Table 4.6, hysteresis area of experimental and numeric results can be seen.

Table 4.6. Hysteresis Area comparison and errors.

Data	Hysteresis Area (MPa)	Error%
Experimental	32.5536	N/A
Original	12.8907	152.5
Modified a	16.5645	96.5
Modified a and G	18.2484	78.4

Even though, error regarding hysteresis area is still to high, error is reduced by implementing modification. It is obvious that estimation of hysteresis area at high strain rates is not very accurate and there are still room for improvement.

5. EDGE CRACKED NITINOL

5.1. Introduction

In order to optimize the design of SMA product, it is vital to forecast its behavior under different loading and thermal conditions. The fracture behavior of SMAs is a complex phenomenon due to phase transformation, and thermomechanical coupling, yet it is important to estimate mechanical behavior of SMAs on fracture mechanics.

5.2. Fracture Mechanics of Shape Memory Alloys

It is a well known fact that temperature of the SMA plays a very important role in mechanical behavior. In cracked geometries, very high stress levels are attainable in short time due to stress singularity and the temperature of the crack-tip may increase if the loading is applied in short time. Since strong thermo-mechanical coupling is observed in SMAs, temperature increase mechanism in the case of stress induced transformation and its effect on fracture parameters need to be evaluated properly to model material behavior correctly. In this section, works devoted to fracture mechanics and temperature change due to phase phase transformation SMAs are briefly summarized.

Mckeeing and Evans in 1982 [56], worked on stress induced martensitic transformation of brittle materials. They founded that martensitic transformation enhances toughness at the crack tip due to residual strain which limits the crack opening.

Stam and van der Giessen [57], examined the influence of stress induced phase transformation on toughness development during crack growth. Constitutive equations are derived from Sun *et al.* [58], to model phase transformations in zirconia ceramics and in shape memory alloys. They assumed fully martensite acts linear-elastically. They showed that reversibility of the transformation significantly reduces the toughness increase.

Birman studied the size of plastic zone near the crack tip and effect of stress induced martensitic transformation on the stress intensity factor. He analyzed isothermal Mode I fracture problem of SMA using two dimensional version of Tanaka [59], constitutive model. His results indicated that effect of phase transformation on stress intensity factor is relatively small and magnitude of stress intensity factor can be calculated by using properties of austenite.

In an experimental work McKelvey and Ritchie [60], studied effect of martensitic transformation on crack growth under dynamic loading. Compared to other biomedical implant alloys, the fatigue crack growth resistance of NiTiNOL was the lowest.

Yan *et al.* [61], used FEA to observe effect of stress induced martensite transformation on fracture behavior of SMAs. They concluded that there is a volume contradiction during forward phase transformation. Negative volumetric strain increases the stress intensity factor near crack tip and decreases toughness. Following study by Yan *et al.* [62], in 2003, effect of plasticity on stress induced transformation is studied. The transformation constitutive model is adopted from a generalized plastic model with Drucker-Prager type phase transformation functions and the plasticity is described using von Mises isotropic hardening model. As internal variable martensite volume fraction is used.

In an experimental study by Wang *et al.* [63], fracture toughness is measured using cracked compact tension (CT) specimen under fatigue load. They concluded that the shape of martensitic transformation region looks like plastic deformation region thus they can be modeled in a similar manner.

Daly *et al.* [64], experimentally studied fracture properties of NiTi sheets under Mode I loading using digital image correlation (DIC) technique and linear elastic fracture mechanics (LEFM). They concluded that phase transformation at the crack tip is related to toughening.

Robertson *et al.* [65], used X-ray diffraction method to obtain strain fields of an edge cracked NiTi specimen under mode I loading. They presented that phase transformation reduces stress near crack tip and increases fracture resistance. It has been seen that LEFM methods and assumptions are rough estimates and more proper approach is needed.

In an experimental study Gollerthan *et al.* [66], effect of pseudoelasticity on mechanical behavior of compact tension specimens is investigated. Approaches from LEFM are used to determine critical stress intensity factors (K_{max}) for several a/W ratios. They concluded that for small specimens, direct use of LEFM is out ruled by other parameters. K_{max} does not depend on a/W for $0.45 < a/W < 0.55$.

Xiong and Liu [67], studied the effect of stress induced martensitic transformation on the stress intensity factor in Ni-Mn-Ga, NiTi and Cu-Al-Ni alloys. According to the results they have found the stress field around the crack tip is modified with the martensitic transformation causing to an increase in SIF at the crack tip. When temperature is lowered transformation zone expands.

Maletta and Furgiuele [68], came up with an idea of defining new fracture parameters for NiTi based SMAs. They suggested two different SIFs for austenite and martensite to describe the stress distribution for both transformed and untransformed region. Their results indicated that stress induced transformation has a toughening effect as the fracture occurs in the martensitic region. Moreover toughening effect is larger when decreasing the transformation strain and increasing the transformation stress. Maletta [69], suggested an approach with trilinear stress strain behavior which does not take into account the plastic deformation occurring at the very crack tip, in SMAs martensitic region. In their recent work Maletta *et al.* [70] analyzed temperature dependent fracture properties of NiTi based SMA. They found that temperature has an important role on stress intensity factor and on other fracture parameters. They proposed a temperature independent fracture toughness parameter.

Baxevanis and Lagoudas [71], analyzed a center cracked infinite SMA under plane stress in mode I. The sizes of fully and partially transformed regions and plastic region are numerically evaluated. A relationship between J-integral and CTOD is formulated. They also concluded that presence of transformation region decreases the plastic zone region.

In the experimental study by LePage *et al.* [72], full field surface displacement and temperature measurements are done with DIC to characterize thermo-mechanical behavior of SMA under mode I loading.

Haghgouyan *et al.* [73], investigated effect of phase transformation on fracture parameters of SMAs experimentally and computationally. Tensile tests are conducted both in room temperature and at 100^0C which give totally different stress-strain curves.

According to the recent numerical study of Ardakani *et al.* [74], increasing the loading rate results in thermo-mechanical coupling effect which decreases the available energy for crack growth. It also increases the stress during forward phase transformation while diminishing the transformation zone.

Ozerim *et al.* [75], estimated the crack tip transformation region in closed form using asymptotic equations of Hutchinson-Rice-Rosengren.

Most of the works mentioned here assumed phase transformation occurs isothermally. Even though there are experiments conducted at different temperatures to observe thermomechanical behaviour of SMA, temperature increase at the crack tip due to dissipation is disregarded. Experimental studies [42, 76, 77] and analytical results [7, 78] showed that mechanical behavior of the SMAs are strongly rate dependent due to strong thermomechanical coupling.

5.3. Problem Statement

Main objective is to quantify the impact of thermomechanical coupling effect on fracture parameters of SMAs. In this regard there are experimental works conducted at different rates, where thermomechanical coupling impact is different. Mutlu [9] used the following NiTiNOL CT specimen in Fig: 5.1 with different loading rates (0.1 mm/min to 2.0 mm/min).

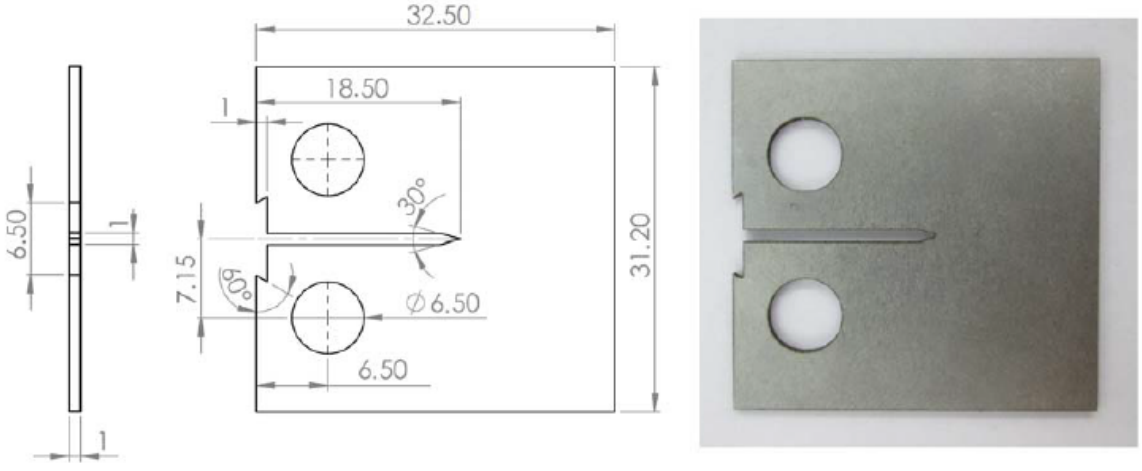

Figure 5.1. Dimensions of the NiTiNOL Plate.

As an extension to experimental and analytical work of Mutlu, finite element analysis is conducted using ABAQUS. In FE analysis, original, modified and uncoupled ZM models are used and the results are compared to the analytical and experimental results. 0.1 mm/min (lowest) and 2.0 mm/min (highest) strain rates are applied from center of the hole.

5.4. Evaluation of Stress Intensity Factor

Assuming SMAs undergo small scale yielding at the crack tip, linear elastic fracture mechanics(LEFM) could be applied to calculate stress intensity factor(SIF). According to ASTM E399 standard critical stress intensity factor, K_Q, that is achieved

when applied force P, starts to propagate crack, is written for edge cracked specimens as follows [79]:

$$K_Q = \frac{P}{B\sqrt{W}} f\left(\frac{a}{W}\right) \tag{5.1}$$

where B is the specimen thickness, a is the crack length and W is the width, measured from center of loading holes to edge. $f\left(\frac{a}{W}\right)$ is the geometric factor and its value for the specimen in Fig. 5.1 is:

$$f\left(\frac{a}{W}\right) = \frac{\left(2+\frac{a}{W}\right)\left[0.886 + 4.64(\frac{a}{W}) - 13.32(\frac{a}{W})^2 + 14.72(\frac{a}{W})^3 - 5.6(\frac{a}{W})^4\right]}{1-(\frac{a}{W})^{\frac{3}{2}}} \tag{5.2}$$

SIF can be determined by using displacement data u_y. Displacement data can be obtained either experimentally (DIC) or in this case by using FEM. By using least-square fit done by Oral *et al.* [80], and u_y data obtained from FEM, SIF and other fracture parameters can be estimated.

$$u_y = \frac{K_I}{2\mu}\left(\frac{r}{2\pi}\right)^{\frac{1}{2}} sin\frac{\theta}{2}\left(\frac{3-v}{1+v} - cos\theta\right) - \frac{Tv}{2\mu(1+v)} r sin\theta \tag{5.3}$$

$$+\frac{K_{II}}{4\mu}\left(\frac{r}{2\pi}\right)^{\frac{1}{2}}\left(\frac{5v-3}{1+v}cos\frac{\theta}{2} - cos\frac{3\theta}{2}\right) + A_1 r cos\theta + u_{0y}$$

In this equation, v is possions ratio, μ is the shear modulus and known variables. T is the stress acting parallel to the crack plane also known as T-stress, A_1 is the rigid body rotation where as u_{0y} is the rigid body displacement. Using Eq. 5.3 and MATLAB code for numerical calculations T, A_1, u_{0y}, K_I and K_{II} can be found.

Another method of evaluating SIF is using J integral which is obtained from finite elements.

5.4.1. Strain Energy Release Rate and J Integral

During fracture, energy dissipation at the crack tip due to formation of new surfaces and other dissipative processes cause a strain energy release. Strain energy release rate G, is the energy dissipated per unit of newly created surface area. Relationship between G and K is written for linearly elastic homogeneous materials as Irwin shows [79]:

$$G = \frac{K_I^2}{E'} \tag{5.4}$$

$$E' = E \qquad \text{for plane stress} \tag{5.5}$$

$$E' = \frac{E}{1 - v^2} \quad \text{for plane strain} \tag{5.6}$$

Rice developed a fracture parameter, J-integral, that is valid for linear or non-linearly elastic homogeneous materials with a uniform temperature distribution [81]. J integral is contour independent and equal to strain energy release rate G.

$$G = J = \int_\Gamma W dy - \int_\Gamma T_i \frac{\partial u_i}{\partial x} ds \tag{5.7}$$

where Γ is the contour of the J integral, W is the strain energy density, T_i is the traction vector, u_i is the displacement components, dy, ds are the length increments. J values are accessible in ABAQUS in fracture mechanics allowing calculation of SIF.

5.5. Computational Evaluation of Fracture Parameters

At the crack tip, since high stresses are achieved in a short amount of time, the material behaves like it is subjected to high strain rates and it is expected that tem-

perature increases significantly near crack tip. Since this thesis deals with fracture of SMAs at which strong thermomechanical coupling is observed, original coupled model needs a modification. With implemented modification explained above, simulations at the crack tip are expected to reflect the mechanical behaviour more realistically.

Finite elements software ABAQUS is used to evaluate fracture parameters and the transformation regions. To be able to compare to experimental results, material parameters in the work of Mutlu [9], are used. Simulations are conducted using original coupled, original uncoupled and modified ZM model, the latter gives better results at higher strain rates. CT specimen with the geometry in Fig. 5.1 is modeled with a fatigue precrack same length as the experiments. Upper half of the geometry is drawn in order to reduce the computational time. Boundary conditions and the model can be seen in Fig. 5.2:

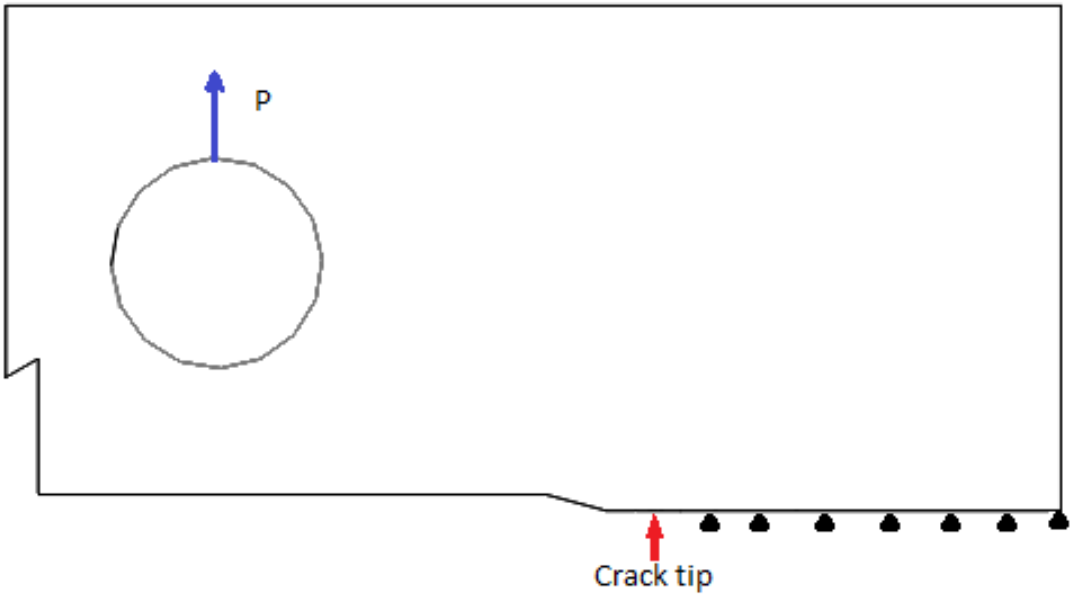

Figure 5.2. FE Geometry of CT Specimen, Loading and Boundary Conditions.

A coarser mesh is used in the far field region to reduce the computational time, and a fine mesh is used near the crack tip for accurate results. C3D8T 8 node, thermally coupled brick, trilinear displacement and temperature element type is used. Mesh

refinement towards the crack tip can be seen in Fig. 5.3

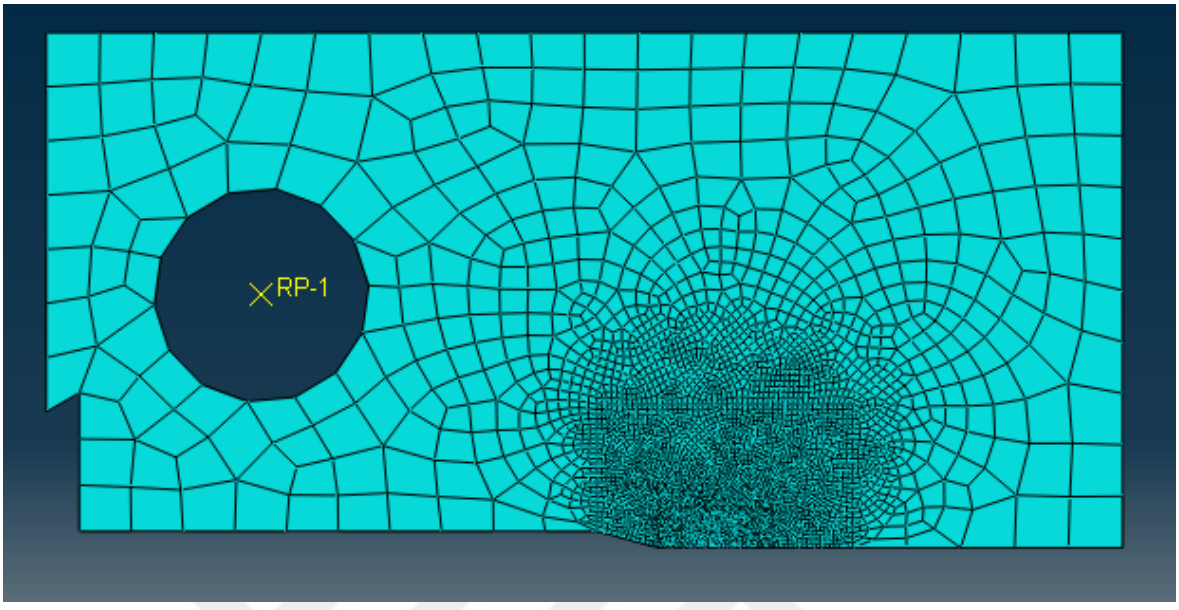

Figure 5.3. Mesh of the CT Specimen.

Following material properties found in tensile experiments of Mutlu [9], are used.

Table 5.1. Material Properties.

E_A	62500 MPa	b	7.2176 MPa
E_M	45000 MPa	ϵ_0	0.05
v	0.33	G	5.7943 MPa
Y	110 MPa	β	4400 MPa
α	2200 MPa	κ	1.7019 MPa
ζ	0.830 MPa/K	T	303.15 K
A_f^0	289.15 K	t_a	$1.1e^{-5}$ 1/K
a	7.20192 MPa	t_m	$6.6e^{-6}$ 1/K
m	20000s	n	0.062

$P = 513.4$ N is applied incrementally in y direction as shown in Fig. 5.2. Same geometry and boundary conditions are used for the simulation of linearly elastic austenite and linearly elastic martensite with the following material parameters.

Table 5.2. Material Properties.

E_A	62500 MPa
v	0.33

Table 5.3. Material Properties.

E_M	45000 MPa
v	0.33

5.6. Results

The results are obtained from ABAQUS simulation and compared to experimental and DIC results of Mutlu [9].

5.6.1. Transformation Region

Table 5.4 shows the size of the martensitic region r_M and that of the phase transformation region r_T; r_M and r_T are full martensitic zone and phase transformation sizes evaluated at $\theta = 0$.

Table 5.4. r_M and r_T Values for $\dot{\epsilon} = 2$mm/min.

	r_M (mm)	r_T (mm)
Analytical (K_I from DIC calculation)	0.39	0.83
Analytical (K_I from ASTM E399)	0.3084	0.663
Original coupled ZM model	0.01	1.12
Modified ZM model	0.01	1.02
Uncoupled ZM model	0.015	1.175

ZM model estimates martensitic region much smaller than the experimentally calculated ones. Both numerically and experimentally calculated transformation regions are between the $0.6 - 1.1$ mm range. Modified model estimates the transformation region slightly smaller than the original coupled model. Impact of modification is not measurable since the exact transformation region sizes are not available, experimentally calculated ones are also estimates based on assumptions. When coupled an uncoupled models are compared, it can be seen that in coupled models transformation region is smaller. This is because, in coupled models temperature of the specimen increases near crack tip, thus more stress is needed to transform the material.

5.6.2. Fracture Parameters

Stress intensity factors are determined from J contour integral values calculated using FE. Assuming small scale transformation zone at the crack tip following relation can be used to calculate K_I assuming LEFM.

$$J = \frac{K^2}{E} \tag{5.8}$$

J values for modified and original coupled model, and for the linearly elastic austenite and martensite are obtained using contours # between $10 - 65$, which can be seen in Fig. 5.4.

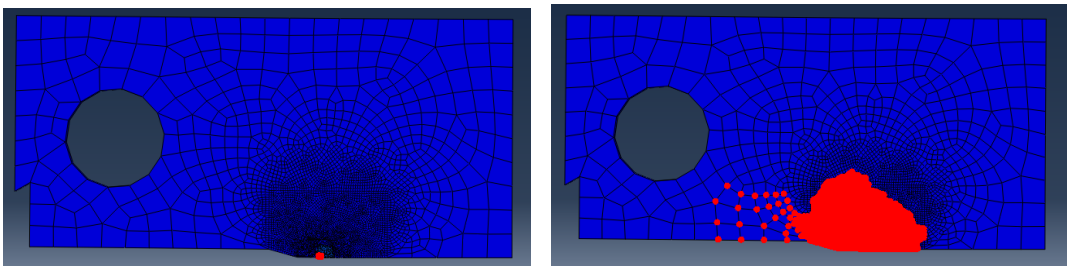

(a) Contour # 10 (b) Contour # 65

Figure 5.4. Contour Numbers 10 and 65 and Their Corresponding Effective Regions.

The contour numbering starts with # 1 at the crack tip, and increases with the radius. Since the first contours near the crack tip has a mixed combination of austenite and martensite due to transformation, it is not possible to use a proper Young modulus E to estimate K, so it is found to be appropriate to start evaluation of the J-integrals from the contour # 10.

J integral values in $\frac{kJ}{m^2}$ between contour # $10-65$ for the simulations can be seen in Fig. 5.5. Note that applied global force is increases linearly with time.

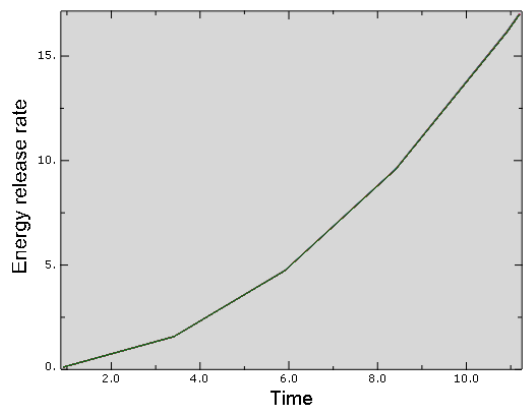

(a) J-austenite

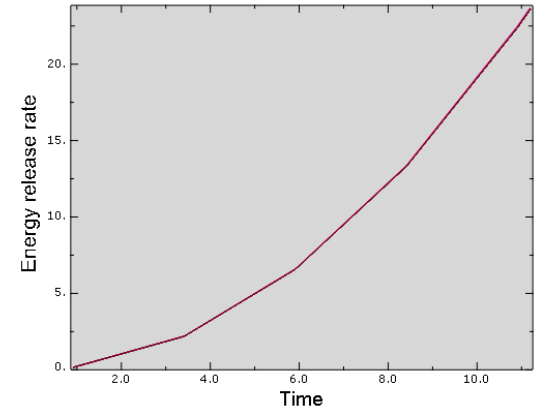

(b) J-martensite

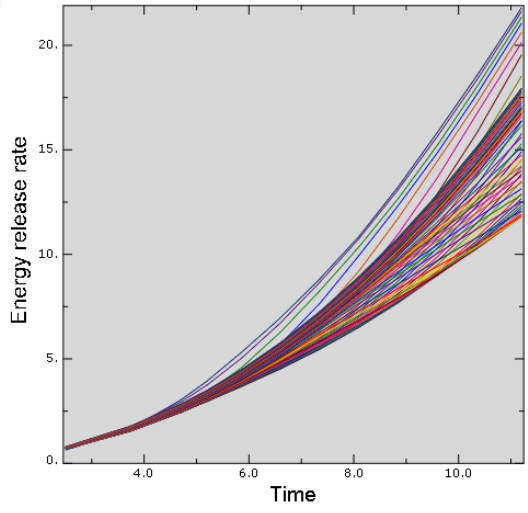

(c) J-original

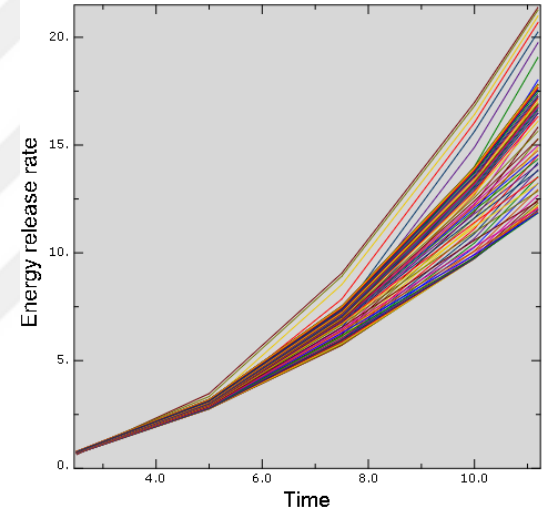

(d) J-modified

Figure 5.5. Energy Release Rate J ($\frac{kJ}{m^2}$) vs Time for the Simulations.

Fig. 5.6 shows the J integral values versus contour # of the four different simulations.

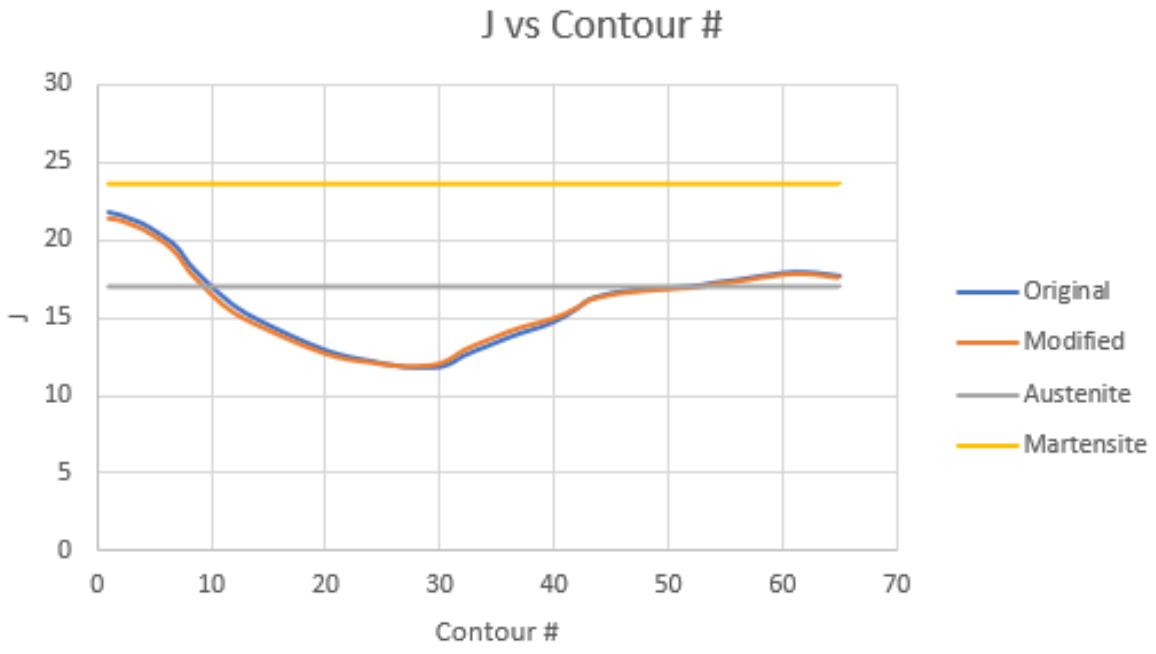

Figure 5.6. J vs Contour #.

In the simulation of the linearly elastic martensite and austenite, J integral is constant regardless of the contour region. Linearly elastic martensite has higher J values compare to austenite due to its lower elastic modulus. In the simulation of the NiTi, J integral takes higher values near the crack tip since dominant phase is martensite with a low elastic modulus. Outside the transformation region where contour number is higher than 50, composition is fully austenite and J values tend to stabilize around the linearly elastic austenite values. The J values of original and modified models are very close to each other.

Using Eq. 5.8 and the maximum J values obtained at far field contour # 65, stress intensity factors are calculated and compared to experimentally calculated ones [9] at Table 5.5.

Displacement fields, obtained from FE simulation are fitted to Eq. 5.3 and stress intensity factor is calculated both for original and modified models. No significant difference is observed.

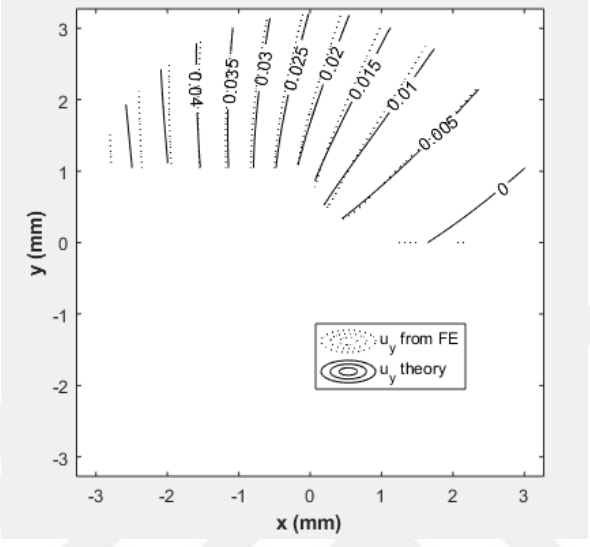

Figure 5.7. Displacement Contour Plots Obtained from FE and Eq. 5.3 Original Model.

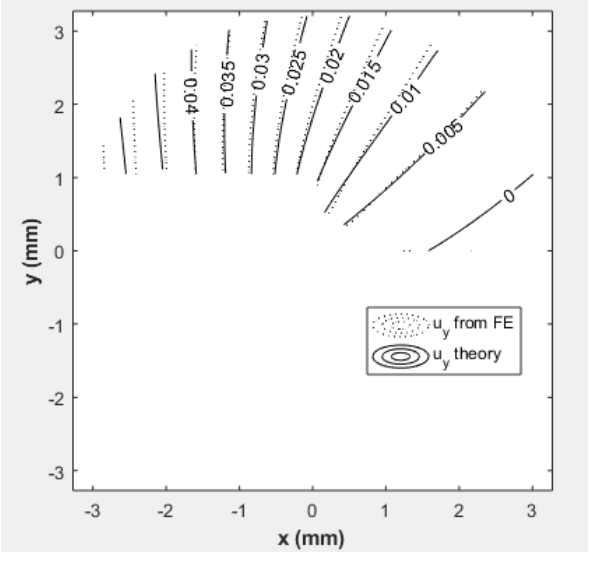

Figure 5.8. Displacement Contour Plots Obtained from FE and Eq. 5.3 Modified Model.

Table 5.5. Stress Intensity Factor K_I.

Method	K_I $(MPa\sqrt{m})$
DIC Least squares fit	33.81
FE Least squares fit (original)	34.71
FE Least squares fit (modified)	34.76
Experimental ASTM E399	30.11
Experimental LEFM J-K relation	30.62
Original coupled ZM model (FE - J integral)	33.25
Modified ZM model (FE - J integral)	33.13
Uncoupled ZM model (FE - J integral)	34.14
Linearly elastic austenite (FE - J integral)	32.61
Linearly elastic martensite (FE - J integral)	32.59

Modified model estimates K_I slightly lower than the original coupled model according to J intergral calculation and slightly higher according FE least squares fit. They both in the range of $30 - 35MPa\sqrt{m}$ range. No significant change between original and modified version is observed.

Crack mouth opening displacements (CMOD) are obtained from finite elements simulations using original and modified model and compared to experimental result of Mutlu [9].

Table 5.6. Crack Mouth Opening Displacement, CMOD.

Method	$CMOD(mm)$	Error %
Experimental	0.4323	–
Original coupled ZM model	0.473	9.5
Modified ZM model	0.470	8.7
Uncoupled ZM model	0.479	10.8

Modified model estimates the CMOD, with slightly less error compared to original coupled model and uncoupled model.

5.6.3. Temperature and Transformation Around the Crack Tip

The temperature of the crack tip increases to 303.7 K from 303.15 K for both original and modified models. The transformation phase occurs rapidly at a very small area near the crack tip due to stress intensity in that area. Even though the heat generation rate per unit volume is high near the crack tip due to high local strain rates around the region, its volume is so small that it increases the temperature of the region by less then 0.5 K. The volume, where the transformation occurs and the heat is generated, is very tiny, compared to the remainder of the body. When the heat generated in the tiny transformation volume is conducted to the remainder of the body, its temperature increases only by a small amount (0.5 degrees). In Fig. 5.9, the evolution of temperature at the crack tip ($r = 0.01$ mm) and at the boundary of transformation region ($r = 0.78$ mm) are plotted.

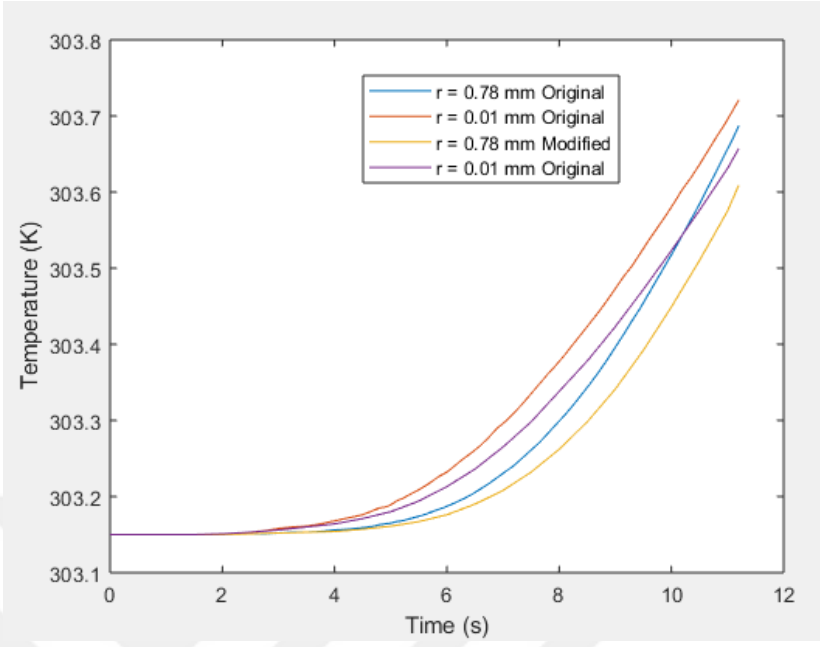

Figure 5.9. Temperature (K) vs Time (s) at the Crack Tip and at the Boundary of Transformation Region.

Because the transformation starts at lower stress levels when the original coupled model is used, the transformation initiates earlier compared to the modified model, causing an earlier increase in temperatures. The experimental data used in this simulation are obtained from the experiment that last 11.2 seconds(fastest experiment), enough for a metallic alloy to diffuse the generated heat through conduction. Figures showing temperature contours and transformation region are as follows:

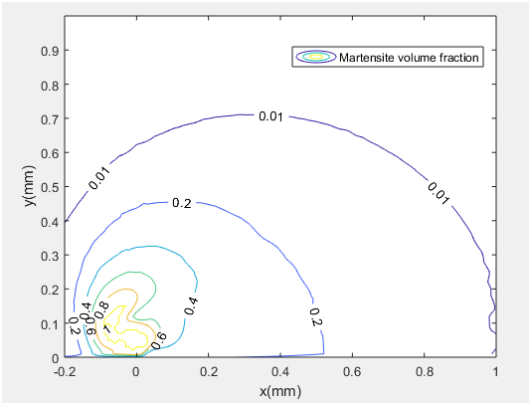

(a) original coupled model

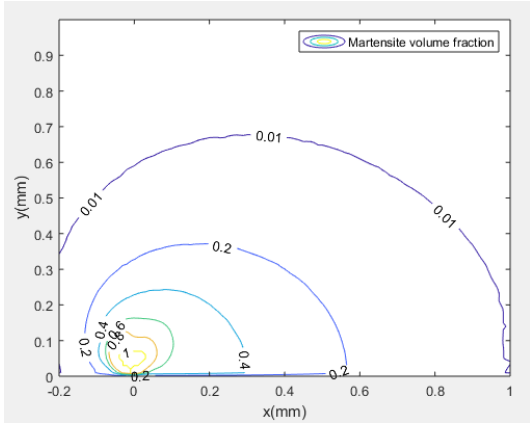

(b) Modified model

Figure 5.10. Martensite Volume Ratio (z) Contours.

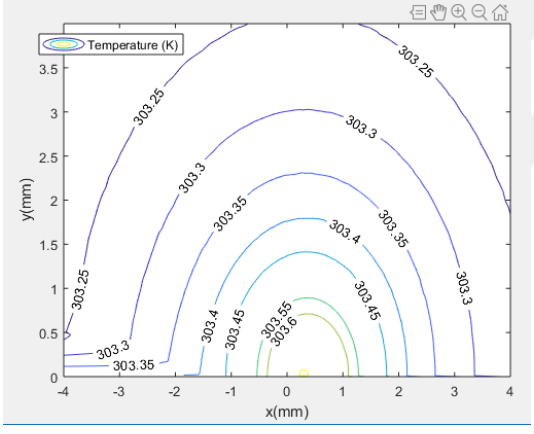

(a) original coupled model

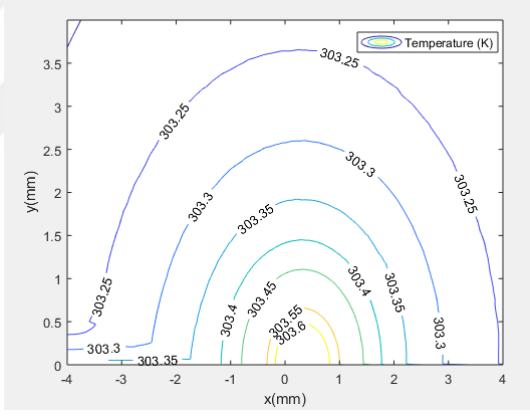

(b) Modified model

Figure 5.11. Temperature (K) Contours.

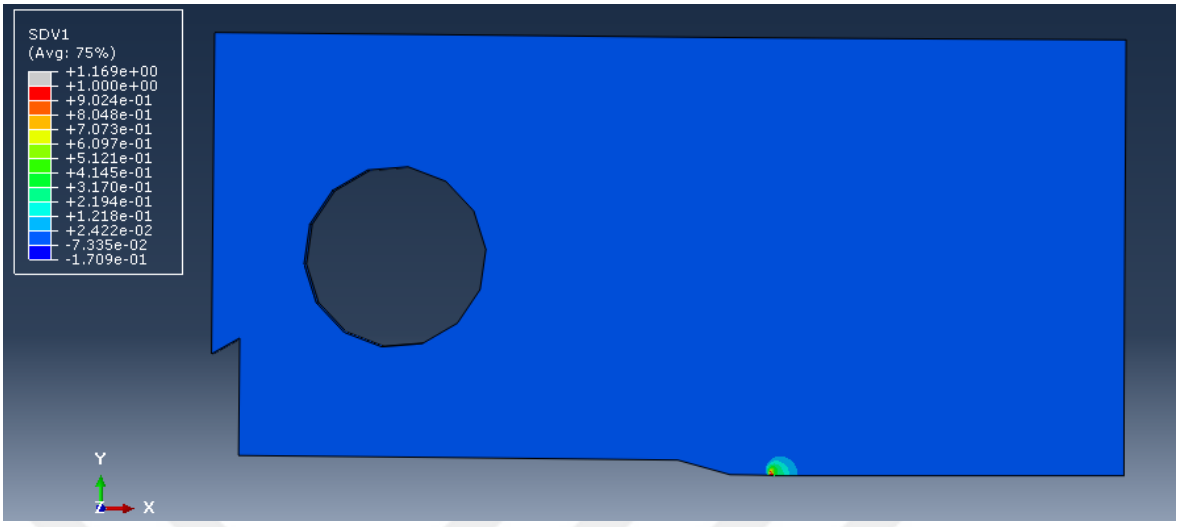

Figure 5.12. Martensitic Volume Fraction Contours.

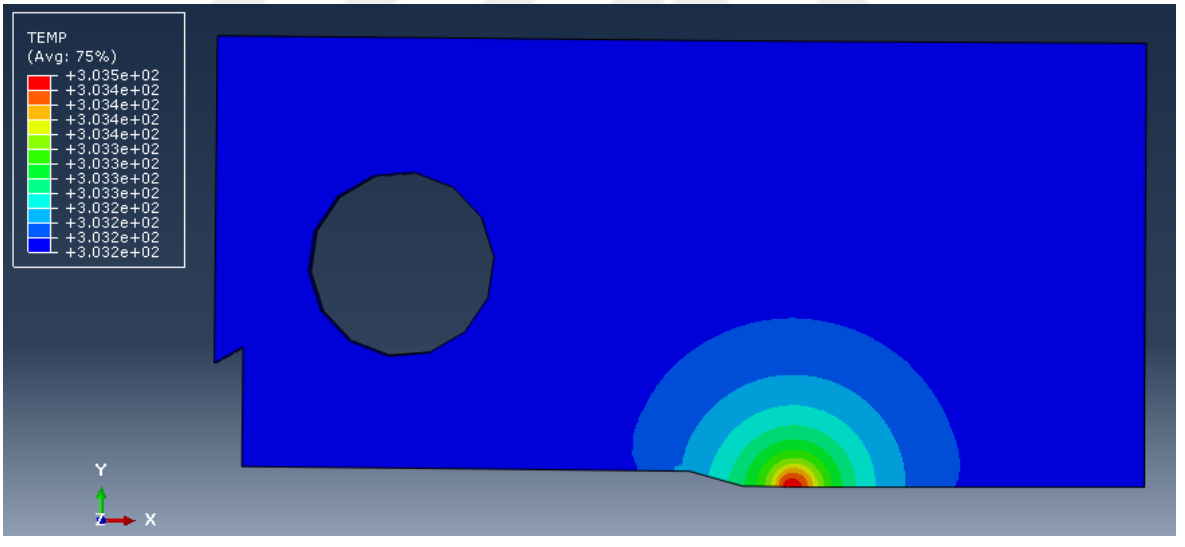

Figure 5.13. Temperature Contours.

5.6.4. Discussion

When linearly elastic austenite and martensite are simulated using ABAQUS, their energy release rate does not change over the contours and their calculated stress intensity factors are equal. The transformation at the crack tip of NiTi, causes J values

to be high closer to crack tip like linearly elastic martensite where main composition is martensite. At far field, J values are close to that of linearly elastic austenite where material is fully austenitic.

In the simulation of NiTi, the temperature of fully austenitic regions increase due to conduction shown in figure 5.13 as well. So the temperature increase at the crack tip is not as high as it is expected, thus the modification has only a minor influence. The impact of the modification to the calculation of stress intensity factor could not be determined since the experimental ones are not in an agreement. Another problem with the data is that only mechanical data (stress-strain) are taken and there are no thermal data, so actual temperature of the material is not known. To be able to assess the impact of thermomechanical coupling on fracture of SMAs, experiments with higher strain rates rates together with thermal cameras are essential. Since change of temperature is not known experimentally, we can only speak of computed ones. Computed temperature change is low, therefore effect of modification of the model is slight. To further test the proposed method, comparable experimental results obtained at higher strain rates with higher temperature change is necessary. The impact of modification seems to be negligible since temperature at the crack tip increases only 0.5 degrees according to the simulation results. The effect of modification would be more worth, when strain rate is higher and experiment duration is lower, so heat generation rate at the crack tip will be higher and the temperature increases will be significant. Unfortunately we do not have faster experimental fracture data to validate the model in fracture mechanics, however it's performance in NiTi wires has been shown in previous chapter.

6. CONCLUSION

This work aimed the investigation of effect of thermomechanical coupling on mechanical behavior of and fracture SMAs. Among several constitutive models, ZM model which includes thermomechanical coupling is studied and improved. SMAs exhibit a strong thermomechanical coupling where temperature of the behavior directly impacts the mechanical behavior and vice versa. Constitutive ZM model, accounts for theromechanical coupling of SMAs is studied and re-derived in Chapter 2.

In Chapter 3, effect of various parameters defined in ZM model is investigated. During the rederivation of constitutive model it is realized that, material parameters a, b and G are defined assuming isothermal material temperature. However, material temperature is not constant during the transformation. Material parameters a, b and G are modified as if material temperature changes with the described method in Chapter 3, however obtained results were not satisfactory. Nevertheless determination of a, b and G assuming isothermal material temperature is found to be problematic and remarked. Examining experimental works of [8], [38] and [9] another modification of σ_{ms}, thus material parameters a and G, is proposed. Based on the work of Tobushi *et al.* [8], σ_{ms} is modified to be a function of strain rate. To achieve corresponding relation between σ_{ms} and strain rate, new material parameters m and n are defined. For finite elements simulation, ZM coupled model algorithm is modified in a way so that values of, a and G which are a function of σ_{ms} are dependent on local strain rate, rather than using constant a and G. With the modification material parameters a and G which determines the shape of the stress-strain curve become a function of strain rate.

In Chapter 4, various simulation results related to thermomechanical behavior of SMAs are demonstrated using MATLAB and ABAQUS. To better understand and visualize the transformation phenomenon 2D and 3D transformation surfaces are drawn using transformation function. Using stresses at $z = 0$ and $z = 1$ cases yield surfaces are drawn, and as expected an expansion of the yield surface is observed. Also with the increase in material temperature yield surface expands. With increasing strain

rates martensite start stress also increases which could not be captured using the original model and achieved with the modification of the material parameter a. 3D transformation yield surfaces of the transformation function at different conditions are visualized. Interestingly, different from von Mises yield theory, according to ZM model, material could yield(transform) if it is subjected to a finite stress without distortion. In the case of von Mises yield criterion when shear stresses are zero and $\sigma_1 = \sigma_2 = \sigma_3$ material does not yield. Our results using the ZM model shows that without shear stress when $\sigma_1 = \sigma_2 = \sigma_3 = 1600$ MPa, forward transformation starts which is a counter argument for von Mises yield theory. This phenomenon has not been tested experimental yet, so we can not further interpret the findings. Yet, the demonstration of the transformation yield surfaces in 3D could lead to and encourage new researches to understand transformation mechanism of SMAs under different conditions.

Effect of phase change heat density, $C(T)$, is demonstrated using uncoupled model in ABAQUS. Dogbone specimen is subjected loading-unloading at different initial temperatures and stress-strain curves are shown.

Validation of the modified model is done using experimental data of Shaw and Kyrkiades [38]. A NiTi wire is modeled and FE simulation is run at different strain rates using the original and modified models. Results in Chapter 4, show that considerable improvement is achieved at higher strain rates in capturing stress-strain behavior compare to that of original coupled ZM-model. We proposed usage of only modified a with the σ_{ms}, since modification of G disturbs the slope of transformation plateau, yet, with the modification of only a, martensite start stress is successfully captured. Also modification of σ_{af} is postponed, since thermomechanical coupling already changes austenite finish stresses and further modifying it with the proposed strain rate relation does not give accurate results. Error of estimation of hysteresis area is reduced by half when the proposed new method is used in a new UMAT.

In Chapter 5, fracture mechanics of SMAs is explained briefly. SMA fracture specimen is modeled and analyzed using the uncoupled, original and new modified UMAT in ABAQUS and transformation regions and stress intensity factor are calculated and

compared to experimental results of Mutlu [9]. It has been seen that in the simulations, even with the highest strain rate, temperature at the crack tip does not change considerably. Since thermal data of the experiments were not available, interpretation and validation of the model is not possible. Far field J integrals are demonstrated for different models which are used to determine stress intensity factors. Modified model estimates the SIF and transformation region in the range of other methods. However the difference between the modified model and original model is negligible. There is a difference in SIF values of coupled and uncoupled models but we can not exactly say which is more realistic since there is not a consensus on experimental determination for SIF. Experimentally measured CMOD values and coupled-uncoupled models are compared. It is seen that modified model is closest to experimental results. Temperature field and transformation region obtained from FE analysis is demonstrated. It is seen that temperature of the specimen increases only 0.5 degrees at the crack tip and generated heat is conducted around the crack tip. The low increase of temperature at the crack tip is one of the limitations of this work. Results obtained with proposed method using tensile specimens where heat generation is spread through the body and temperature increase is higher, the modified method gives better results. Fracture specimens with much higher strain rates could be analyzed with the proposed method if any validating experiments with higher strain rates and thermal data are conducted in the future.

Fracture simulations using coupled and uncoupled models and fracture experiments assert that, if the fracture is completed at more than 11.2 seconds, large portion of generated heat at the crack tip dissipates over the body. Temperature increase at the crack tip and the specimen is minimal. So one can use, uncoupled, original or modified model to simulate material behavior and they do not differ much. However in the case of dogbone specimen or wires, material temperature changes considerably thus thermomechanical coupling effect becomes dominant. Original coupled model estimates the mechanical behavior better than uncoupled; and newly proposed model better than original coupled model. For future work, fracture tests conducted at higher strain rates with a thermal camera would be very helpful to validate and improve the proposed model for the estimation of fracture parameters.

REFERENCES

1. Chauhan, A., S. Patel, R. Vaish and C. R. Bowen, "A review and analysis of the elasto-caloric effect for solid-state refrigeration devices: Challenges and opportunities", *MRS Energy & Sustainability*, Vol. 2, 2015.

2. Lagoudas, D. C., *Shape memory alloys: modeling and engineering applications*, Springer Science & Business Media, 2008.

3. Ave., S. A., *Aerofit*, `http://www.aerofit.com/sma-cryofit-couplings`, accessed in April 2019.

4. Petrini, L. and F. Migliavacca, "Biomedical applications of shape memory alloys", *Journal of Metallurgy*, Vol. 2011, 2011.

5. Neugebauer, R., A. Bucht, K. Pagel and J. Jung, "Numerical simulation of the activation behavior of thermal shape memory alloys", *Industrial and Commercial Applications of Smart Structures Technologies 2010*, Vol. 7645, p. 76450J, International Society for Optics and Photonics, 2010.

6. Zaki, W. and Z. Moumni, "A three-dimensional model of the thermomechanical behavior of shape memory alloys", *Journal of the Mechanics and Physics of Solids*, Vol. 55, No. 11, pp. 2455–2490, 2007.

7. Morin, C., Z. Moumni and W. Zaki, "A constitutive model for shape memory alloys accounting for thermomechanical coupling", *International Journal of Plasticity*, Vol. 27, No. 5, pp. 748–767, 2011.

8. Tobushi, H., Y. Shimeno, T. Hachisuka and K. Tanaka, "Influence of strain rate on superelastic properties of TiNi shape memory alloy", *Mechanics of Materials*, Vol. 30, No. 2, pp. 141–150, 1998.

9. Mutlu, F., *Effect of loading rate on fracture of NiTi*, Master's Thesis, Bogazici University, Turkey, 2016.

10. Wikipedia, *von Mises Yield Surfaces*, `https://en.wikipedia.org/wiki/Von_Mises_yield_criterion/media/File:Yield_surfaces.svg`, accessed in February 2019.

11. Ölander, A., "An electrochemical investigation of solid cadmium-gold alloys", *Journal of the American Chemical Society*, Vol. 54, No. 10, pp. 3819–3833, 1932.

12. Buehler, W. J., J. Gilfrich and R. Wiley, "Effect of low-temperature phase changes on the mechanical properties of alloys near composition TiNi", *Journal of applied physics*, Vol. 34, No. 5, pp. 1475–1477, 1963.

13. Huang, W., *Shape memory alloys and their application to actuators for deployable structures*, Ph.D. Thesis, University of Cambridge, 1998.

14. Otsuka, K. and C. M. Wayman, *Shape memory materials*, Cambridge university press, 1999.

15. Ziolkowski, A., *Pseudoelasticity of shape memory alloys: theory and experimental studies*, Butterworth-Heinemann, 2015.

16. Cisse, C., W. Zaki and T. B. Zineb, "A review of constitutive models and modeling techniques for shape memory alloys", *International Journal of Plasticity*, Vol. 76, pp. 244–284, 2016.

17. Falk, F., "Model free energy, mechanics, and thermodynamics of shape memory alloys", *Acta Metallurgica*, Vol. 28, No. 12, pp. 1773–1780, 1980.

18. Falk, F., "Ginzburg-Landau theory of static domain walls in shape-memory alloys", *Zeitschrift für Physik B Condensed Matter*, Vol. 51, No. 2, pp. 177–185, 1983.

19. Ball, J. M. and R. D. James, "Fine phase mixtures as minimizers of energy",

Archive for Rational Mechanics and Analysis, Vol. 100, No. 1, pp. 13–52, 1987.

20. Idesman, A., V. Levitas, D. Preston and J.-Y. Cho, "Finite element simulations of martensitic phase transitions and microstructures based on a strain softening model", *Journal of the Mechanics and Physics of Solids*, Vol. 53, No. 3, pp. 495–523, 2005.

21. Zhong, Y. and T. Zhu, "Phase-field modeling of martensitic microstructure in NiTi shape memory alloys", *Acta Materialia*, Vol. 75, pp. 337–347, 2014.

22. Sun, Q. P. and K. C. Hwang, "Micromechanics modelling for the constitutive behavior of polycrystalline shape memory alloys—I. Derivation of general relations", *Journal of the Mechanics and Physics of Solids*, Vol. 41, No. 1, pp. 1–17, 1993.

23. Huang, M., X. Gao and L. C. Brinson, "A multivariant micromechanical model for SMAs Part 2. Polycrystal model", *International Journal of Plasticity*, Vol. 16, No. 10-11, pp. 1371–1390, 2000.

24. Blanc, P. and C. Lexcellent, "Micromechanical modelling of a CuAlNi shape memory alloy behaviour", *Materials Science and Engineering: A*, Vol. 378, No. 1-2, pp. 465–469, 2004.

25. Levitas, V. I. and I. B. Ozsoy, "Micromechanical modeling of stress-induced phase transformations. Part 1. Thermodynamics and kinetics of coupled interface propagation and reorientation", *International Journal of Plasticity*, Vol. 25, No. 2, pp. 239–280, 2009.

26. Patoor, E., D. C. Lagoudas, P. B. Entchev, L. C. Brinson and X. Gao, "Shape memory alloys, Part I: General properties and modeling of single crystals", *Mechanics of materials*, Vol. 38, No. 5-6, pp. 391–429, 2006.

27. Fremond, M., "Matériaux à mémoire de forme", *Comptes rendus de l'Académie des sciences. Série 2, Mécanique, Physique, Chimie, Sciences de l'univers, Sciences de*

la Terre, Vol. 304, No. 7, pp. 239–244, 1987.

28. Tanaka, K., "A thermomechanical sketch of shape memory effect: one-dimensional tensile behavior", *Res. Mechanica*, Vol. 18, pp. 251–263, 1986.

29. Liang, C. and C. A. Rogers, "One-dimensional thermomechanical constitutive relations for shape memory materials", *Journal of intelligent material systems and structures*, Vol. 8, No. 4, pp. 285–302, 1997.

30. Brinson, L. C., "One-dimensional constitutive behavior of shape memory alloys: thermomechanical derivation with non-constant material functions and redefined martensite internal variable", *Journal of intelligent material systems and structures*, Vol. 4, No. 2, pp. 229–242, 1993.

31. Boyd, J. G. and D. C. Lagoudas, "A thermodynamical constitutive model for shape memory materials. Part I. The monolithic shape memory alloy", *International Journal of Plasticity*, Vol. 12, No. 6, pp. 805–842, 1996.

32. Lagoudas, D. C., Z. Bo and M. A. Qidwai, "A unified thermodynamic constitutive model for SMA and finite element analysis of active metal matrix composites", *Mechanics of Composite Materials and Structures*, Vol. 3, No. 2, pp. 153–179, 1996.

33. Raniecki, B., C. Lexcellent and K. Tanaka, "Thermodynamic models of pseudoelastic behaviour of shape memory alloys", *Archiv of Mechanics, Archiwum Mechaniki Stosowanej*, Vol. 44, pp. 261–284, 1992.

34. Raniecki, B. and C. Lexcellent, "Thermodynamics of isotropic pseudoelasticity in shape memory alloys", *European Journal of Mechanics-A/Solids*, Vol. 17, No. 2, pp. 185–205, 1998.

35. Lubliner, J. and F. Auricchio, "Generalized plasticity and shape-memory alloys", *International Journal of Solids and Structures*, Vol. 33, No. 7, pp. 991–1003, 1996.

36. Auricchio, F., R. L. Taylor and J. Lubliner, "Shape-memory alloys: macromodelling and numerical simulations of the superelastic behavior", *Computer methods in applied mechanics and engineering*, Vol. 146, No. 3-4, pp. 281–312, 1997.

37. Halphen, B. and N. quoc Son, "Plastic and visco-plastic materials with generalized potential", *Mechanics Research Communications*, Vol. 1, No. 1, pp. 43–47, 1974.

38. Shaw, J. A. and S. Kyriakides, "Thermomechanical aspects of NiTi", *Journal of the Mechanics and Physics of Solids*, Vol. 43, No. 8, pp. 1243–1281, 1995.

39. Müller, C. and O. Bruhns, "A thermodynamic finite-strain model for pseudoelastic shape memory alloys", *International Journal of Plasticity*, Vol. 22, No. 9, pp. 1658–1682, 2006.

40. Peyroux, R., A. Chrysochoos, C. Licht and M. Löbel, "Thermomechanical couplings and pseudoelasticity of shape memory alloys", *International Journal of Engineering Science*, Vol. 36, No. 4, pp. 489–509, 1998.

41. Nemat-Nasser, S. and W.-G. Guo, "Superelastic and cyclic response of NiTi SMA at various strain rates and temperatures", *Mechanics of materials*, Vol. 38, No. 5-6, pp. 463–474, 2006.

42. Grabe, C. and O. T. Bruhns, "On the viscous and strain rate dependent behavior of polycrystalline NiTi", *International Journal of Solids and Structures*, Vol. 45, No. 7-8, pp. 1876–1895, 2008.

43. Xiajun, M., *Optimization of the Shape Memory Alloy Sturctures with Respect to Fatigue*, Ph.D. Thesis, L'universite Paris-Saclay, 2017.

44. Zaki, W., S. Zamfir and Z. Moumni, "An extension of the ZM model for shape memory alloys accounting for plastic deformation", *Mechanics of Materials*, Vol. 42, No. 3, pp. 266–274, 2010.

45. Lubarda, V., "On thermodynamic potentials in linear thermoelasticity", *International Journal of Solids and Structures*, Vol. 41, No. 26, pp. 7377–7398, 2004.

46. Asaro, R. and V. Lubarda, *Mechanics of solids and materials*, Cambridge University Press, 2006.

47. Fung, Y.-c., P. Tong and X. Chen, *Classical and computational solid mechanics*, Vol. 2, World Scientific Publishing Company, 2017.

48. Maugin, G. A., "The saga of internal variables of state in continuum thermomechanics (1893–2013)", *Mechanics Research Communications*, Vol. 69, pp. 79–86, 2015.

49. Valanis, K. and S. d. Lalwani, "Thermodynamics of internal variables in the context of the absolute reaction rate theory", *The Journal of Chemical Physics*, Vol. 67, No. 9, pp. 3980–3990, 1977.

50. Zaki, W., *Modélisation thermomécanique unifiée des comportements des matériaux a mémoire de forme. Application aux chargements cycliques et a la fatigue.*, Ph.D. Thesis, Ecole Polytechnique, 2006.

51. Müller, I., "On the size of the hysteresis in pseudoelasticity", *Continuum Mechanics and Thermodynamics*, Vol. 1, No. 2, pp. 125–142, 1989.

52. Dewar, R. C., C. H. Lineweaver, R. K. Niven and K. Regenauer-Lieb, "Beyond the Second Law", *Entropy Production and Non-Equilibrium Systems*, 2013.

53. Zhu, S. and Y. Zhang, "A thermomechanical constitutive model for superelastic SMA wire with strain-rate dependence", *Smart Materials and Structures*, Vol. 16, No. 5, p. 1696, 2007.

54. Maletta, C. and F. Furgiuele, "1D Phenomenological Modeling of Shape Memory and Pseudoelasticity in NiTi Alloys", *Smart Actuation and Sensing Systems-Recent*

Advances and Future Challenges, InTech, 2012.

55. Zaki, W., "An efficient implementation for a model of martensite reorientation in martensitic shape memory alloys under multiaxial nonproportional loading", *International Journal of Plasticity*, Vol. 37, pp. 72–94, 2012.

56. McMeeking, R. and A. Evans, "Mechanics of transformation-toughening in brittle materials", *Journal of the American Ceramic Society*, Vol. 65, No. 5, pp. 242–246, 1982.

57. Stam, G. and E. van der Giessen, "Effect of reversible phase transformations on crack growth", *Mechanics of materials*, Vol. 21, No. 1, pp. 51–71, 1995.

58. Sun, Q., K. C. Hwang and S. Yu, "A micromechanics constitutive model of transformation plasticity with shear and dilatation effect", *Journal of the Mechanics and Physics of Solids*, Vol. 39, No. 4, pp. 507–524, 1991.

59. Tanaka, K. and Y. Sato, "Analysis of superplastic deformation during isothermal martensitic transformation", *Res Mech.*, Vol. 17, No. 3, pp. 241–252, 1986.

60. McKelvey, A. and R. Ritchie, "Fatigue-crack propagation in Nitinol, a shape-memory and superelastic endovascular stent material", *Journal of biomedical materials research*, Vol. 47, No. 3, pp. 301–308, 1999.

61. Yan, W., C. H. Wang, X. P. Zhang and Y.-W. Mai, "Effect of transformation volume contraction on the toughness of superelastic shape memory alloys", *Smart materials and structures*, Vol. 11, No. 6, p. 947, 2002.

62. Yan, W., C. H. Wang, X. P. Zhang and Y.-W. Mai, "Theoretical modelling of the effect of plasticity on reverse transformation in superelastic shape memory alloys", *Materials Science and Engineering: A*, Vol. 354, No. 1-2, pp. 146–157, 2003.

63. Wang, X., B. Xu, Z. Yue and X. Tong, "Fracture behavior of the compact tension

specimens in NiTi shape memory alloys", *Materials Science and Engineering: A*, Vol. 485, No. 1-2, pp. 14–19, 2008.

64. Daly, S., A. Miller, G. Ravichandran and K. Bhattacharya, "An experimental investigation of crack initiation in thin sheets of nitinol", *Acta Materialia*, Vol. 55, No. 18, pp. 6322–6330, 2007.

65. Robertson, S., A. Mehta, A. Pelton and R. Ritchie, "Evolution of crack-tip transformation zones in superelastic Nitinol subjected to in situ fatigue: A fracture mechanics and synchrotron X-ray microdiffraction analysis", *Acta Materialia*, Vol. 55, No. 18, pp. 6198–6207, 2007.

66. Gollerthan, S., D. Herberg, A. Baruj and G. Eggeler, "Compact tension testing of martensitic/pseudoplastic NiTi shape memory alloys", *Materials Science and Engineering: A*, Vol. 481, pp. 156–159, 2008.

67. Xiong, F. and Y. Liu, "Effect of stress-induced martensitic transformation on the crack tip stress-intensity factor in Ni–Mn–Ga shape memory alloy", *Acta Materialia*, Vol. 55, No. 16, pp. 5621–5629, 2007.

68. Maletta, C. and F. Furgiuele, "Fracture control parameters for NiTi based shape memory alloys", *International Journal of Solids and Structures*, Vol. 48, No. 11-12, pp. 1658–1664, 2011.

69. Maletta, C., "A novel fracture mechanics approach for shape memory alloys with trilinear stress–strain behavior", *International journal of fracture*, Vol. 177, No. 1, pp. 39–51, 2012.

70. Maletta, C., E. Sgambitterra and F. Niccoli, "Temperature dependent fracture properties of shape memory alloys: novel findings and a comprehensive model", *Scientific reports*, Vol. 6, No. 1, p. 17, 2016.

71. Baxevanis, T. and D. Lagoudas, "A mode I fracture analysis of a center-cracked

infinite shape memory alloy plate under plane stress", *International journal of fracture*, Vol. 175, No. 2, pp. 151–166, 2012.

72. *Thermomechanical characterization of shape memory alloy mode I Fracture Behavior)*, Vol. 24, ICTAM, 2016.

73. Haghgouyan, B., N. Shafaghi, C. C. Aydıner and G. Anlas, "Experimental and computational investigation of the effect of phase transformation on fracture parameters of an SMA", *Smart Materials and Structures*, Vol. 25, No. 7, p. 075010, 2016.

74. Ardakani, S. H., A. Afshar and S. Mohammadi, "Numerical study of thermomechanical coupling effects on crack tip fields of mixed-mode fracture in pseudoelastic shape memory alloys", *International Journal of Solids and Structures*, Vol. 81, pp. 160–178, 2016.

75. Özerim, G., G. Anlaş and Z. Moumni, "On crack tip stress fields in pseudoelastic shape memory alloys", *International Journal of Fracture*, Vol. 212, No. 2, pp. 205–217, 2018.

76. He, Y. J. and Q. Sun, "On non-monotonic rate dependence of stress hysteresis of superelastic shape memory alloy bars", *International Journal of Solids and Structures*, Vol. 48, No. 11-12, pp. 1688–1695, 2011.

77. Pieczyska, E. A., H. Tobushi, K. Kulasinski and K. Takeda, "Impact of strain rate on thermomechanical coupling effects in TiNi SMA subjected to compression", *Materials Transactions*, Vol. 53, No. 11, pp. 1905–1909, 2012.

78. Yu, C., G. Kang, Q. Kan and Y. Zhu, "Rate-dependent cyclic deformation of super-elastic NiTi shape memory alloy: thermo-mechanical coupled and physical mechanism-based constitutive model", *International Journal of Plasticity*, Vol. 72, pp. 60–90, 2015.

79. Anderson, T. L., *Fracture mechanics: fundamentals and applications*, CRC press, 2017.

80. Oral, A., J. Lambros and G. Anlas, "Crack initiation in functionally graded materials under mixed mode loading: experiments and simulations", *Journal of Applied Mechanics*, Vol. 75, No. 5, p. 051110, 2008.

81. Rice, J. R., "A path independent integral and the approximate analysis of strain concentration by notches and cracks", *Journal of applied mechanics*, Vol. 35, No. 2, pp. 379–386, 1968.

APPENDIX A: EQUIVALENT STRESS AND STRAIN

Strain energy density is given by:

$$\int \boldsymbol{\sigma} : \boldsymbol{\epsilon} \tag{A.1}$$

For linearly elastic materials:

$$W = \frac{1}{2}\boldsymbol{\sigma} : \boldsymbol{\epsilon} \tag{A.2}$$

Which can be expanded as:

$$W = \frac{1}{2}[\sigma_{xx}\epsilon_{xx} + \sigma_{yy}\epsilon_{yy} + \sigma_{zz}\epsilon_{zz} + 2(\sigma_{xy}\epsilon_{xy} + \sigma_{xz}\epsilon_{xz} + \sigma_{yz}\epsilon_{yz})] \tag{A.3}$$

Strain energy in principal coordinates reduces to:

$$W = \frac{1}{2}[\sigma_1\epsilon_1 + \sigma_2\epsilon_2 + \sigma_3\epsilon_3] \tag{A.4}$$

Linear elastic relations in principal stresses and strains lead to:

$$\epsilon_1 = \frac{1}{E}(\sigma_1 - v\sigma_2 - v\sigma_3) \tag{A.5}$$

$$\epsilon_2 = \frac{1}{E}(\sigma_2 - v\sigma_1 - v\sigma_3) \tag{A.6}$$

$$\epsilon_3 = \frac{1}{E}(\sigma_3 - v\sigma_1 - v\sigma_2) \tag{A.7}$$

Strain energy in terms of principal stresses can be written as:

$$W = \frac{1}{2E}[\sigma_1^2 + \sigma_2^2 + \sigma_3^2 - 2v(\sigma_1\sigma_2 + \sigma_2\sigma_3 + \sigma_1\sigma 3)] \tag{A.8}$$

Principal stress σ_p, is composed of hydrostatic stress σ_h, and deviatoric stress σ_d:

$$\begin{bmatrix} \sigma_1 & 0 & 0 \\ 0 & \sigma_2 & 0 \\ 0 & 0 & \sigma_3 \end{bmatrix} = \begin{bmatrix} \sigma_h & 0 & 0 \\ 0 & \sigma_h & 0 \\ 0 & 0 & \sigma_h \end{bmatrix} + \begin{bmatrix} \sigma_{d1} & 0 & 0 \\ 0 & \sigma_{d2} & 0 \\ 0 & 0 & \sigma_{d3} \end{bmatrix} \tag{A.9}$$

where hydrostatic stress is $\sigma_h = (\sigma_1 + \sigma_2 + \sigma_3)/3$. Distortion part of energy , is the strain energy of deviatoric stress W_d, which can be found by subtracting hydrostatic strain energy W_h, from total strain energy W.

$$W_d = W - W_h \tag{A.10}$$

$$= \frac{1+v}{3E}(\sigma_1^2 + \sigma_2^2 + \sigma_3^2 - \sigma_1\sigma_2 + \sigma_1\sigma_3 + \sigma_2\sigma_3) \tag{A.11}$$

$$= \frac{1+v}{3E}\frac{(\sigma_1 - \sigma_2)^2 + (\sigma_1 - \sigma_3)^2 + (\sigma_2 - \sigma_3)^2}{2} \tag{A.12}$$

W_d can be written in terms of equaivalent von Mises stress σ_{VM}

$$W_d = \frac{1+v}{3E}\sigma_{VM}^2 \tag{A.13}$$

where σ_{VM} equals to:

$$\sigma_{VM} = \sqrt{\frac{(\sigma_1 - \sigma_2)^2 + (\sigma_1 - \sigma_3)^2 + (\sigma_2 - \sigma_3)^2}{2}} \tag{A.14}$$

In tensorial notation stress tensor can be written as sum of hydrostatic and deviatoric stress as follows:

$$\sigma_{ij} = \frac{1}{3}\delta_{ij}\sigma_{kk} + S_{ij} \tag{A.15}$$

$\frac{1}{3}\delta_{ij}\sigma_{kk}$ being the hydrostatic stress tensor and S_{ij} is the deviatoric stress tensor. von Mises stress leads to:

$$\sigma_{VM} = \sqrt{\frac{3}{2}\sigma_{ij}\sigma_{ij} - \frac{1}{2}(\sigma_{kk})^2} \tag{A.16}$$

$$\sigma_{VM} = \sqrt{\frac{3}{2} S_{ij} S_{ij}} \tag{A.17}$$

Stress, σ can be written as sum of hydro-static stress σ_h, and deviatoric stress tensors S.

$$\sigma = \sigma_h + \sigma^{'} \tag{A.18}$$

where,

$$\sigma_h = \frac{\sigma_{xx} + \sigma_{yy} + \sigma_{zz}}{3} \tag{A.19}$$

Eq. A.3 becomes:

$$W = \frac{1}{2}(\sigma_h + \sigma^{'}) + (\epsilon_h + \epsilon^{'}) \tag{A.20}$$

$$\frac{1}{2}[(\sigma_h + \epsilon_h) + (\sigma_h + \epsilon_h^{'}) + (\sigma_h^{'} + \epsilon_h) + (\sigma_h^{'} + \epsilon_h^{'})] \tag{A.21}$$

$(\sigma_h + \epsilon_h^{'})$ and $(\sigma_h^{'} + \epsilon_h)$ is equal to zero since double dot product of hydrostatic and deviatoric stresses are zero. Expression reduces to:

$$W = \frac{1}{2}[(\sigma_h + \epsilon_h) + (\sigma_h^{'} + \epsilon_h^{'})] \tag{A.22}$$

where strain energy is divided into hydrostatic and deviatoric parts. According to distortion energy criterion, only deviatoric part of stress causes to yielding. Deviatoric strain energy can be written as:

$$W^{'} = \frac{1}{2}\boldsymbol{\sigma}^{'} : \boldsymbol{\epsilon}^{'} \tag{A.23}$$

using Hooke's law:

$$\epsilon^{'} = \frac{1}{2G}\sigma^{'} \tag{A.24}$$

where G is the shear modulus and $G = \frac{E}{2(1+v)}$. Deviatoric strain energy becomes:

$$W^{'} = \frac{1}{4G}\boldsymbol{\sigma}^{'} : \boldsymbol{\sigma}^{'} \tag{A.25}$$

Now assume there is a scalar value of σ_s which gives the same deviatoric strain energy as $\sigma_{\prime}$:

$$\sigma_s = \sqrt{\boldsymbol{\sigma}^{'} : \boldsymbol{\sigma}^{'}} \tag{A.26}$$

so deviatoric strain energy becomes:

$$W^{'} = \frac{1}{4G}(\sigma_s)^2 \tag{A.27}$$

Now assume a uniaxial tension test with following stress state:

$$\boldsymbol{\sigma} = \begin{bmatrix} \sigma & 0 & 0 \\ 0 & 0 & 0 \\ 0 & 0 & 0 \end{bmatrix} \tag{A.28}$$

When hydrostatic stress is subtracted from $\boldsymbol{\sigma}$ deviatoric stress is found as follows:

$$\boldsymbol{\sigma}^{'} = \begin{bmatrix} \frac{2\sigma}{3} & 0 & 0 \\ 0 & \frac{-\sigma}{3} & 0 \\ 0 & 0 & \frac{-\sigma}{3} \end{bmatrix} \tag{A.29}$$

Using Eq. A.29 $\boldsymbol{\sigma}^{'} : \boldsymbol{\sigma}^{'} = 2\sigma^2/3$ and:

$$\sigma_s = \sqrt{\boldsymbol{\sigma}^{'} : \boldsymbol{\sigma}^{'}} = \sqrt{\frac{2}{3}}\sigma \tag{A.30}$$

Scalar value of $\boldsymbol{\sigma}$ is also called von Mises stress σ_{VM}, and in terms of deviatoric stress,

$\sigma^{'}$ it can be written as:

$$\sqrt{\frac{3}{2}\boldsymbol{\sigma}^{'} : \boldsymbol{\sigma}^{'}} = \sigma \tag{A.31}$$

APPENDIX B: DERIVATION OF THE TANGENT OPERATORS

Mechanical properties of SMAs are strongly affected by temperature due to thermomechanical coupling. To be able to estimate SMA behavior through simulation, temperature, strain, stress fields and heat generation of structure must be known at each integration point. This numerical integration requires a identification of tangent operators which are representing the local rate of change in stress and heat generation with respect to strain and temperature. The method developed by Gu [43], provides coupling between temperature and displacement fields thus allows incremental finite elements solution to the coupled problem. The incremental stress $d\boldsymbol{\sigma}$ and incremental heat dQ can be written in terms of Jacobian:

$$d\boldsymbol{\sigma} = J_{\boldsymbol{\sigma\epsilon}} : d\boldsymbol{\epsilon} + J_{\boldsymbol{\sigma}T} dT \tag{B.1}$$

$$dQ = J_{T\boldsymbol{\epsilon}} : d\boldsymbol{\epsilon} + J_{QT} dT \tag{B.2}$$

where $J_{\boldsymbol{\sigma}T}$ and J_{QT} are the tangent thermal modulus tensors with respect to the increments of stress and heat generation and $J_{\boldsymbol{\sigma\epsilon}}$ and $J_{Q\boldsymbol{\epsilon}}$ are the tangent stiffness tensors with respect to the increments of stress and heat generation. Constitutive stress-strain relation Eq. 2.127, in differential form:

$$d\boldsymbol{\sigma} = \boldsymbol{K} : [d\boldsymbol{\epsilon} - (\boldsymbol{R}dz + z\boldsymbol{N}d\eta + \boldsymbol{\alpha}_{eq}dT] \tag{B.3}$$

where R tensor order of two equals to:

$$\boldsymbol{R} = (\boldsymbol{K}_M^{-1} - \boldsymbol{K}_A^{-1}) : \boldsymbol{\sigma} + \boldsymbol{\epsilon}_{ori} + (\boldsymbol{\alpha}_M \boldsymbol{\alpha}_A)(T - T_0). \tag{B.4}$$

$\dot{Q}$, the volumetric heat generation per unit time in differential form is given by:

$$dQ = [\zeta - \boldsymbol{\sigma} : (\boldsymbol{\alpha}_M - \boldsymbol{\alpha}_A)]T\frac{dz}{dt} + Yz^2\frac{d\eta}{dt} + [a(1-z) + bz]\frac{dz}{dt} \tag{B.5}$$

Consistency with the transformation functions 2.129-2.131:

$$\partial_{\boldsymbol{\sigma}} F_z : d\boldsymbol{\sigma} + \partial_z F_z dz + \partial_{\boldsymbol{\epsilon}_{ori}} F_z : \boldsymbol{N} d\eta + \partial_T F_z dT = 0 \tag{B.6}$$

$$\partial_{\boldsymbol{\sigma}} F_{ori} : d\boldsymbol{\sigma} + \partial_z F_{ori} dz + \partial_{\boldsymbol{\epsilon}_{ori}} F_{ori} : \boldsymbol{N} d\eta + \partial_T F_{ori} dT = 0 \tag{B.7}$$

Using Eqs. B.3, B.6 and B.7 one gets the following:

$$A_{\boldsymbol{\epsilon}} : d\boldsymbol{\epsilon} + A_z dz + A_{ori} d\eta + A_T dT = 0 \tag{B.8}$$

$$B_{\boldsymbol{\epsilon}} : d\boldsymbol{\epsilon} + B_z dz + B_{ori} d\eta + B_T dT = 0 \tag{B.9}$$

where,

$$\begin{aligned}
A_{\boldsymbol{\epsilon}} &= \boldsymbol{K} : \partial_{\boldsymbol{\sigma}} F_z, \\
A_z &= \partial_z F_z - \partial_{\boldsymbol{\sigma}} F_z : \boldsymbol{K} : \boldsymbol{R}, \\
A_{ori} &= \partial_{\boldsymbol{\epsilon}_{ori}} F_z : \boldsymbol{N} - z\partial_{\boldsymbol{\sigma}} F_z : \boldsymbol{K} : \boldsymbol{N}, \\
A_T &= \partial_T F_z - \partial_{\boldsymbol{\sigma}} F_z : \boldsymbol{\alpha}, \\
B_{\boldsymbol{\epsilon}} &= \boldsymbol{K} : \partial_{\boldsymbol{\sigma}} F_{ori}, \\
B_z &= \partial_z F_{ori} - \partial_{\boldsymbol{\sigma}} F_{ori} : \boldsymbol{K} : \boldsymbol{R}, \\
B_{ori} &= \partial_{\boldsymbol{\epsilon}_{ori}} F_{ori} : \boldsymbol{N} - z\partial_{\boldsymbol{\sigma}} F_{ori} : \boldsymbol{K} : \boldsymbol{N}, \\
B_T &= -\partial_{\boldsymbol{\sigma}} F_{ori} : \boldsymbol{\alpha}
\end{aligned} \tag{B.10}$$

Solution for increments of martensite volume fraction and inelastic multiplier obtained using Eqs. B.8 and B.9 and given as:

$$dz = \boldsymbol{C}_{\boldsymbol{\epsilon}} : d\boldsymbol{\epsilon} + C_T dT, \tag{B.11}$$

$$d\eta = \boldsymbol{D}_{\boldsymbol{\epsilon}} : d\boldsymbol{\epsilon} + D_T dT. \tag{B.12}$$

where,

$$\boldsymbol{C_\epsilon} = \frac{A_{ori}\boldsymbol{B_\epsilon} - B_{ori}\boldsymbol{A_\epsilon}}{A_z B_{ori} - B_z A_{ori}},$$
$$C_T = \frac{A_{ori}B_T - B_{ori}A_T}{A_z B_{ori} - B_z A_{ori}},$$
$$\boldsymbol{D_\epsilon} = \frac{B_z\boldsymbol{A_\epsilon} - A_z\boldsymbol{B_\epsilon}}{A_z B_{ori} - B_z A_{ori}},$$
$$D_T = \frac{B_z A_T - A_z B_T}{A_z B_{ori} - B_z A_{ori}}. \tag{B.13}$$

Using values of dz and $d\eta$ in Eqs. B.11 and B.12 in B.3 and B.5 gives following incremental stress and heat generations:

$$d\boldsymbol{\sigma} = (\boldsymbol{K} - \boldsymbol{K} : \boldsymbol{R} \otimes \boldsymbol{C_\epsilon} - z\boldsymbol{K} : \boldsymbol{N} \otimes \boldsymbol{D_\epsilon}) : d\boldsymbol{\epsilon} + (-\boldsymbol{K} : \boldsymbol{R}C_T - z\boldsymbol{K} : \boldsymbol{N}D_T)dT, \tag{B.14}$$

$$dQ = \frac{G_z\boldsymbol{C_\epsilon} + H_{ori}\boldsymbol{D_\epsilon}}{dt} : d\boldsymbol{\epsilon} + \frac{G_z C_T + H_{ori}D_T}{dt} : dT, \tag{B.15}$$

where,

$$G_z = [\zeta - \boldsymbol{\sigma} : (\boldsymbol{\alpha}_M - \boldsymbol{\alpha}_A)]T + [a(1-z) + bz]sgn(\dot{z}), \tag{B.16}$$
$$H_{ori} = Yz^2. \tag{B.17}$$

Following the procedures indicated above the tangent stiffness and thermal moduli tensors are found to be:

$$\boldsymbol{J_{\sigma\epsilon}} = \boldsymbol{K} - \boldsymbol{K} : \boldsymbol{R} \otimes \boldsymbol{C_\epsilon} - z\boldsymbol{K} : \boldsymbol{N} \otimes \boldsymbol{D_\epsilon}, \tag{B.18}$$
$$\boldsymbol{J}_{\sigma T} = -\boldsymbol{K} : \boldsymbol{R}C_T - z\boldsymbol{K} : \boldsymbol{N}D_T, \tag{B.19}$$
$$\boldsymbol{J_{Q\epsilon}} = \frac{G_z\boldsymbol{C_\epsilon} + H_{ori}\boldsymbol{D}_\epsilon}{dt}, \tag{B.20}$$
$$J_{QT} = \frac{G_z C_T + H_{ori}D_T}{dt}. \tag{B.21}$$